Magnet System Design for the Helium Light Ion Compact Synchrotron

Thesis MSc Mechanical Engineering
Dept. Thermal & Fluid Engineering
University of Twente

Accelerator & Technology Sector
Directorate Office
CERN

G.W.D. Flier (s2015684)

University of Twente supervisor:	Prof. Dr. A.R. Thornton
University of Twente supervisor:	Dr. Ir. W.K. den Otter
CERN supervisor:	Dr. L. Bottura

September 10, 2024

UNIVERSITY OF TWENTE.

Abstract

This thesis presents the development and optimization of the magnet system for the Helium Light Ion Compact Synchrotron (HeLICS), which aims to advance helium ion therapy for cancer treatment.

The design incorporates six dipoles, fifteen quadrupoles, and three sextupoles. The dipoles, functioning as combined magnets, employ a specialized shimming scheme to ensure the required field quality. The quadrupoles are distinguished by two mechanical and three magnetic designs. The sextupoles have been optimized to produce an additional horizontal and vertical dipole field, removing the need for corrector magnets.

Utilizing ANSYS Maxwell for simulations, the magnet system's configurations were meticulously adjusted to optimize field quality and minimize optical aberrations. The design efforts focused on achieving a balance between system compactness, power efficiency, and field quality.

Results indicate that the developed magnet system could successfully control the beam trajectory based on the various magnets' integrated field strengths. With the initial design phase complete—encompassing lattice configuration, magnet design, and component integration—the next phase will focus on constructing a prototype of the critical dipole magnet. Further, the feasibility of incorporating a superferric dipole to potentially accommodate carbon ion acceleration in HeLICS is also being evaluated.

Acknowledgements

Contents

1 Introduction

Cancer is becoming an increasingly significant global health challenge, with rising incidence rates and substantial mortality worldwide. According to the World Health Organization, cancer is one of the leading causes of death globally, with approximately 10 million deaths in 2020 [1]. While there is reason for cautious optimism, with advancements in cancer treatments leading to a decline in mortality rates [2], there is no room for complacency. The burden of cancer is expected to increase in the coming decades, driven by factors such as ageing populations, lifestyle changes, and environmental influences. Projections indicate that the number of new cancer cases will increase from 19.3 million in 2020 to 28.4 million in 2040 [1]. The complexity and heterogeneity of cancer, characterized by its ability to adapt and resist treatments, have made it one of the most formidable diseases to manage effectively. Traditional cancer treatments, such as surgery, chemotherapy and radiation therapy, have been the mainstay of cancer management for decades. However, these approaches often come with severe side effects and varying degrees of effectiveness, necessitating the exploration of more advanced and precise treatment modalities.

1.1 Particle Therapy

Conventional external beam radiotherapy employs electromagnetic radiation in the form of X-rays to target and destroy cancerous cells. X-rays interact with tissues in a manner that is not highly selective. Figure 1, shows that X-rays deposit the peak relative dose shortly after entering the body, after which the relative dose steadily decreases. As a result, X-rays deposit most of their dose outside a tumour, leading to significant collateral damage to surrounding healthy tissues. Several strategies are employed to mitigate these adverse effects, such as rotating the beam around multiple axes to disperse the radiation over a broader volume of healthy cells while maintaining a concentrated dose within the tumour. Despite this, the treatment sessions are typically short and distributed over several days or weeks to allow the healthy cells time to recover and reduce potential side effects, ranging from acute skin reactions and fatigue to long-term complications such as memory or concentration problems and fibrosis [3, 4]. The limitations of X-ray therapy have spurred the development of particle therapy, also called ion therapy. This offers a more refined approach to cancer treatment by leveraging the unique physical and biological properties of charged particles. As ions move through matter, they lose energy and deposit a dose along their path, similar to X-rays. However, the energy lost (dose) is inversely proportional to the square of the ion's velocity, resulting in a peak in dose delivered just before the ion has zero velocity. This phenomenon is called the Bragg peak and can be seen in Figure 1. Increasing the kinetic energy increases the deposition depth and can be aligned to match the tumour site, thereby minimising damage to surrounding healthy tissues. This property makes ion therapy particularly advantageous for treating tumours near critical structures or in paediatric patients, where minimising radiation exposure to healthy developing tissues is paramount.

The most common type of particle therapy is proton therapy, with over 100 treatment facilities worldwide [6]. Carbon ion therapy is the other type of particle therapy with approximately 14 facilities globally [6]. Notable European centres for carbon ion therapy include the National Center for Oncological Hadrontherapy (CNAO) in Italy, MedAustron in Austria, and the Heidelberg Ion-Beam Therapy Center (HIT) in Germany. While carbon therapy is similar in its delivery method to proton therapy, it has a higher Relative Biological Effectiveness (RBE) due to the heavier ions. This increase in RBE leads to more significant biological damage to cancer cells, making carbon ions useful for treating various types of cancers that are difficult to treat with traditional methods. These include skull base tumours, sarcomas, recurrent cancers and radio-resistant tumours. However, the increased RBE also poses a greater risk to surrounding healthy tissues, necessitating precise treatment planning and delivery. This reduces patient throughput rates and increases treatment costs. Moreover, as carbon ions are twelve times
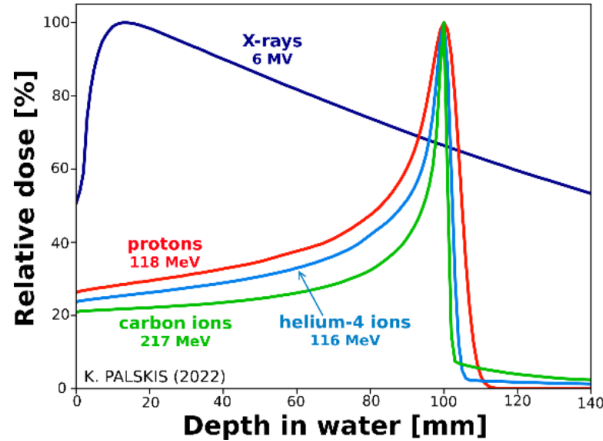
1

Figure 1: The Bragg peak of protons, helium and carbon ions compared to X-rays at specific energies [5].

heavier than protons, accelerating them to high enough kinetic energy levels poses significant technical challenges and costs; for example, the carbon ion gantry used in HIT weighs over 600 tons. There is growing interest in exploring other particles, such as oxygen or neon. Among the potential particles, helium ions show significant potential. The concept of using helium ions for radiotherapy dates back to the 1950s, with clinical trials beginning in 1975 at the Lawrence Berkeley National Laboratory (LBL). These trials, which extended until 1992, demonstrated the effectiveness of helium ions in treating various cancers, particularly those located near critical structures such as uveal melanomas and certain central nervous system tumours [7]. More research and clinical applications have been conducted in recent years, especially at CNAO and HIT [8–10]. These indicated that helium ions possess several advantages over protons for radiotherapy. Helium ions exhibit reduced lateral scattering and range straggling [11], resulting in a sharper Bragg peak and more precise energy deposition. Additionally, helium ions have a higher RBE than protons, enhancing cancer cell damage without increasing harm to normal tissues. A planning study focusing on paediatric patients indicated that helium ions could reduce the volume of irradiated normal tissue compared to proton therapy. This is crucial for minimising long-term side effects and the risk of secondary cancers in children, making helium ion therapy a promising alternative for treating paediatric cancers [8]. Compared to carbon ions, helium ions exhibit similar physical attributes, such as a sharp Bragg peak. With the advantage of having reduced radiobiological uncertainties and without potentially spoiling dose distributions due to excess fragmentation of heavier ion beams, particularly for higher penetration depths [8]. Additionally, helium ion therapy facilities can be much more compact and cost-effective, potentially allowing for broader adoption.

In summary, helium ion therapy offers a balance between proton and carbon ion therapies. It would be significantly smaller and more cost-effective than a carbon ion therapy facility. Moreover, it would provide superior treatment options for certain cancers compared to proton and carbon ion therapy.

1.2 Helium Ion Therapy Facility

Acknowledging the benefits of helium ion therapy, the Next Ion Medical Machine Study (NIMMS) at CERN is designing a dedicated facility for this advanced treatment. Figure 2 illustrates the proposed facility design, composed of three primary sections: the injection and initial acceleration area, the particle accelerator, and the transfer and treatment rooms.
In the first section, two independent ion sources can deliver beams of either protons or fully stripped helium ions. Additionally, there are plans to include a third ion source for fully
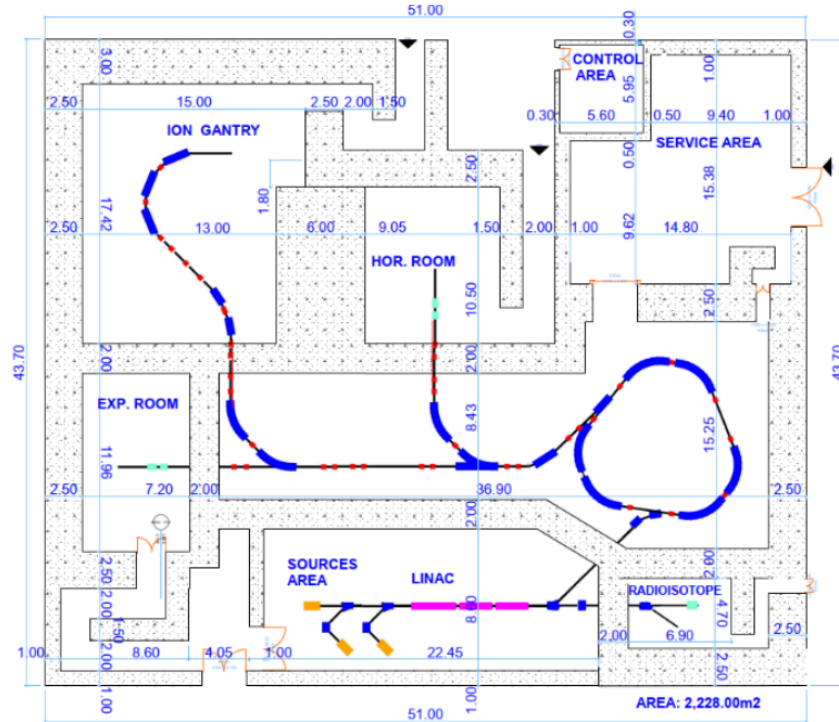
Figure 2: Layout of the proposed helium ion therapy facility. HeLICS, depicted as a rounded triangle on the right, serves as the central component. Ion sources are represented in yellow, linacs in pink, bending magnets in blue, and focusing magnets in red [5].

stripped carbon ions in a future upgrade. After the source, the particles enter the Radio Frequency Quadrupole (RFQ), accelerating them to 2 MeV/u and creating bunches (groups of particles) necessary for multi-turn injection into the particle accelerator. The helium and carbon beams can then be further accelerated in three consecutive linear particle accelerators (linacs) up to 5 MeV/u. The protons are accelerated in the same linacs up to 10 MeV to allow for the production of radioisotopes for therapy and imaging and the combination of both, theragnostic. Once the particles reach their required energy levels, they are injected into a circular particle accelerator: the Helium Light Ion Compact Synchrotron (HeLICS): the Helium Light Ion Compact Synchrotron (HeLICS). In HeLICS, helium ions are accelerated to a maximum energy of 220 MeV/u, enabling a penetration depth of 30 cm in water [5]. Conversely, protons can be accelerated to 700 MeV, facilitating proton radiography with low-intensity proton beams. Upon reaching the required energy levels, the beams are sent to an experiment room or two treatment rooms, one equipped with a fixed beam line and the other with a superconducting gantry [12]. The total surface for the facility, including treatment rooms and shielding, is expected to be about 2200 m^2.

The space required for HeLICS is around 200 m^2. This is comparatively larger than a commercial proton therapy solution that utilizes a cyclotron instead of a synchrotron [13], e.g. the ProteusONE from IBA, see Figure 3. Cyclotrons accelerate charged particles outwards from the centre of a flat cylindrical vacuum chamber along a spiral path, as seen in Figure 4. The particles are held in a spiral trajectory by a static magnetic field and accelerated by a rapidly varying electric field before being ejected at the peak energy [14]. Then, the beam's kinetic energy is decreased in a degrader to the required energies for therapy. This allows for a compact design for the accelerator but also reduces efficiency.

Instead, HeLICS utilizes a synchrotron where the accelerating particle beam travels around a fixed closed-loop path. During the accelerating process, the magnetic field that bends the

Figure 3: The cyclotron accelerator used in the proton therapy
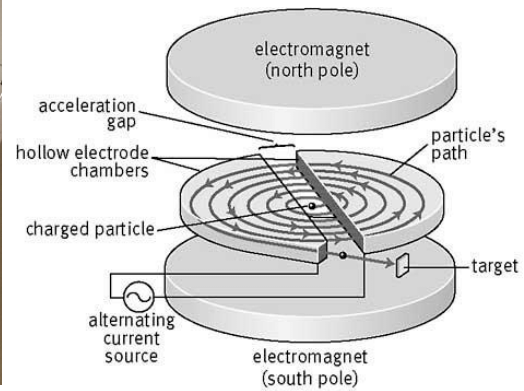solution, ProteusONE by IBA [15].

Figure 4: A schematic representation of a cyclotron [16].

particle beam into its closed path increases with time and is synchronized with the particles' increasing kinetic energy, hence the name: synchrotron. This closed path is enclosed within the beam pipe and maintained under vacuum conditions to prevent the beam from interacting with air particles. When the beam reaches its extraction energy, it can remain within the synchrotron until the patient is prepared for the dose. At that point, a kicker changes the beam's stable orbit, allowing it to be extracted through a septum magnet. A synchrotron requires more instrumentation and different magnets than a cyclotron to maintain a stable beam trajectory, resulting in a larger and more complex operation. Nevertheless, a synchrotron provides greater efficiency, higher extraction energies, and enhanced control over the beam [14]. Consequently, the decision was made to use a synchrotron, with the specific goal of keeping it compact to minimize investment costs and facilitate future commercialization. The initial design for HeLICS is depicted in Figure 5. Compared to the cyclotron in Figure 3, which only requires one large magnet with a constant field, HeLICS requires multiple types of magnets with varying magnetic fields. The design of these magnets will be the focus of this thesis.
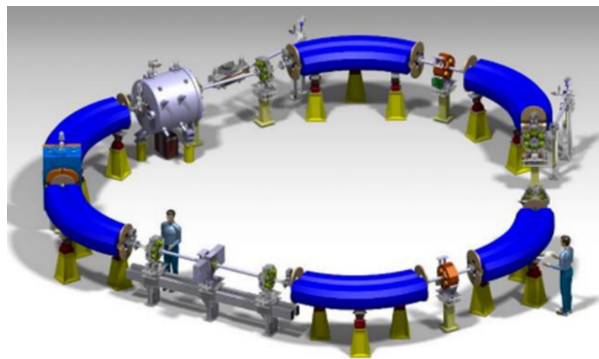

Figure 5: The initial design of HeLICS illustrating the arrangement of dipole magnets (blue) and quadrupoles (orange).

2   Synchrotron Magnet Theory

When a charged particle passes through an electromagnetic field, it experiences a force. This force, **F**, is called the Lorentz force and can be calculated by

$$\mathbf{F} = q(\mathbf{E} + \mathbf{v} \times \mathbf{B}), \tag{1}$$

where q is the charge of the particle, **E** the electric field (which is zero), **v** is the velocity, and **B** the magnetic flux density. The particles in HeLICS are accelerated by an electric field in the radiofrequency cavity. Meanwhile, the magnets only generate a magnetic field, which is used to bend and focus the beam. The main magnets in a synchrotron are the dipoles, quadrupoles and sextupoles, each with a different function.

A typical dipole generates a magnetic field with the field lines in the vertical direction. This is shown in Figure 6, B_x is zero, and B_y is positive. The strength of a dipole is called B_1 and is equal to $|B|$. Due to the cross-product, the particles will be bent horizontally, ensuring the particle beam precisely follows the trajectory inside the synchrotron.

Under ideal conditions, all particles within a beam would have identical energies and move in perfectly parallel trajectories. However, this is not realistic. When particles are injected into an accelerator, they inevitably have slight variations in their initial conditions, such as differences in energy or position. As a result, the size of the beam called the beam envelope, varies along the trajectory. Without additional steering, the beam envelope would increase until the beam is lost. The function of the quadrupoles is to focus the beam to ensure the beam envelope fits within the beam pipe. The magnetic field lines of a quadrupole can be seen in Figure 6. Along the positive y-axis, the magnetic field lines are horizontal and based on Equation 1, the force will be pointed downwards, while along the negative y-axis, the force will be pointed up. This reduces the beam size in the vertical plane, called focusing. Meanwhile, along the positive x-axis, the force will be pointed to the right and on the negative x-axis to the left, thus defocusing on the horizontal plane. The horizontal plane is used to denote the function of a quadrupole, making this a defocusing quadrupole. The magnetic field strength increases linearly with the distance from the centre, with $|B| = B_2 r$, where B_2 is the strength of the quadrupole.

Suppose two similar quadrupoles with opposite polarity are placed behind each other. In that case, the beam will, for example, diverge in the horizontal direction and converge in the vertical direction in the first quadrupole. In the second quadrupole, the opposite will occur, but as the beam is larger in the horizontal direction compared to before it entered the first quadrupole, it will converge more than it diverged. Moreover, since the beam is smaller in the vertical direction, it will not expand as much and still be smaller than before the beam entered
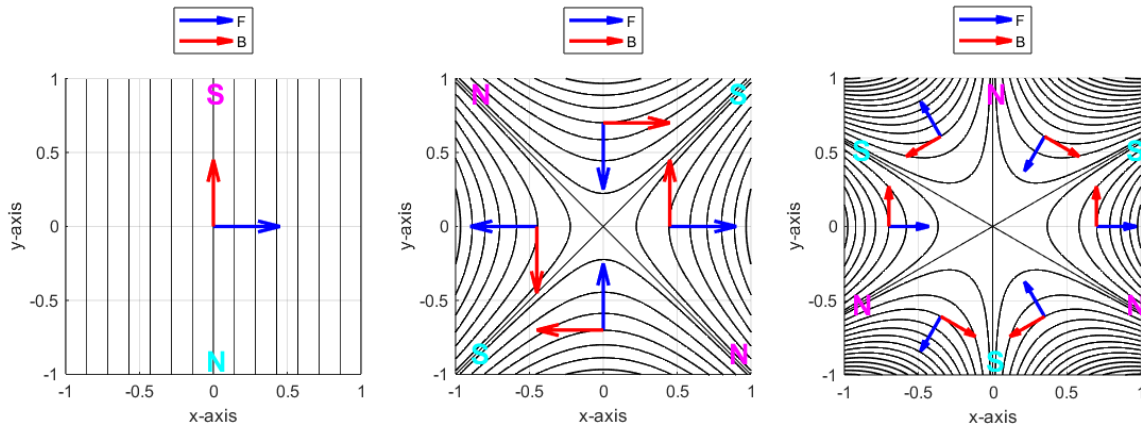

Figure 6: The magnetic field lines of a normal dipole (left), defocussing quadrupole (middle) and sextupole (right) and the corresponding force for a positively charged particle moving away from the reader.
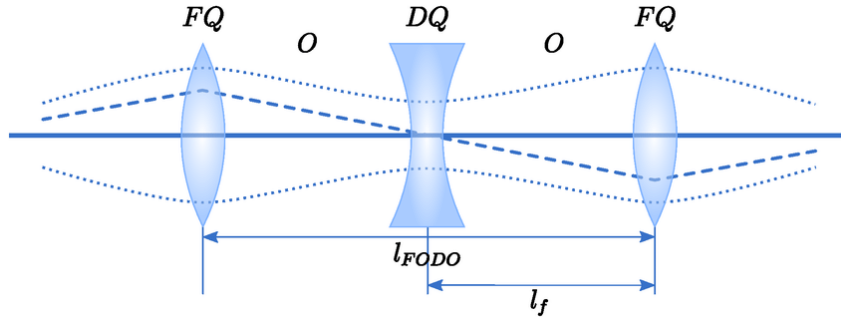
Figure 7: A FODO cell, the dotted line is the beam envelope along the trajectory and the dashed line is the trajectory of a particle [17].

the two dipoles. This arrangement is called a FODO cell; see Figure 7. Generally, a FODO cell consists of a focusing quadrupole (FQ), a drift space (O), a defocusing quadrupole (DQ) and a second drift space.

The initial energy of the particles injected into the accelerator varies slightly, following a specific energy distribution. These small differences at the start can lead to significant deviations in the particles' momentum and trajectory during acceleration. Additionally, factors like magnetic field imperfections, or quantum effects can further contribute to these variations. The particles with a higher momentum experience less focusing in a quadrupole compared to those with lower momentum. As a result, these particles will deviate more from the reference trajectory. A sextupole is used to correct these larger deviations caused by the energy distribution, the so-called chromaticity. The magnetic field strength of a sextupole magnet increases quadratically with distance from the centre, following the relation $|B| = B_3 r^2$. This means that a sextupole provides stronger focusing to particles that deviate further from the centre.

The magnetic fields of these magnets may have minor imperfections resulting from the fabrication process, or there may be alignment errors between different magnets. These minor errors can cause the beam to deviate from its intended path. Orbit corrector magnets play a vital role in addressing these deviations. These magnets have a weak dipole field, oriented either horizontally or vertically. They can rapidly adjust the strength of their magnetic field to steer the particle beam back onto its correct trajectory. This correction process is essential for maintaining the stability and precision of the beam.

In summary, dipole magnets bend the beam along its intended path, while quadrupole magnets focus the beam. Sextupole magnets correct the difference in trajectory due to the energy distribution among the particles. Finally, orbit corrector magnets fine-tune the beam's trajectory, ensuring it follows the correct path precisely.

2.1 Field Harmonics

The terms used to describe the strengths of the different magnet types B_1, B_2 and B_3 are called multipoles. Multipoles conveniently describe the harmonic content of a magnetic field. The magnetic field strength can be written as a function of these multipoles

$$|B| = B_n r^{n-1}. \tag{2}$$

Considering the 2D cross-section of an infinitely long magnet, the horizontal and vertical magnetic field components, B_x and B_y, within a circular region inside the aperture (up to the first field source) can be expressed as a complex power series expansion around a point. This expansion takes the form:

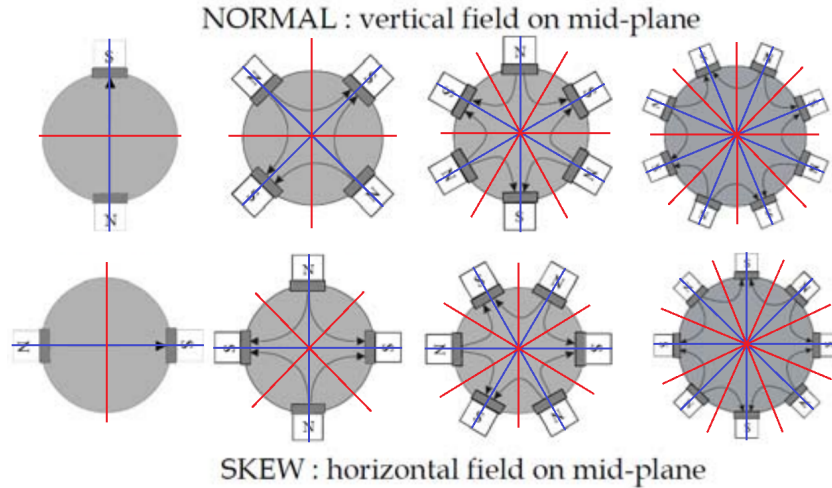$$B_y(x,y) + iB_x(x,y) = \sum_{n=1}^{\infty} (B_n + iA_n)(x + iy)^{n-1}, \tag{3}$$

Figure 8: Comparison of magnetic field lines for normal (top) and skew (bottom) configurations in dipole, quadrupole, sextupole, and octupole magnets [18]. The red lines indicate planes of even symmetry where the magnetic flux is normal to the boundary. In contrast, the blue lines indicate planes of odd symmetry where the magnetic flux is tangential to the boundary. The degree of symmetry is the sum of the even and odd symmetries.

where B_n and A_n are the normal and skew multipoles, respectively. The magnetic field of a skew magnet is rotated compared to a normal magnet; see Figure 8. The ideal magnetic field of a normal dipole (with poles oriented vertically) is uniform, with only B_1 as non-zero. The corresponding magnetic field components are $B_x = 0$ and $B_y = B_1$. Conversely, the ideal magnetic field of a skew dipole (with poles oriented horizontally) is described with only A_1 as non-zero. Resulting in the magnetic field components $B_x = A_1$ and $B_y = 0$. A normal quadrupole field has B_2 as the only non-zero term, leading to magnetic field components $B_x = B_2 y$ and $B_y = B_2 x$. Lastly, in a normal sextupole, only B_3 is non-zero, resulting in $B_x = 2B_3 xy$ and $B_y = B_3(x^2 - y^2)$.

Expressing the magnetic field using Equation 3 enables the description of the field with an infinite series of complex coefficients. However, this series converges quickly, so only the first 15 coefficients are typically considered, with higher-order terms being neglected. In the Large Hadron Collider at CERN, only the first 11 multipoles are considered [19]. This considerably reduces the information needed to describe a magnetic field. Furthermore, some coefficients are eliminated due to design symmetries. These are the not-allowed (or random) multipoles, which ideally should not appear in the magnet but may result from asymmetries introduced during the fabrication process. The allowed multipoles are those expected in the design; see Table 1. The magnetic design process involves optimizing the geometry to minimize unwanted harmonics.

Since the magnet is designed to generate a primary field component, it is customary to normalize the multipoles accordingly. For a normal dipole, Equation 3 is normalized with respect to its

Table 1: The allowed harmonics for different degrees of symmetry [20].

	Degree of symmetry	Allowed harmonics
No symmetry	0	B_n and A_n for $n \in 1, 2, 3, 4$, etc.
Half symmetric (C-shape) dipole	1	B_n for $n \in 1, 2, 3, 4$, etc.
Fully symmetric (H-shape) dipole	2	B_n for $n \in 1, 3, 5, 7$, etc.
Fully symmetric quadrupole	4	B_n for $n \in 2, 6, 10$, etc.
Fully symmetric sextupole	6	B_n for $n \in 3, 9, 15$, etc.

main component B_1 and a factor of 10^{-4}

$$B_y(x,y) + iB_x(x,y) = 10^{-4} B_1 \sum_{n=1}^{\infty} (b_n + ia_n) \left(\frac{x+iy}{R_{\text{ref}}} \right)^{n-1}, \tag{4}$$

where b_n and a_n are the normalized multipoles and R_{ref} is the reference radius. The reference radius is introduced to have non-dimensional multipoles. It has no physical meaning but is chosen to express the relative weight of the field harmonics. Typically, it is set at two-thirds of the sampling radius R_s. The sampling radius is the largest radius around the origin that encapsulates an area free of charge and magnetic material. Equation 4 is normalized to 10^{-4} since the expected deviations from the ideal field are expected to be around 0.01% [19]. As a result, the main term of a dipole b_1 equals 10^4.

A limitation of Equations 3 and 4 is that they are only valid within the domain $r \leq R_s$ and R_s. This poses a challenge if the aperture is significantly broader than it is tall, as in the case of a dipole. Nevertheless, if there is no charge or magnetic material (inside the aperture), the multipoles are a good approximation for the field outside the domain R_s.

Moreover, these equations hold only under the condition that $\frac{\partial \mathbf{B}}{\partial z} = 0$, which is valid for the 2D cross-section of an infinitely long magnet. However, the magnetic field along the body of a straight magnet is also constant; see Figure 9. The body of the magnet is defined as the region where the magnetic field does not vary along the trajectory s, while the ends are where the magnetic field begins to decrease. It is important to note that the length of the magnet's body does not correspond to the length of the yoke, as the magnetic field strength starts to decrease within the yoke itself.

At the ends of a magnet, different expansions, such as elliptical harmonics in toroidal coordinates, are required to describe the magnetic fields [21]. However, due to their complexity, these methods are not widely employed. Instead, a more practical approach integrates the magnetic field components over the trajectory

$$\int B_y(x,y)\,ds + i \int B_x(x,y)\,ds = \sum_{n=1}^{\infty} \left(\int B_n\,ds + i \int A_n\,ds \right) (x+iy)^{n-1}. \tag{5}$$

For the normalized multipoles, the integration becomes

$$\int B_y(x,y)\,ds + i \int B_x(x,y)\,ds = 10^{-4} \int B_1\,ds \sum_{n=1}^{\infty} \left(\int b_n + i \int a_n \right) \left(\frac{x+iy}{R_{\text{ref}}} \right)^{n-1}. \tag{6}$$

Notably, the normalized multipoles are not integrated over the trajectory to preserve their unitless nature. Thus, they are denoted as $\int b_n$ and $\int a_n$ to distinguish between the normalized multipoles calculated through Equations 4 and 6. These integrations are only valid over regions with limits where the magnetic field remains constant along s, thus from inside the body to far outside the magnet [19].
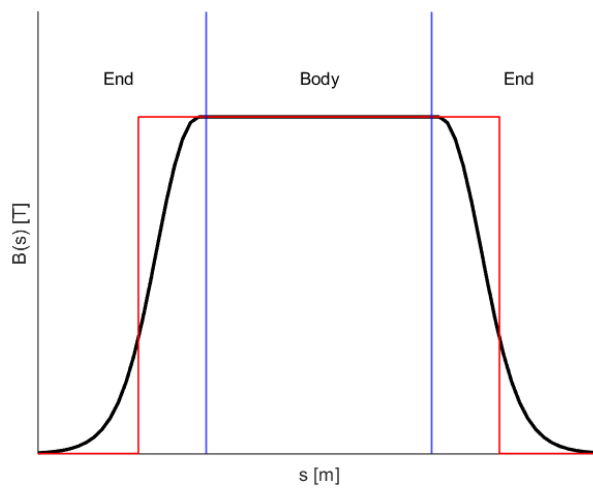
Figure 9: The magnetic field strength along a trajectory (s), shown in black. The body is the region where the magnitude of B remains constant, and the ends are the regions where B decreases to zero. The red lines denote the length of the yoke.

3   Requirements HeLICS

The magnetic beam rigidity $B\rho$ is the fundamental starting point for defining the requirements of a synchrotron and is based on the particles' energy and charge. For a fully stripped helium ion, this gives a momentum p of

$$p = \frac{\sqrt{(E_0 + E_k)^2 - E_0^2}}{c} = 9.03 \, \text{GeV/c}. \tag{7}$$

Here, c is the speed of light, the kinetic energy E_k is 0.88 GeV, and the helium ion's rest energy, E_0, is 3.73 GeV. This gives a normalized velocity

$$\beta = \frac{v}{c} = \frac{cp}{E_k + E_0} = 0.588, \tag{8}$$

and a Lorentz factor

$$\gamma = \frac{1}{\sqrt{1 - \beta^2}} = 1.24. \tag{9}$$

The centrifugal force acting on the particle is

$$F_c = \frac{\gamma m v^2}{\rho} = \frac{pv}{\rho}, \tag{10}$$

where m is the mass, v the velocity, and ρ the bending radius. The particle's velocity is perpendicular to the magnetic field, so Equation 1 can be written as $F_c = qvB$. This gives

$$qvB = \frac{pv}{\rho}, \tag{11}$$

which can be simplified to

$$B\rho = \frac{p}{q} = 4.52 \, \text{Tm}. \tag{12}$$

As stated before, the dipoles are responsible for bending the beam. The strength of the dipoles B_1 is set at 1.65 T, resulting in a bending radius ρ of 2.737 m. Increasing the peak field would decrease the size of the synchrotron but lead to more magnetic saturation. Magnetic saturation occurs when an increase in the applied magnetic field no longer significantly increases the magnetization of the material. Consequently, the generated magnetic field strength ceases to increase proportionally with the current. The ratio of the actual generated field strength to the theoretical magnetic field strength (assuming a linear relationship with current) is called the magnetic efficiency. Moreover, magnetic saturation increases the difference in field quality between injection and extraction, complicating the operation of the magnet.

The magnetic fields at injection and extraction for different beams are calculated using the bending radius of 2.737 m and are presented in Table 2. Note that the magnetic field at extraction for carbon ions would exceed 1.65 T. This higher field is a future consideration and can be achieved using the same iron yoke with superconducting coils, a so-called super ferric magnet.

To keep HeLICS compact, it will consist of a triangular layout with three straight sections measuring 4.4 meters, as shown in Figure 10. The space in these straights is reserved for a septa magnet for injection, a kicker magnet to destabilize the beam's orbit in preparation for extraction, a septa magnet for extraction, an RF cavity for acceleration, instrumentation to measure the beam's properties and vacuum pumps. The three bending sections consist of two 60-degree dipoles separated by a straight section of 1.6 meters. Combined with the length of the trajectory in the dipoles,

$$L_{mag} = \rho\theta = 2.866 \, \text{m}, \tag{13}$$

Table 2: Key properties of different particle beams used in HeLICS.

Particle type	p^+	$4He^{2+}$	$12C^{6+}$
Mass-to-charge ratio [u/e]	1	2	2
Injection energy [MeV/u]	10	5.0	5.0
Extraction energy [MeV/u]	700	220	430
Magnetic field at injection [T]	0.167	0.236	0.236
Magnetic field at extraction [T]	1.63	1.65	2.42

this gives a total length of 35.2 m for a single turnS. This single orbit rotation is split into three identical unit cells to simplify simulations. Each of these unit cells is made up of the same magnets for which the following nomenclature will be used to denote the five different magnet types: Magnet Bending (MB), Magnet Quadrupole Bend (MQB), Magnet Quadrupole Focusing (MQF), Magnet Quadrupole Defocusing (MQD), and Magnet Sextupole (MSX). The location of the different magnets can be seen in Figure 10.

The synchrotron's unit cells comprise the following magnets in sequence: MB, MQB, MSX, MB, MQF, MQD, MQD, and MQF. The MQFs and MQDs are situated in the long straight sections, while the MQBs are placed in the short straight sections between the MBs. This order does not match the trajectory the beam will experience just after it has been injected. This order is based on the simulations done by the beam optics team, and it has been repeated here for consistency.

Table 3 presents the required integrated field strengths to ensure the proper functioning of the lattice design illustrated in Figure 10. It can be seen that the MB will have a dipole and an additional quadrupole field. This is done to keep HeLICS compact. Since the quadrupole component is negative, the beam experiences alternating focusing and defocusing quadrupole components along the trajectory. As a result, the unit cell comprises three reversed FODO cells, see Figure 7: first defocusing from the MB and focusing from the MQB, then MB and the MQF, then a single defocusing quadrupole MQD, and finally the MQD and MQF.
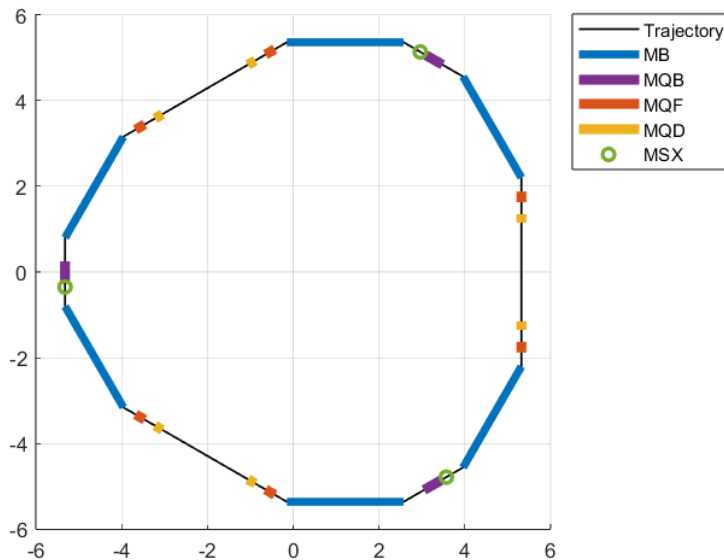

Figure 10: Schematic of the lattice design for HeLICS with a triangular layout. The trajectory of the beam inside the MBs is not shown.

Table 3: The required integrated dipole, quadrupole and sextupole field strength per magnet.

	MB	MQB	MQF	MQD	MSX
$\int B_1\, ds$ [Tm]	4.73	0	0	0	0
$\int B_2\, ds$ [T]	-2.25	4.90	4.64	-2.85	0
$\int B_3\, ds$ [T/m]	0	0	0	0	-6.75

3.1 Aperture

The beam envelope is the main driver of the size of the aperture. The beam envelope is denoted by $\sqrt{5}\sigma(s)$ in either x or y direction, where s is the distance along the particle trajectory. The maximum values of the beam envelope are determined over the magnets, extending 150 mm outwards for the MB and 50 mm for the other magnet types. This is done to leave space for the connection of two different beampipes. The dotted lines in Figure 11 display the resulting values and are listed in Table 4. Based on these, the decision was made to utilize a round beam pipe in all the magnets except the MB, which will have a rectangular beam pipe. This is done for manufacturing reasons and to keep the gap height to a minimum. Furthermore, to reduce the cost of manufacturing, the same laminations will be used for all the quadrupoles. Moreover, since the integrated quadrupole components for the MQB and MQF are relatively similar, see Table 3, the same magnet design will be used for both but operated at different currents. Finally, there is no space between the MQB and MSX to change the beam pipe; instead, the same beam pipe will be used.

Various tolerances and errors must be added to the beam envelope to prevent accidental beam loss. These tolerances include mechanical errors due to fabrication processes and positioning errors due to alignment inaccuracies. Using the ELENA accelerator as a reference [22], these tolerances can be estimated for the dipoles, quadrupoles, and sextupoles in the HeLICS system. Form errors arise from defects in the fabrication of the magnets and vacuum pipes. For the magnets, the form errors consist of two main components. The mechanical errors due to the machining and stacking of laminations are estimated at 0.05 m. The fiducialisation errors, representing measurement discrepancies between the physical opening of the magnet and the target, were also estimated at 0.05 mm. Thus, the total form error for magnet openings is 0.1 mm.
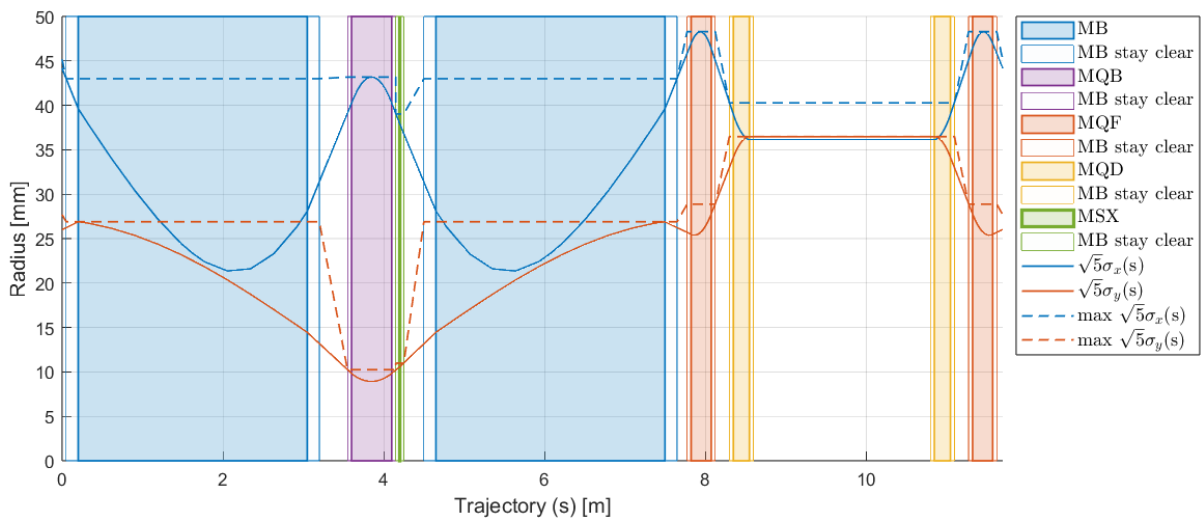

Figure 11: Beam envelope plotted over the trajectory of a unit cell. The dashed line depicts the maximum beam envelope per magnet.

For vacuum pipes, the errors are related to the inner and outer diameters, as these pipes are formed from a single metal sheet. The standard value for form errors, including straightness and circularity, is 0.3 mm. When considering dipole magnet chambers, a more pessimistic scenario accounts for machining and welding tolerances of 0.5 mm on both the outer and inner surfaces, plus a deflection due to vacuum pressure estimated at 0.4 mm. Therefore, the total form error for vacuum pipes is 0.9 mm.

Finally, the perpendicularity errors on the vacuum flanges. Bellows can compensate for these. If that is not the case, the perpendicularity error of flanges relative to the beam pipe must be multiplied by the length of the pipe to determine the total defect. A standard value of 0.2 mm and a length of 500 mm result in a maximum defect of 1 mm.

Positioning errors stem from inaccuracies in the alignment tooling and must be accounted for to maintain beam stability. For ELENA, the standard positioning error for magnets is 0.6 mm, with a 3σ certainty. Additionally, there is a potential mismatch between the mechanical and magnetic centres of the quadrupoles and sextupoles, estimated at 2 mm. The positioning errors of the vacuum chambers are 0.6 mm in the dipoles due to being equipped with targets, whereas in the other magnets, a more conventional accuracy of 1.0 mm is estimated.

Another way to keep the synchrotron compact is to have instrumentation inside the magnets' apertures. The Beam Position Monitors (BPMs) are suitable for this and a design similar to the one used in ELENA [23] will be used. These can measure the beam position in 2 planes and will placed in the MQBs and the MQDs, giving a total of 9 BPMs per plane. This will add 14.6 mm to the apertures of the selected quadrupoles. The form errors of the BPMs come from the tolerances in manufacturing, which are expected to be around 0.2 mm. For the positioning errors, this is expected to be 0.6 mm relative to the beam pipe.

The space for tolerances, instrumentation, beam pipe and beam envelopes is summarized in Table 12 and visualised in Figure 12. The quadrupoles and sextupoles will have the same size round beam pipe and thus the same aperture radius of 65.4 mm. The MB will have a total aperture height and width of 70 by 200 mm. This was decided before HeLICS's lattice design and, by extension, beam envelope were known.
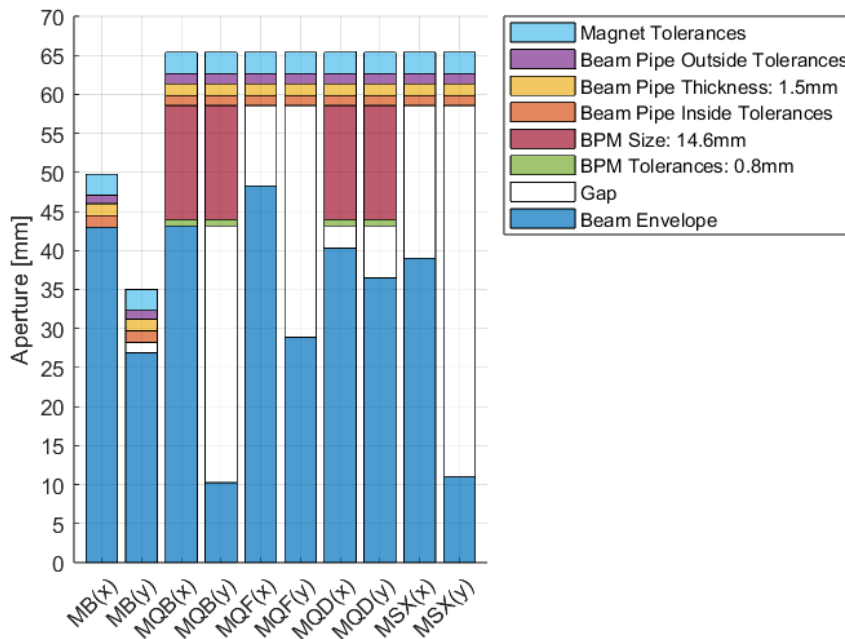

Figure 12: The minimal aperture per magnet per plane, based on the space required for the beam envelope, instrumentation, beam pipe, errors and tolerances, in mm.

Table 4: The space required for the apertures per magnet, based on the beam envelope, instrumentation, beam pipe, errors and tolerances, in mm.

Tolerance Type	MB	MQB	MQF	MQD	MSX
Aperture size (x-plane, y-plane) or radius R	100, 35.0	R65.4	R65.4	R65.4	R65.4
Total (x-plane, y-plane)	49.8, 33.7	65.4,32.5	55.1,35.7	62.5,58.7	45.8,17.8
Sum tolerances magnet	2.7	2.7	2.7	2.7	2.7
Mechanical errors	0.05	0.05	0.05	0.05	0.05
Magnet fiducialisation	0.05	0.05	0.05	0.05	0.05
Magnet position errors	0.6	0.6	0.6	0.6	0.6
Magnetic offset center	2.0	2.0	2.0	2.0	2.0
Sum tolerances outside beam pipe	1.1	1.3	1.3	1.3	1.3
Perpendicularity errors outside beam pipe	0	0	0	0	0
Form errors outside beam pipe	0.5	0.3	0.3	0.3	0.3
Position error outside beam pipe	0.6	1.0	1.0	1.0	1.0
Thickness beam pipe	1.5	1.5	1.5	1.5	1.5
Sum tolerances inside beam pipe	1.5	1.3	1.3	1.3	1.3
Perpendicularity errors inside beam pipe	0	0	0	0	0
Form errors inside beam pipe	0.5	0.3	0.3	0.3	0.3
Position error inside beam pipe	0.6	1.0	1.0	1.0	1.0
Deflection due to vacuum	0.4	0	0	0	0
Sum tolerances BPM	0	15.4	0	15.4	0
Size BPM	0	14.6	0	14.6	0
Form errors BPM	0	0.2	0	0.2	0
Position errors BPM	0	0.6	0	0.6	0
Max beam envelope (x-plane, y-plane)	43.0, 26.9	43.2,10.3	48.3,28.9	40.3,36.5	39.0,11.0

3.2 Field Quality

The beam envelope is the benchmark for defining the Good Field Region (GFR) within a magnet aperture. The GFR of the quadrupoles will be circular with a radius of 48.3 mm, the maximum beam envelope of the three quadrupoles. For the MSX, the GFR will have a radius of 39.0 mm. The GFR of the MB was conservatively estimated as an ellipse, measuring 120 mm in width and 60 mm in height. This was based on an initial estimate during the lattice design phase, as the design for the MB and the lattice were done in parallel.

Two parameters are used to evaluate the field quality in the GFR. The first one is the Relative Field Deviation (RFD). It is defined as the generated field minus the ideal field divided over the ideal field. In two dimensions, this is

$$\frac{|\Delta B|}{|B|} = \frac{\left| \begin{bmatrix} B_x(x,y) \\ B_y(x,y) \end{bmatrix} - \begin{bmatrix} B_{x\,ideal}(x,y) \\ B_{y\,ideal}(x,y) \end{bmatrix} \right|}{\left| \begin{bmatrix} B_{x\,ideal}(x,y) \\ B_{y\,ideal}(x,y) \end{bmatrix} \right|}. \tag{14}$$

The ideal field components are determined through Equation 3, with only the main component as non-zero, e.g. B_1 for a normal dipole. In three dimensions, the integrated RFD is defined as

$$\frac{|\Delta B|}{|B|} = \frac{\left| \begin{bmatrix} \int B_x(x,y)\,ds \\ \int B_y(x,y)\,ds \end{bmatrix} - \begin{bmatrix} \int B_{x\,ideal}(x,y)\,ds \\ \int B_{y\,ideal}(x,y)\,ds \end{bmatrix} \right|}{\left| \begin{bmatrix} \int B_{x\,ideal}(x,y)\,ds \\ \int B_{y\,ideal}(x,y)\,ds \end{bmatrix} \right|}. \tag{15}$$

The z-components of the magnetic field do not affect the particles and can thus be ignored. The integrated ideal field components are determined through Equation 5, with only the integrated

main component as non-zero. The RFD should be below 0.01% [24] for a dipole. However, as the MB is a combined function dipole, this requirement is relaxed to 0.05%. The allowed RFD for the quadrupoles and sextupole is also set at 0.05%.

The other parameter against which the field quality will be evaluated is the Sum of the Normalized Multipoles (SNM):

$$\sum_{n}^{\infty} |b_n| \leq 5. \tag{16}$$

This is done without the main component of the magnet as this is, by definition, 10^4, see Equation 4. To evaluate the magnetic field over the whole magnet, the integrated SNM is

$$\sum_{n}^{\infty} \left| \int b_n \right| \leq 5. \tag{17}$$

The limit for the sum of the normalized multipoles is set at 5 for the dipoles, quadrupoles and sextupoles.

4   Ansys Maxwell Solver

Most of the magnetostatic simulations are performed with the ANSYS Maxwell software. Only the iterative 2D designs for the quadrupoles and sextupoles are done in FEMM 4.2. ANSYS Maxwell is a comprehensive tool for simulating electromagnetic fields through the Finite Element Method (FEM). The core of the simulation relies on solving Maxwell's equations in differential form under steady-state conditions. The primary equations governing magnetostatic simulations are Ampère's law with no time variation

$$\nabla \times \mathbf{H} = \mathbf{J}, \tag{18}$$

and Gauss's law for magnetism

$$\nabla \cdot \mathbf{B} = 0. \tag{19}$$

Here, $\mathbf{H}$ is the magnetic field intensity, $\mathbf{J}$ is the current density, and $\mathbf{B}$ is the magnetic flux density related to $\mathbf{H}$ by $\mathbf{B} = \mu \mathbf{H}$. The permeability of the material μ is equal to the vacuum magnetic permeability μ_0 times the relative magnetic permeability μ_r. Substituting

$$\mathbf{H} = \frac{\mathbf{B}}{\mu_r \mu_0} \tag{20}$$

into Ampère's Law gives

$$\nabla \times \left(\frac{\mathbf{B}}{\mu_r \mu_0} \right) = \mathbf{J}. \tag{21}$$

To satisfy Equation 19, $\mathbf{B}$ is expressed as function of $\mathbf{A}$:

$$\mathbf{B} = \nabla \times \mathbf{A}. \tag{22}$$

Substituting this equation into Equation 21 gives the equation that is solved in Ansys Maxwell

$$\mathbf{J} = \nabla \times \left(\frac{\nabla \times \mathbf{A}}{\mu_r \mu_0} \right). \tag{23}$$

It is important to note that $\mathbf{A}$ is not unique; different vector potentials can lead to the same magnetic field $\mathbf{B}$. This is because $\mathbf{B}$ does not change when a gradient of any scalar field ϕ is added to $\mathbf{A}$ (i.e., $\mathbf{A}' = \mathbf{A} + \nabla \phi$) since the curl of a gradient is always zero: $\nabla \times (\nabla \phi) = \mathbf{0}$. Ansys Maxwell solves electromagnetic field problems by solving Maxwell's equations in a finite region of space with appropriate boundary conditions and initial conditions to obtain a solution with guaranteed uniqueness. The simulation time can be considerably reduced by utilising symmetric boundary conditions. Odd symmetry means that the current on one side of the plane flows in the opposite direction to the current on the other side of the plane. The magnetic flux is tangential to this boundary. Even symmetry means the direction of current flow is the same on both sides of the plane. Thus, the magnetic flux is normal to this type of boundary. The number of degrees of symmetry in two-dimensional space for various magnets are illustrated in Figure 8 and Table 1. The portion of the model that needs to be solved in 2D can be expressed as follows:

$$\text{Model portion in 2D} = \frac{1}{2 \times (\text{degrees of symmetry})}. \tag{24}$$

These degrees of symmetry also apply in three-dimensional (3D) space. However, 3D modelling introduces an additional symmetry on the vertical plane in the middle of the magnet, allowing only half of the model to be simulated. Since the current flows through this plane, a distinct boundary condition is applied, specifically the Neumann boundary condition. Here, the magnetic field ($\mathbf{H}$) remains tangential to the boundary, ensuring that magnetic flux does not cross
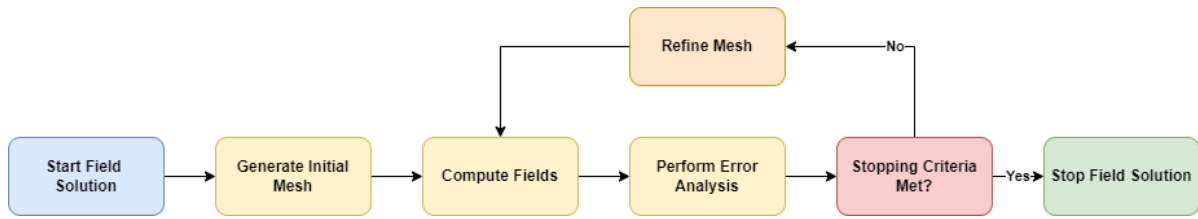
Figure 13: Ansys Maxwell workflow diagram for FEM with adaptive meshing.

it. To obtain the set of algebraic equations to be solved, the problem's geometry is discretized into small elements, typically triangles in 2D and tetrahedrons in 3D. All the model solids are meshed automatically by the mesher. The general process for solving a field can be seen in Figure 13.

There are two stopping criteria: the Energy Error % and the Delta Energy %. Ansys Maxwell uses the Curl of H to find the current density and subtracts all input currents and other sources. For a perfect solution the result would be zero, for a real, finite mesh the result is some amount of residual current density. The energy value calculated from this residual current density as a percentage of the total energy is called the Energy Error %. If more than one pass has been completed, the software also calculates the change in total energy from the previous pass. The percentage difference is the Delta Energy %. Mesh refinement continues until both the Energy Error % and the Delta Energy % are below the target Percent Error specified by the user (or until it reaches the Maximum Number of Passes requested). When the error targets are not satisfied, the mesh is refined.

5   Design of the Dipole

This section proposes a design for the MB, illustrated in Figures 14 and 15. The design ensures continuous operation at peak energy without the risk of overheating. Additionally, within the GFR, the field quality at both injection and extraction of protons and helium ions is optimized to meet the required RFD and SNM tolerances. To improve performance, the end plates are designed with optimized chamfers to reduce the risk of pole saturation, which can otherwise introduce unwanted multipoles.
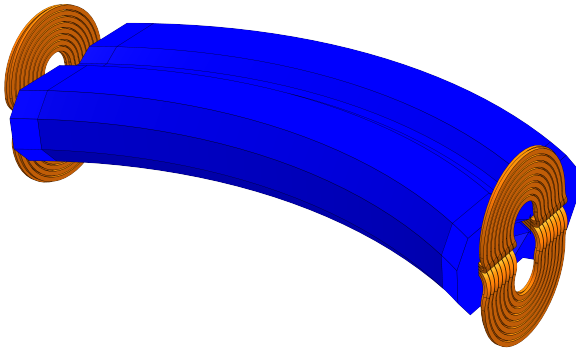
Figure 14: Design of the MB, with the coil in orange and the yoke and end plates in blue.
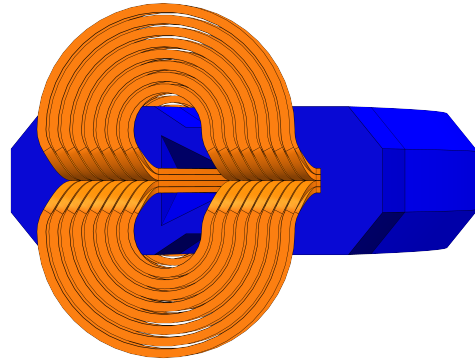
Figure 15: Front view of the MB, the shim cut-out in the end plate can be seen.

As previously discussed, the function of the MB in HeLICS is to bend the beam along a circular trajectory with a radius of 2.737 m. This is achieved thanks to an integrated dipole field strength of 4.73 Tm, bending the beam by 60°. Consequently, the magnetic length, computed in Equation 13, is 2.866 m, resulting in a B_1 component of 1.65 T.

5.1   Yoke Design

To conserve lattice space in the accelerator, the MB will be a combined-function magnet that simultaneously bends and defocuses the beam. The integrated quadrupole field strength is -2.51 T. There are two complementary approaches to generating the integrated B_2 component. Firstly, adding a 30° pole face rotation, as depicted in Figure 16, produces a defocusing field at the MB's fringe field. This modification transitions the MB from a sector dipole to a rectangular dipole configuration. Rectangular dipoles are commonly used to conserve lattice space by providing additional defocussing [25, 26]. This modification is expected to achieve an integrated B_2 field of -1.09 T.
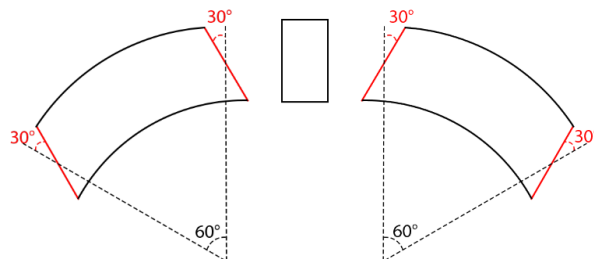
Figure 16: Top view of two dipoles with a quadrupole in between. The dipoles have a 30° pole face rotation to provide additional defocussing [27].

Secondly, the pole shape of the MB is optimized to produce both quadrupole and dipole fields. This shape can be modelled as the edge of a large quadrupole, mathematically represented by:

$$y_{\text{pole}} = \frac{B_1 h}{B_1 + B_2 x}, \tag{25}$$

where y_{pole} is the vertical position of the pole surface, h is the aperture height of 35 mm, and x is the horizontal position along the pole face. This function describes a translated hyperbola, as illustrated in Figure 17. To achieve the required integrated quadrupole field strength of -1.42 T, the corresponding quadrupole field strength along the magnet should be

$$B_2 = \frac{-1.42}{L_{\text{mag}}} = -0.50 \text{ T/m.} \tag{26}$$

A first-order approximation of the pole shape can be expressed as a straight line passing through $x = 0$ and $y = h$, with a slope of

$$\frac{dy}{dx} = -\frac{B_2 h}{B_1} = 0.61°. \tag{27}$$

However, this approximation is not applied in the current design. Initially, the MB was designed with a quadrupole field strength of -1.1 T/m, corresponding to a slope of 1.3°. To simplify achieving the requirements for the field quality, it was decided not to use this approximation. Instead, the translated hyperbola was adopted as the final pole shape. Nevertheless, with the lower quadrupole field strength, further investigation is required to determine if the field quality is maintained while approximating the pole shape with a straight slope of 0.61°, as this would simplify the manufacturing process.

Combining the pole face rotation and the hyperbolic pole shape, the integrated B_2 component of -2.51 T is achieved, with -1.09 T from the pole face rotation and -1.42 T through the pole profile. This should enable the MB to efficiently fulfil both bending and defocusing roles while optimising the accelerator's lattice space.
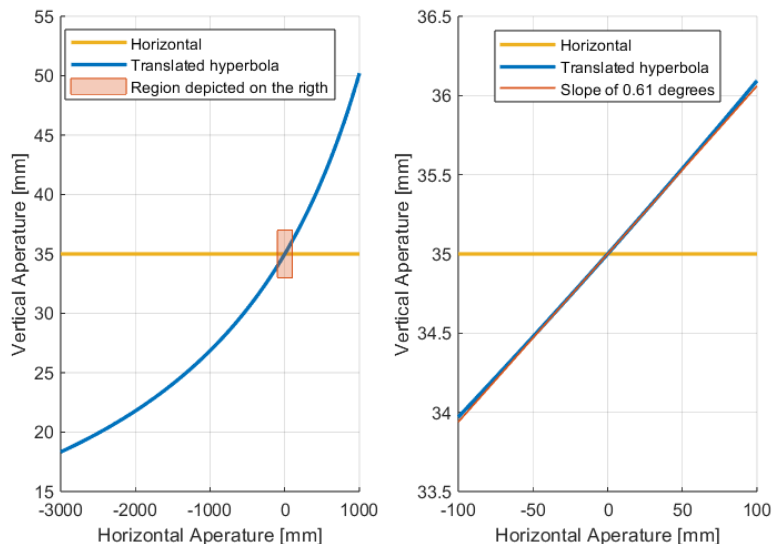
Figure 17: Translated hyperbola pole design for a quadrupole strength of -0.5 T/m, with asymptotes at $y = 0$ and $x = -\frac{B_1}{B_2}$. The red square in the left figure is the region displayed in the right figure, which corresponds to the aperture width of the MB.

The yoke directs and shapes the magnetic field generated by the coils. Figure 18 presents the three common designs for resistive magnets: C-shaped, H-shaped, and O-shaped, each

differentiated by their unique yoke configurations. The C-shaped magnet provides convenient access to the beam pipe for maintenance, though this results in a slight asymmetry, which compromises field quality. In contrast, the H-shaped magnet eliminates this asymmetry and offers a more compact and mechanically stable design. With its wide enclosed poles, the O-shaped geometry offers the highest field quality and requires less material than the H-shaped design. However, since the available aperture height is limited, fitting the coils poses a challenge. Additionally, the coils must be bent up and down to avoid the beam path, complicating their construction.

Despite these limitations, the O-shaped geometry is selected for superior field quality. As instrumentation inside the dipole is not required, limited access to the beam pipe is not considered a significant drawback.
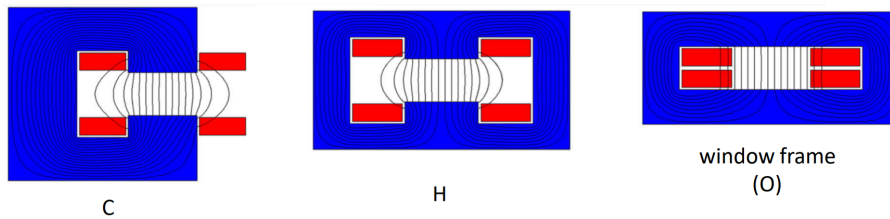
Figure 18: Cartoon representation of the most common types of resistive dipoles, the C-shape (left), H-shape (middle) and O-shape / window frame (right) [20]. The magnetic yokes are in blue, the coils are in red, and the magnetic field lines are also displayed.

The pole width is determined through an iterative process to satisfy the GFR's requirements for field quality. Due to the hyperbolic profile of the poles, the RFD achieved on the left and right sides of the GFR is not uniform. Cut-outs were introduced on either side of the aperture to address this. After several iterations, the aperture width was finalized at 200 mm. Moreover, a triangular cut-out measuring 10.5 mm in width and 20 mm in height was added. In contrast, a cut-out on the other side did not improve the RFD.

The portion of the yoke responsible for guiding the magnetic flux back through the magnetic circuit is known as the return leg. The width of the return leg is designed to ensure that the material remains in the high permeability region, effectively minimizing saturation losses. For a peak magnetic field of 1.35 T, the width of the return leg is given by:

$$w_{\text{leg}} = \frac{B_1}{2} \frac{w_{\text{pole}} + 1.2h}{B_{\text{leg}}} = 0.174\text{m}, \tag{28}$$

rounded up to 175 mm. Consequently, the MB has an overall width of 1050 mm and a height of 420 mm, as depicted in Figure 19. It can also be seen that material from the corners and the middle of the yoke has been removed compared to Figure 18, as it did not contribute to the magnetic field in the aperture.

The space allocated for the coils, 250 mm, exceeds the actual coil width of 206.4 mm. This additional space is necessary to accommodate the difference in bending radius between the coils and the iron yoke, as will be depicted later.

5.2 Coil Design

The MB coil is constructed using a copper conductor with an internal cooling channel through which demineralized water flows to cool the magnet effectively. The cooling water velocity is limited to a maximum of 3.0 m/s to prevent erosion [20]. Additionally, the design imposes a maximum current density of 10 A/mm^2 [28] and allows a pressure drop of up to 10 bars across each of the cooling circuits [20]. The MB will have two coils; figure 20 shows a single layer.
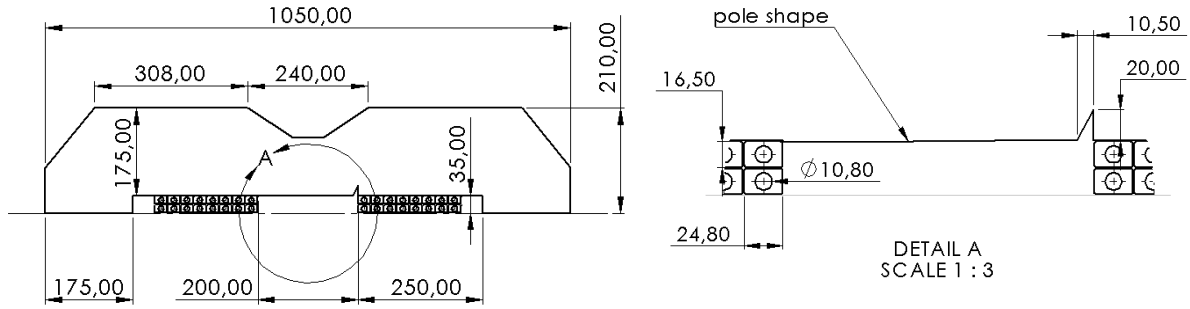
Figure 19: Half of the cross-section of the MB in the middle of the yoke, with the pole shape determined through Equation 25. The left side corresponds to the inner, concave side of the yoke.
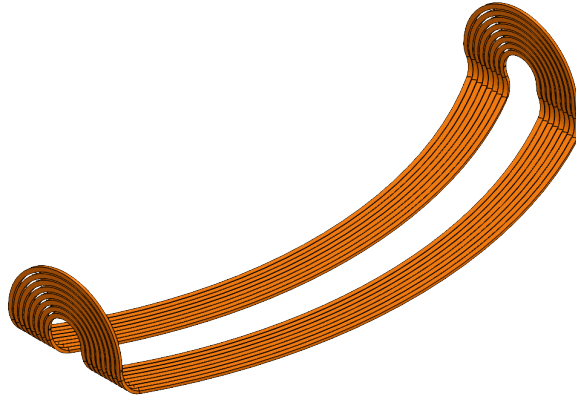

Figure 20: A single coil layer of the MB, note the asymmetries between the power lead and the return lead are not considered.

The coil height is constrained to half the aperture height, resulting in a maximum coil height of 35 mm. Initially, the feasibility of using a single layer of copper conductors was explored. The design satisfied all the requirements. However, the minimum bending radius must be at least three times the conductor height to avoid excessive mechanical stresses. Consequently, more space would be required outside the yoke to bend the conductor.

Instead, a two-layer coil configuration was selected, with a conductor height, h_c, of 16.5 mm and an additional insulation layer of 0.5 mm. Alternative designs using smaller conductors with more layers were also explored. However, these configurations failed to meet cooling requirements. The smaller cooling ducts and increased conductor length would necessitate a higher water velocity and cause a significant pressure drop over the cooling circuits. Moreover, a square conductor shape proved unsuitable for meeting the current density requirements. Consequently, a rectangular conductor with a width, c_w, of 24.8 mm was selected. The corners of the conductor are rounded with a corner radius, R_c, of 1.5 mm. The diameter of the internal cooling duct, d_c, is 10.8 mm, allowing the heat to be removed from the system. The conductor and coil dimensions are summarized in Tables 5 and 6. The conductor will be insulated with a 0.5 mm thick layer. This insulation could, for example, consist of a combination of two layers of 50 µm thick polyimide tape and three layers of 130 µm thick glass fibre tape.

Table 5: Dimensions of conductor

Conductor height, h_c [mm]	16.5
Conductor width, w_c [mm]	24.8
Conductor diameter, d_c [mm]	10.8
Conductor corner radius, R_c [mm]	1.5
Conductor cross-sectional area, A_c [mm]	316

Table 6: Dimensions of coil

Coil height [mm]	35
Coil width [mm]	206
Layers per coil	2
Turns per coil	16
Length coil, l_{coil} [m]	127

The MB must be designed to operate continuously at a peak magnetic field strength of 1.65 T, necessary for the extraction of helium ions. The total Ampere-turns required to achieve this field is

$$NI = \frac{B_1 h}{\eta \mu_0} = 97.7\,\text{kA},\tag{29}$$

where N is the total number of turns, η represents the magnet's efficiency, and μ_0 is the permeability of free space, with a value of $4\pi \times 10^{-7}$ Tm/A. The dipole field strength of 1.65 T causes the yoke to saturate, reducing efficiency. Therefore, the magnetic efficiency is set to 0.93. With 32 total turns across both coils, the current I is calculated as 3.1 kA. The resulting current density of 9.66 A/mm^2 is based on the conductor's cross-sectional area, provided in Table 5.

The inlet and outlet temperatures of the demineralized cooling water, T_{in} and T_{out}, are 20 °C and 50 °C respectively. The average temperature T_{avg} is then 35 °C. At this temperature, the resistivity ρ is 1.82×10^{-8} Ωm. Since the coils are powered in series, see Figure 112 in Appendix D, the electrical resistance over the magnet is

$$R = \frac{2\rho l_{coil}}{A_c} = 13.5\,\text{m}\Omega.\tag{30}$$

The resistive power that has to be dissipated via cooling is

$$P = RI^2 = 127\,\text{kW}.\tag{31}$$

The required flow rate to cool both coils is

$$q = \frac{P}{c_p \rho \Delta T} = 60.8\,\text{L/min},\tag{32}$$

where c_p is the specific heat capacity of water at T_{avg} and ρ is the density of water at T_{avg}. There are two layers per coil, and each layer is cooled separately for a total of four cooling circuits, depicted in Figure 113 in Appendix D. The total flow rate per cooling circuit is 15.2 L/min. The water velocity required to transport 15.2 L/min through a round tube is

$$v = \frac{q}{\pi d_c^2} = 2.77\,\text{m/s}.\tag{33}$$

The corresponding Reynolds number is

$$Re = \frac{\nu d}{v} = 4.1 \times 10^4,\tag{34}$$

where ν denotes the kinematic viscosity of water at T_{avg}. Finally, the pressure drop across a cooling circuit, which is half the length of the coil, is computed using the Darcy-Weisbach equation

$$\Delta p = f \frac{l_{coil}}{2d_c} \frac{\rho v^2}{2},\tag{35}$$

where ρ is the density of water at T_{avg}. The dimensionless friction factor f for fully developed turbulent flow depends on the Reynolds number. For the Reynolds number range $2 \times 10^4 < Re \leq 2 \times 10^6$ [29], the friction factor is given by:

$$f = \frac{0.184}{Re^{0.2}}. \tag{36}$$

By substituting this into Equation 35, the pressure drop across the cooling circuit is calculated to be 4.6bar. The key parameters of the MB are summarized in Table 7. Achieving the necessary balance between maximum water velocity, pressure drop, and current density required a detailed and iterative process. This complexity arose from the combined effects of the magnet's relatively large aperture height, which increases power dissipation, the reduced magnetic efficiency caused by magnetic saturation, and the large cooling circuits necessitated by the magnet's size.

Table 7: Main parameters of the MB at 1.65 T, the magnetic field strength for extracting helium ions.

Number of magnets	6
Bending angle [deg]	60
Bending radius [mm]	2737
Magnetic length [mm]	2866
Dipole field strength [T]	1.65
Quadrupole field strength [T/m]	0.50
Aperture height [mm]	70
Current [kA]	3.1
Total turns [-]	32
Conductor size	16.5 x 24.8, $\varnothing$10.8
Current density [A/m^2]	9.66
Resistance [mΩ]	13.5
Power [kW]	127
Water velocity [m/s]	2.77
Reynolds number [-]	4.1×10^4
Pressure drop [bar]	4.6

5.3   Material Selection

Given the nominal flux density of 1.65 T at the centre of the gap, the magnetic design must account for iron saturation, which varies depending on the type of electrical steel used. While 1010 steel has been used, cold-rolled, non-grain-oriented electrical steel sheets are more common. Silicon is added to these electrical steels to reduce resistivity and hysteresis losses. Figure 21 illustrates the B-H curves for three materials: M15 (corresponding to M250-35A according to the European Standard EN 10106:2015 [30]), M27 (M330-50A), and 1010 steel (a plain carbon steel with 0.10% carbon content). Although the labels 35A and 50A in the plot refer to different thicknesses, the material's properties are consistent in 2D simulations. The cross-sectional design shown in Figure 19 was simulated in Ansys Maxwell 2D using these different materials for the yoke and at different currents. Figure 22 illustrates the resulting dipole field strengths from these simulations.

The transfer functions corresponding to the applied current and the resulting dipole field strengths are determined using Equation 29 and are illustrated in Figure 23. The results indicate that the materials are still well below saturation at lower currents up to 2.0 kA, with efficiencies close to 100%. However, at the peak current of 3.1 kA, M15 and ST1010 exhibit
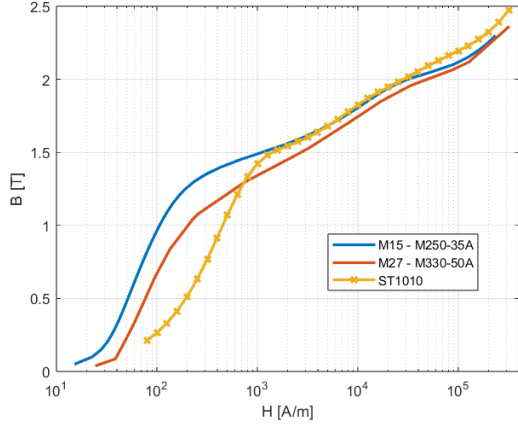
Figure 21: B-H curves for the three materials considered, M15, M27 and ST1010.
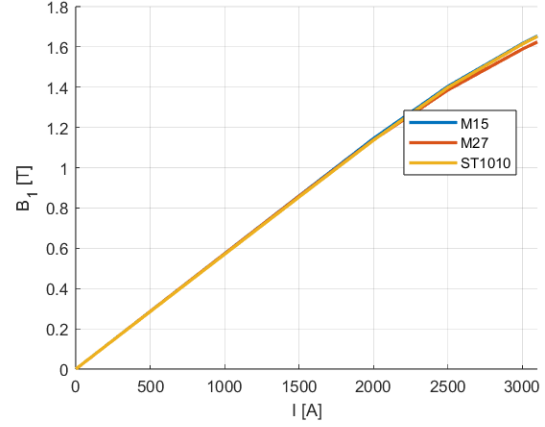
Figure 22: The magnetic field strength B_1 as a function of the current for M15, M27 and ST1010.

comparable efficiencies of 92.8%, while M27 shows the lowest efficiency at 91.2%. M15 is selected as the optimal material due to its superior performance at lower current levels over the other two materials.

Using the data for M15 from Figure 22, the operational currents are determined to reach the magnetic field strengths required for the different particles at injection and extraction from Table 2. These results are summarized in Table 8.
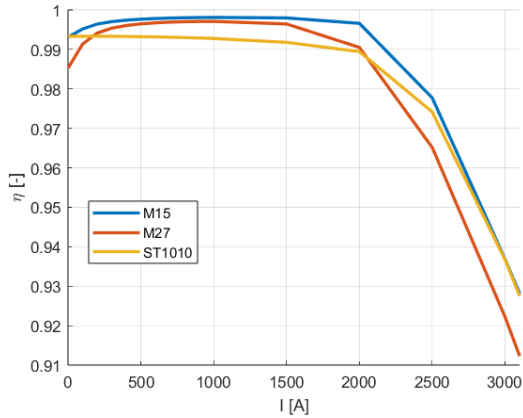
Figure 23: The transfer functions for M15, M27 and ST1010.

Table 8: The required currents to reach the corresponding dipole field strength for the different particles at injection and extraction.

	B_1 [T]	I [kA]
Proton injection	0.167	0.29
Proton extraction	1.63	3.0
Helium injection	0.236	0.42
Helium extraction	1.65	3.1
Carbon injection	0.236	0.42
Carbon extraction	2.42	8.3

5.4   Field Quality

The design depicted in Figure 19 is imported into Ansys Maxwell 2D. An even symmetry boundary condition is applied on the horizontal plane, meaning the magnetic flux is normal to this plane. The magnitude of the magnetic flux density in the yoke is depicted in Figure 24.
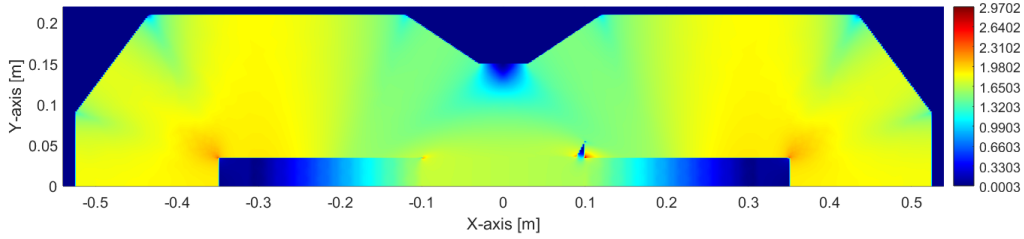
Figure 24: Magnitude of the magnetic field density, with a maximum of 2.97 T and minimum of 0 T. The left side corresponds to the inner, concave side of the yoke.
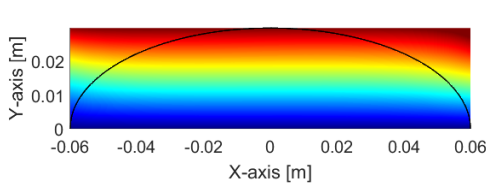
Figure 25: The B_x component in the aperture, with the GFR depicted by a black line.
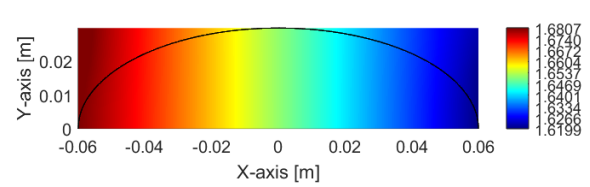
Figure 26: The B_y component in the aperture, with the GFR depicted by a black line.

Figures 25 and 26 illustrate the magnetic field components in the x and y directions. Within the GFR, these field components remain constant along the x-axis for B_x and along the y-axis for B_y, resulting from the quadrupole component introduced by the pole's geometry. The allowed multipoles are calculated in a MATLAB script based on a FEMM 4.2 script from Atillio Milanese as shown in the CAS course on "Normal- and Superconducting Magnets" [31]. Table 9 presents the multipoles corresponding to the magnetic field within the R_s region. The dipole field reaches a strength of 1.65 T, and the quadrupole field strength is -0.507 T/m, both corresponding to the design specifications. The SNM without the dipole and quadrupole fields is 0.10, far exceeding the requirement of less than 5. It is important to note that this simulation in 2D is a reasonably accurate assumption for the field inside the body of the MB. However, the magnetic fields in the ends will significantly contribute to the unwanted multipoles. The ideal field components are derived using the values of B_1 and B_2 as the only non-zero terms in Equation 3. The resulting RFD, shown in Figure 27, is at a maximum of 4.5×10^{-4} within the GFR.
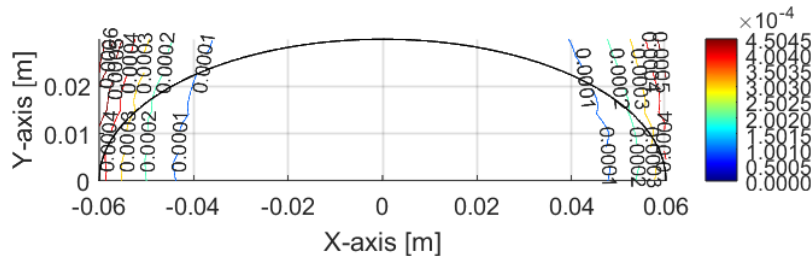
Figure 27: The RFD over the GFR at 1.65 T, the magnetic field strength required to extract helium ions.

The cross-sectional design of Figure 19 meets both the SNM and the RFD requirements at a magnetic field strength of 1.65 T. The same approach is undertaken to evaluate the field quality

Table 9: The allowed multipoles describing the magnetic field at 1.65 T, R_s is 30 mm, R_{ref} is 20 mm.

n	B_n [T/m^{n-1}]	b_n [-]
1	1.6514e+00	1.0000e+04
2	-5.0659e−01	-6.1355e+01
3	1.3308e−01	3.2236e−02
4	6.6447e−01	3.2190e−02
5	-3.6440e+01	-3.5306e−02
6	4.1284e+01	8.1733e−04
7	-9.2621e+03	-3.5896e−03
8	-7.9156e+03	-6.1355e−05
9	-1.1891e+06	-1.8434e−04
10	-2.8286e+06	-8.7700e−06
11	-1.8877e+09	-1.1706e−04
12	6.3397e+09	7.8624e−06
13	-1.8991e+12	-4.7104e−05
14	6.1752e+12	3.0634e−06
15	8.0779e+14	8.0146e−06

at the magnetic field strengths required for injecting and extracting protons, helium ions and carbon ions, according to Table 8. The RFD is depicted in Figures 88 to 91 in Appendix A. The maxima of the RFD over the GFR and the SNM are summarized in Table 10. The field quality of the magnetic fields required for the injection and extraction of protons and helium ions is within the requirements. However, achieving the dipole field strength of 2.42 T to extract carbon ions leads to significant iron saturation. This, coupled with the curved pole shape optimized for operation at 1.65 T and -0.50 T/m, results in a substantial degradation of field quality. Since this upgrade to carbon therapy is planned for a future phase, the issue is not currently considered critical. Instead of a copper conductor, a superconducting coil is required to supply the necessary current to prevent cooling problems. In this upgrade, the pole could be reshaped to improve the field quality.

Table 10: Results of the maximum RFD and the SNM in the GFR for different magnetic field strengths.

	B_1 [T]	RFD in 10^{-4}	$\sum_{n=3}^{15} |b_n|$
Proton injection	0.167	4.3	0.11
Proton extraction	1.63	4.4	0.077
Helium injection	0.236	4.5	0.092
Helium extraction	1.65	4.5	0.10
Carbon injection	0.236	4.4	0.092
Carbon extraction	2.42	94	14

5.5   Complete Design

With a satisfactory cross-sectional design, the design can now be assessed in three dimensions. The integrated fields, magnetic lengths, and field quality at both injection and extraction energy will be evaluated through simulations. Special attention is given to the effects of iron saturation at the pole tips at the ends of the yoke. Two cross-sections of the assembled coils and yoke can be seen in Figures 28 and 29.

The yoke is composed of 1 mm thick laminations stacked side by side, around a radius of 2.737 m, corresponding to the bending radius, depicted in Figure 30. The coil turns are curved around
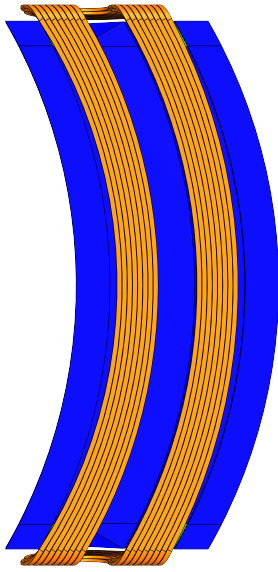
Figure 28: Horizontal cross-section of the MB's yoke and coil assembled.
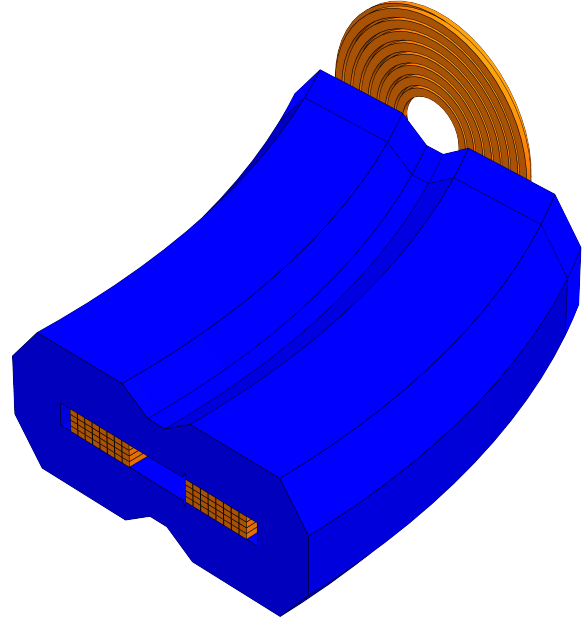
Figure 29: Vertical cross-section of the MB's yoke and coil assembled.

a central point corresponding to the bending radius of the inside of the aperture. This results in a larger outer radius than the inner radius for each turn. The cumulative effect leads to a bending radius of 2.524 m on the inner side of the coil and 2.949 m on the outer side, as illustrated in Figure 31.
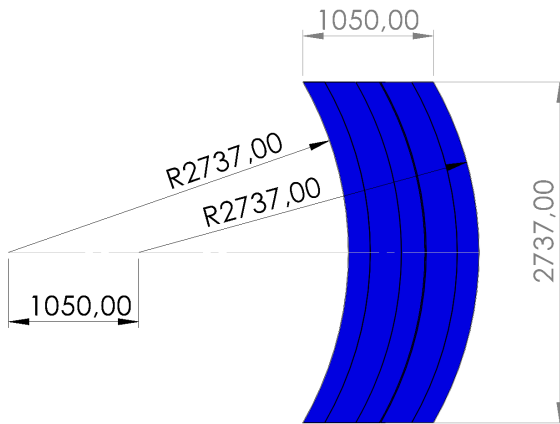
Figure 30: The yoke is made up of laminations stacked around a curve with a radius of 2737 mm.
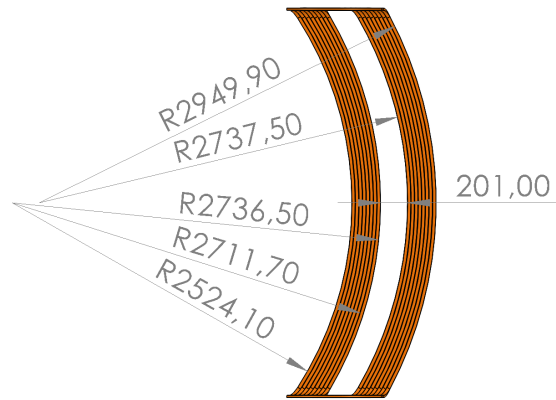
Figure 31: Bending radii of different turns in a single coil. The inner (concave) side of the coil is rotated around a point 200 mm left of the point around which the outer (convex) side is rotated.

The laminations are separated by a 30 µm thick non-magnetic insulation layer, epoxy, resulting in a stacking factor of

$$\lambda = \frac{t_{Fe}}{t_{Fe} + t_{ins}} = 0.97. \tag{37}$$

Since the stacking factor is high, it has a minimal impact on the magnetic field within the gap. Meanwhile, the eddy current losses are effectively reduced, thereby enhancing the magnet's overall efficiency during ramping. The yoke's total weight is 7.3 tonnes, and the two coils

combined weigh 711 kg, leading to a fully assembled weight of at least 8.0 tonnes.

5.6   Integrated Field Quality

Evaluating the field quality in three dimensions for a curved magnet is challenging. As stated before in Section 2.1, the harmonics can only be determined when the magnetic field is independent of z or by taking the integral over the field components when the limits are independent of z. In the body of the magnet, the field is dependent on z, meaning the integral has to be taken from $-\infty$ to ∞. This increases the simulation time and is thus unwanted.

Instead, a local coordinate system will be defined based on a reference trajectory $R(s)$. This reference trajectory is on the horizontal mid-plane of the magnet, depicted in Figure 32. It starts at the vertical mid-plane with $s = 0$ and follows a trajectory in the middle of the aperture. This is a circular path with a radius of 2.737 m. It continues straight when it crosses the boundary between the yoke and the outside, at s_1. The local coordinate system is defined as $(u(s), v, w(s))$, where $u(s)$ is both perpendicular to s and y, v is independent of s and thus equal to y, and w is parallel to s and perpendicular to y. At $s = 0$, (u, v, w) is equal to (x, y, z). With this local coordinate system, the magnetic field within the body is independent of w. The magnetic field components are expressed in B_u, B_v and B_w, and the integrals are taken over s from $s = 0$ to $s = s_1 + 0.5$ m. It is expected that 0.5 m is enough for the magnitude of the magnetic field to approach zero. Only one-fourth of the design is simulated in Ansys Maxwell 3D. The resulting magnetic field strength at $y = 0$ can be seen in Figure 33. The magnetic field components inside the GFR are expressed in the local coordinate system and are displayed in Figures 34 to 36.
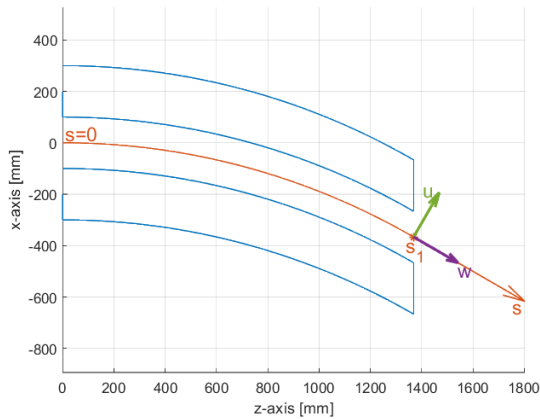
Figure 32: Reference trajectory (s) along the mid-plane ($y = 0$) of the MB. The return legs are blue. The local coordinate system is shown at s_1.
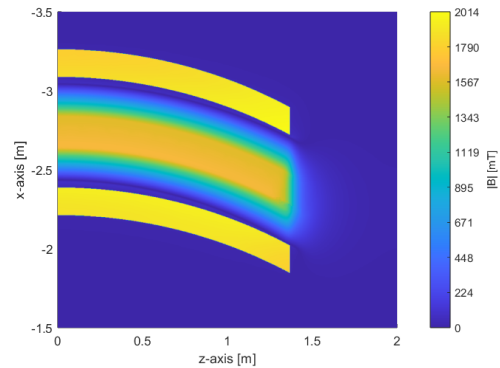
Figure 33: Magnetic field strength over the horizontal mid-plane of the magnet; note the coordinate system from Ansys Maxwell is shown.
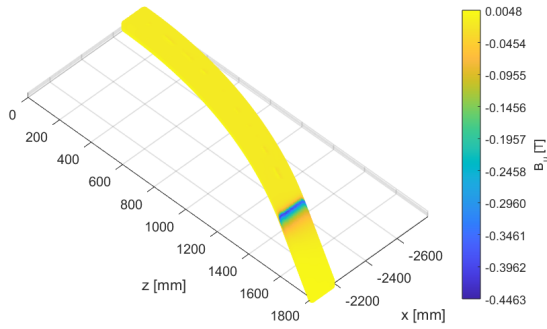
Figure 34: B_u plotted over the GFR; note the coordinate system from Ansys Maxwell is shown.
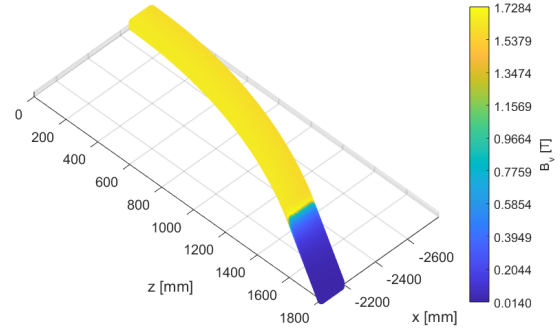
Figure 35: B_v plotted over the GFR; note the coordinate system from Ansys Maxwell is shown.
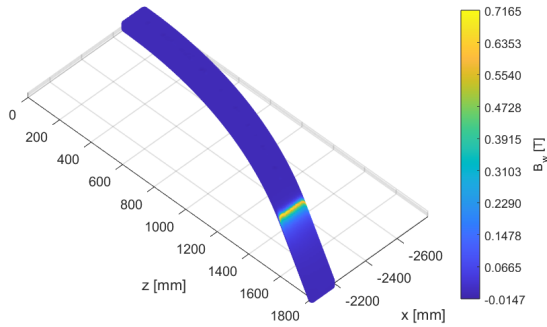
Figure 36: B_w plotted over the GFR; note the coordinate system from Ansys Maxwell is shown.
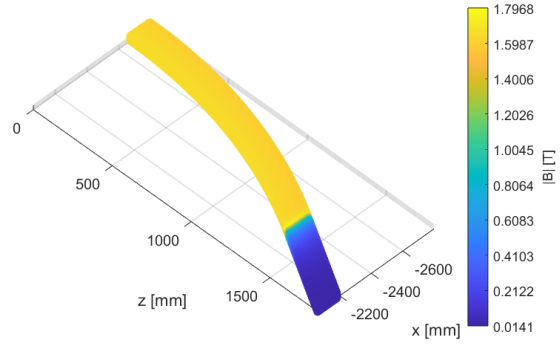
Figure 37: $|B|$ plotted over the GFR; note the coordinate system from Ansys Maxwell is shown.

In Figures 33 and 37, it is shown that in the body, the magnetic field strength is constant along s. However, at s_1, there is a steep drop-off; this can also be seen in Figure 38. The slight peak in B_1 just before s_1 results from the saturation in the pole tip near the end. The B_2 is also calculated along the reference trajectory, depicted in Figure 39. At s_1, there is a significant peak of 11 T/m. This can largely be attributed to the 30-degree pole face angle. The reason for this becomes clear when considering that the multipoles are evaluated in the uv-plane, perpendicular to the beam's path. At s_1, the plane lies both outside the magnet and inside the magnet. This difference causes a substantial variation in the magnetic field strength, leading to the observed peak in the B_2 component. Such a large peak is unwanted, and the integrated B_2 component is too large, -1.63 T compared to a target of -1.26 T.

One approach is to decrease the current to reduce the integrated B_2 component, but this simultaneously impacts the integrated B_1 component, which is undesirable. A more effective solution involves modifying the pole shape at the end of the magnet's yoke using shims, which strategically remove material to achieve the desired magnetic field profile.

    Various approaches have been implemented in similar combined-function magnets to address this issue. For instance, in the ELETTRA dipoles, the two-dimensional profile of the magnet was precision-machined along its entire length based on a reference curvature radius. In this design, no chamfers were included, but the magnets underwent individual shimming based on precise magnetic measurements. In a specific magnet, two shims were added to each pole end, embedded in a brass holder that was bolted onto the end plate to fine-tune the magnetic field [32, 33]. In more recent machines, such as those at ALBA and CLS, a different approach was
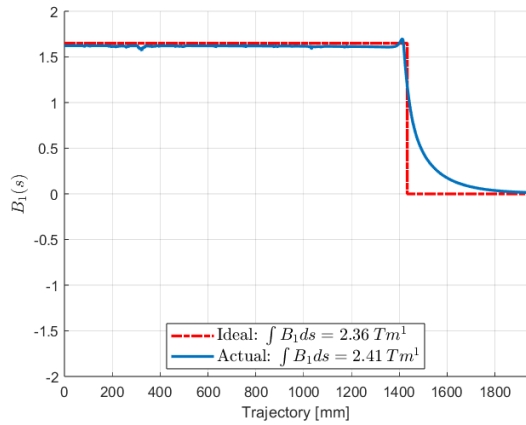
Figure 38: The B_1 component along the reference trajectory, where the ideal case is a constant B_1 of 1.65 T inside, which drops to zero at s_1.
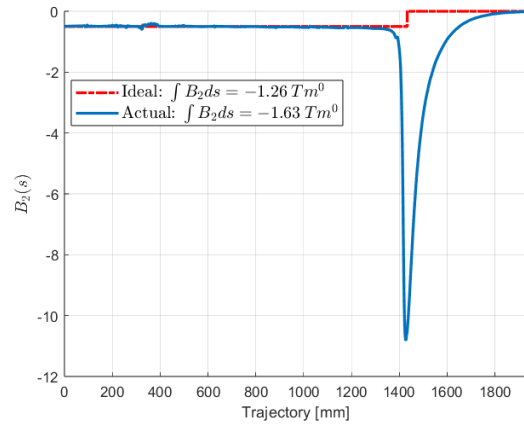
Figure 39: The B_2 component along the reference trajectory, where the ideal case is a constant B_2 of -0.5 T inside, which drops to zero at s_1.

adopted. Instead of relying solely on shimming, these designs incorporated a chamfer with a slight rotation of the pole face to achieve better field homogeneity and control over the magnetic components [34–36]. These shimming methods represent a shift towards more sophisticated techniques in modern magnet design, offering greater precision in tailoring the magnetic field, particularly at the pole ends. This approach will also be used to design the MB's shim.

The shims will machined out of a specially design part, the end plate. The shim features a chamfer on the pole with a 45° angle. This chamfer is defined by the shim angle, which represents the inclination between the chamfer and the side of the end plate. The shim angle ranges from 0° to 40°and is represented in Figure 40. The shim thickness is defined as the length of a vector normal to the shim plane and the point $(u(s_1), 35, (w(s_1))$ mm, it ranges from 0 to 60 mm.
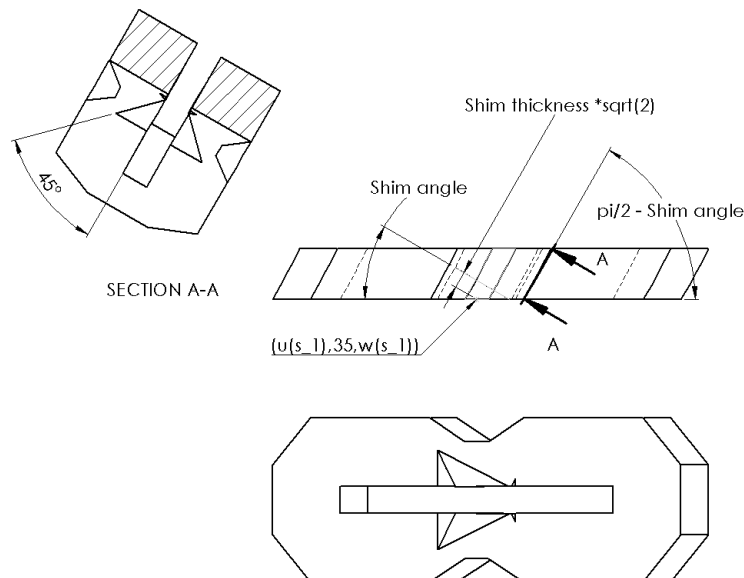
Figure 40: The shim design in the end plate. The shim consists of a chamfer with a 45° angle relative to the horizontal plane (top left). The shim thickness is the distance between the chamfer and the point $(u(s_1), 35, (w(s_1))$ mm and the shim angle is the angle between the side of the end plate and the chamfer.
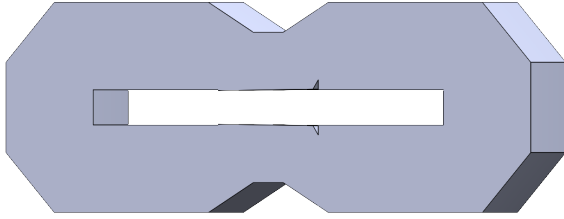
Figure 41: End plate with no shim.
.
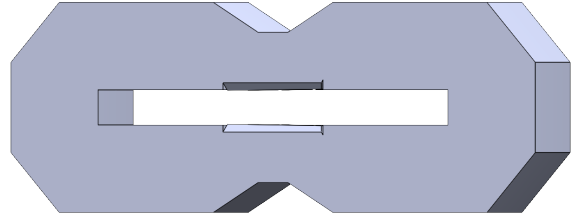
Figure 42: End plate with a zero° shim angle and thickness of 10 mm.
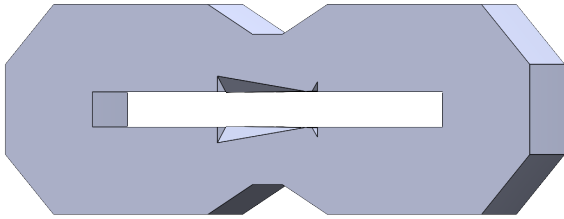
Figure 43: End plate with a 10° shim angle and thickness of 10 mm.
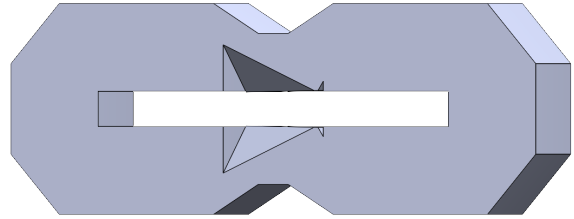
Figure 44: End plate with a 30° shim angle and thickness of 30 mm.

All the different shims were simulated in Ansys Maxwell 3D, and the integrated B_1 and B_2 components were calculated. In Figure 45, it can be seen that the shim angle hardly influences the integrated B_1 component. Moreover, the shim thickness only has a limited effect, with approximately reducing the integrated B_1 component by 0.012 Tm per 10 mm. In contrast, the integrated B_2 component is significantly affected by the shim angle and less by the shim thickness, shown in Figure 46.
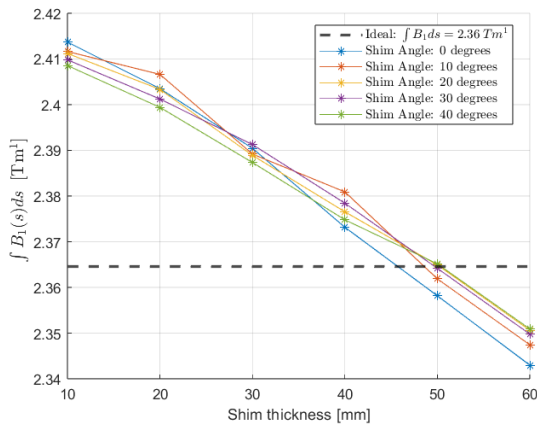
Figure 45: Integrated B_1 component for shims with different angles and thicknesses.
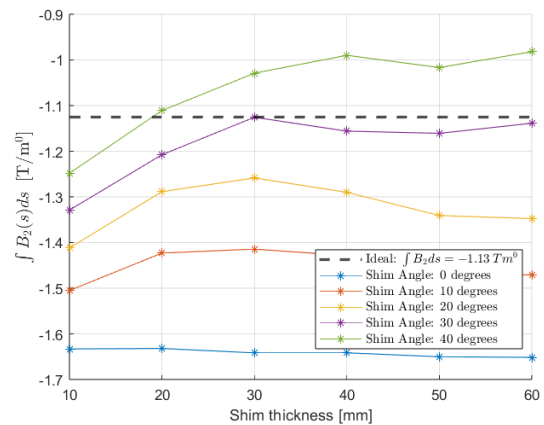
Figure 46: Integrated B_2 component for shims with different angles and thicknesses.

It was decided to go for a shim with an angle of 30° and a 30 mm thickness. For this shim design, the integrated B_1 is 2.39 Tm, within 1% of the requirements, and the integrated B_2 component is equal to the requirement of 1.13 T. The shape of the shim is depicted in Figure 44. In Figures 47 and 48 the resulting B_1 and B_2 along the reference trajectory are shown. Finally, Figure 49 depicts the magnitude of the magnetic field in the mid-plane. Compared to Figure 33, the effect of the shim is most apparent in the GFR region at the end of the yoke.
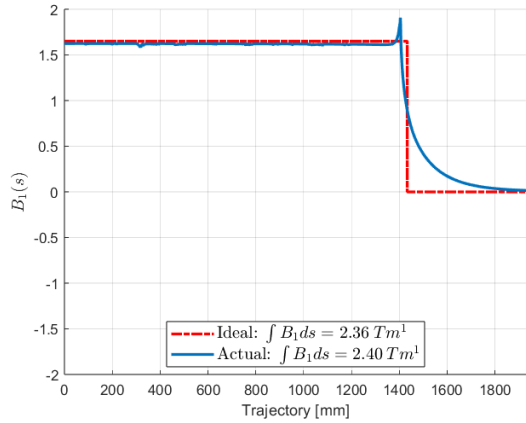
Figure 47: The B_1 component along the reference trajectory.
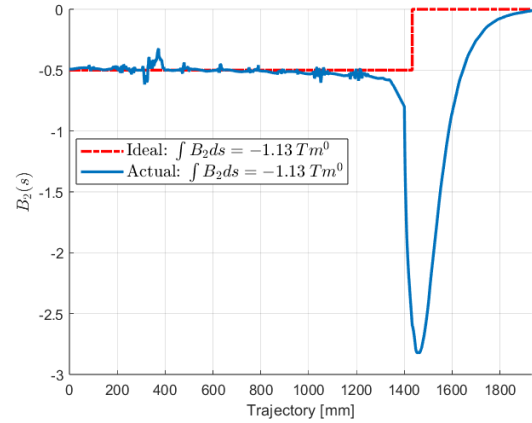
Figure 48: The B_2 component along the reference trajectory.
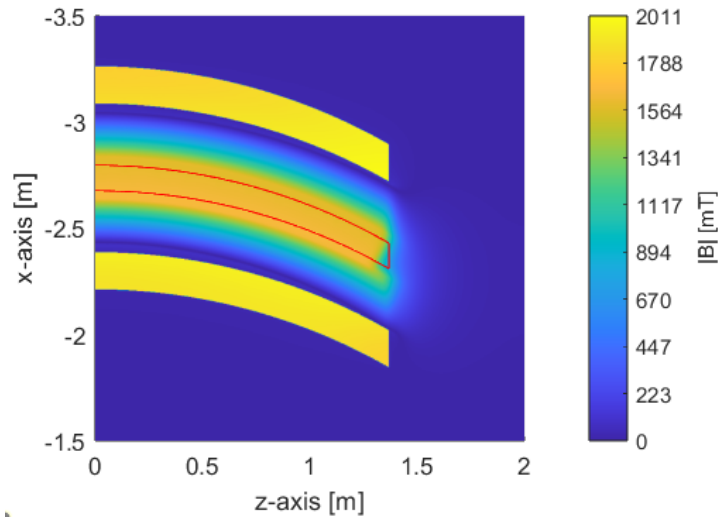
Figure 49: Magnetic field strength over the horizontal mid-plane of the magnet, note the coordinates are based on Maxwell. The red line denotes the area for the GFR.

The field quality is assessed by integrating the magnetic field components, expressed in the local coordinate system, over the trajectory. Using this approach, the integrated radial field distortion RFD is calculated as per Equation 15. Figure 50 illustrates the results, showing a peak value of 5.2×10^{-4} within the Good Field Region (GFR), which slightly exceeds the target threshold of less than 5. Additionally, the integrated multipoles are evaluated using Equations 5 and 6. The corresponding results are presented in Table 11. The SNM is 8.90, surpassing the required limit of less than 5.

Although these results do not fully meet the specifications, the decision was made to forgo further design refinements and proceed with the development of the other magnets.
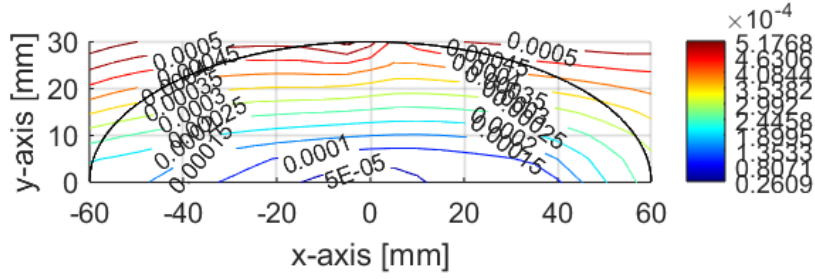
Figure 50: The integrated RFD over the GFR.

Table 11: The integrated multipoles for the MB design with a shim of 30° and a thickness of 30 mm.

	$\int B_n \, ds \; [\mathrm{T/m}^{n-2}]$	$\int b_n \; [\text{-}]$
n = 1	2.3913e+00	1.0000e+04
n = 2	-1.1256e+00	-2.6649e+02
n = 3	-1.6449e+00	-3.7537e+00
n = 4	2.4634e+01	9.3583e−01
n = 5	-3.9040e+03	-1.4543e+00
n = 6	2.2114e+04	2.1282e−01
n = 7	1.7440e+05	-2.1187e−01
n = 8	-7.0223e+06	-4.9266e−02
n = 9	-5.8766e+08	-2.6084e−02
n = 10	-1.3236e+10	-6.4729e−02
n = 11	6.5246e+11	2.9342e−02
n = 12	-1.7301e+13	-3.7110e−02
n = 13	9.6639e+12	1.0405e−02
n = 14	-8.8130e+15	-1.3080e−02
n = 15	3.2315e+17	3.8550e−03

6   Design Quadrupoles

This section will explore the design and operation of the three quadrupole magnets used in the system: the MQB, MQF, and MQD. While the MQB and MQF share the same structural design, they operate at different currents, leading to separate magnet strengths. For this reason, the separate nomenclature will be continued. The electromagnetic specifications and design considerations will be discussed. The final design for the MQB and MQF is shown in Figure 51 and for the MQB in Figure 52.
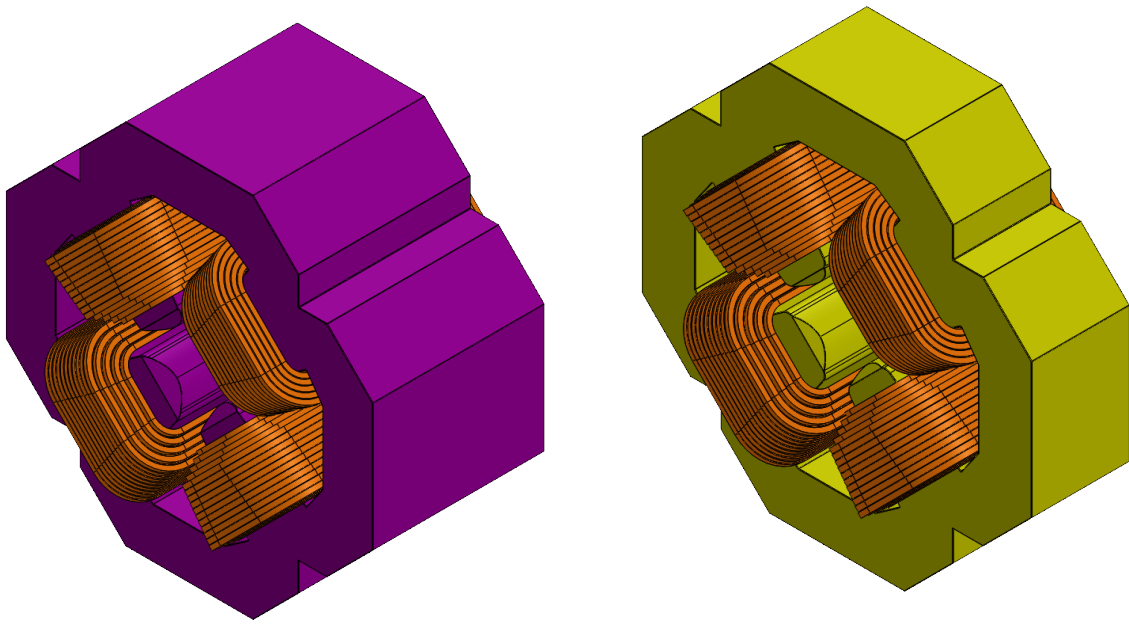
Figure 51: The final design of the MQB and MQF magnets, featuring a purple yoke and four orange coils. The applied shim on the pole is depicted.

Figure 52: The final design of the MQD magnet, featuring a yellow yoke and four orange coils. The applied shim on the pole is depicted as well.

The magnetic flux density at the pole tip of a quadrupole, B_{pole}, is typically limited to 0.80 T [20]. While it is possible to operate with a higher pole tip field — such as the quadrupoles in the Super Proton Synchrotron (SPS) at CERN, which operates at 1.0 T — this results in reduced magnetic efficiency due to saturation of the iron within the poles. The aperture radius, h_0, of the quadrupoles is 65.4 mm, leading to a maximum quadrupole strength of

$$\max(B_2) = \frac{\max(B_{\mathrm{pole}})}{h_0} = 12.23 \ \mathrm{T/m}. \tag{38}$$

The minimum magnetic lengths required to generate a sufficiently strong integrated quadrupole strength,

$$\min(L_{\mathrm{mag}}) = \frac{\int B_2 \, ds}{\max(B_2)}. \tag{39}$$

These lengths are rounded up to the nearest multiple of five, yielding magnetic lengths of 400 mm, 380 mm, and 235 mm for the MQB, MQF, and MQD quadrupoles, respectively. As previously noted, the MQB and MQF share the same magnet design; thus, both will have a magnetic length of 400 mm. The final magnetic lengths, along with the corresponding magnet strengths and magnetic flux densities at the pole tips, are presented in Table 12.

The ampere-turns in a quadrupole depend on the magnetic field strength and aperture radius:

$$NI = \frac{B_2 h_0^2}{2\eta\mu_0}.$$
(40)

A conservative value of 0.95 is used for magnetic efficiency, resulting in excitation currents of 22.0 kA for the MQB, 20.8 kA for the MQF, and -21.8 kA for the MQD. A copper conductor provides the required current through a cross-sectional area of 8.8 x 8.8 mm, featuring a 1.0 mm corner radius. The conductor also includes an internal cooling channel with a diameter of 4.2 mm and an area A_{cc} of 13.9 mm^2. The total cross-sectional area of the copper conductor, A_c, is 62.7 mm^2, with 1.0 mm thick insulation between turns. The maximum current density, $j_{\max}$, is set to 5.5 A/mm^{2}allowing each turn to carry up to 345 A. This requires a minimum of 64 turns for the MQB, 61 turns for the MQF, and 64 turns for the MQD. Each quadrupole coil is designed with five turns per layer and a total of fifteen layers. After eleven layers, the number of turns decreases by one per layer, resulting in 65 total turns; see Figure 53.

The operating currents are calculated to be 338 A for the MQB, 320 A for the MQF, and -335 A for the MQD. The total length of the copper conductor per coil is 77.4 m for both the MQB and MQF quadrupoles and 55.9 m for the MQD quadrupole. Similar to the MB, the coils are powered in series but are cooled in parallel; see Figures 114 and 115 in Appendix D. The resulting electrical and cooling parameters, calculated using Equations 30 to 35, are summarized in Table 12. It should be noted that the Reynolds number falls outside the specified range for Equation 36. Therefore, the following friction factor is used to calculate the pressure drop:

$$f = \frac{0.316}{Re^{0.25}},$$
(41)

which is valid for $3 \times 10^3 < Re \leq 2 \times 10^4$ [37].

Table 12: Summary of main properties for MQB, MQF, and MQD.

	MQB	MQF	MQD
$\int B_2\, ds$ [T]	4.90	4.64	-2.85
h_0 [mm]		65.4	
L_{mag} [mm]		400	235
B_2 [T/m]	12.26	11.61	-12.15
N [-]		65	65
I [A]	338	320	-335
j [A/mm^2]	5.4	5.1	-5.3
L_{Fe} [mm]		356.4	191.4
L_{co} [m]		78	57
ρ [mΩ]		88	645
P_{Magnet} [kW]	10	9.0	7.1
Q_{Magnet} [l/min]	4.8	4.3	3.4
# Cooling Circuits [-]		4	
v [m/s]	1.5	1.3	1.0
Re [-]	7.6e3	6.8e3	5.4e3
ΔP [bar]	6.6	5.4	2.6

6.1   Pole Design

The ideal pole shape for a quadrupole would be a hyperbola going from zero to infinity,

$$xy = \frac{h_0^2}{2}.$$
(42)

However, this is unrealistically large, and there is no space for the coils. Instead, the poles will end at a specific cut-off point (x_c, y_c) and shims will be added to improve the field quality. The shims compensate for this loss of material by adding more material closer to the pole. Tanabe [38] gives two equations for determining this cut-off point for an optimized (with shims) and unoptimized (without shims) quadrupole:

$$x_c = h_0 \sqrt{\frac{1}{2}\sqrt{\left(\rho_0^2 - c\right)^2 + 1} + \frac{1}{2}\left(\rho_0^2 - c\right)} \tag{43}$$

$$y_c = h_0 \sqrt{\frac{1}{2}\sqrt{\left(\rho_0^2 - c\right)^2 + 1} - \frac{1}{2}\left(\rho_0^2 - c\right)} \tag{44}$$

where h_0 is the pole radius, $\rho_0 = \frac{r_0}{h_0}$ is the normalized good field region with r_0 being the good field region radius. This good field region encompasses the maximum beam envelope from Table 4. The constant c is dependent on whether or not the pole profile has been optimized with shims or truncates abruptly:

$$c_{unoptimized} = -0.36 \ln \frac{\Delta B}{B} - 0.90, \tag{45}$$

$$c_{optimized} = -0.14 \ln \frac{\Delta B}{B} - 0.25. \tag{46}$$

The poles will be optimized and should have a RFD of 10^{-4}. Since the design choice has been made to use the same pole profile for all quadrupoles, the largest cut-off point will be used to ensure good field quality for all the quadrupoles. This results in a cut-off point with the coordinates $(86.0, 24.9)$ mm. From here, the quadrupoles are designed using a parametric model, similar to the quadrupoles for the CERN Neutrino to Gran Sasso transfer line [39]. This technique can easily change the pole shape by varying only a few parameters so that optimization can be done fairly quickly. The parameters for the yoke, see Figure 54, are the aperture radius, h_0 (which determines the hyperbola), the cut-off point (x_c, y_c), the length of line A, the radius of circle C, the angle and length of line B, the length of line D, and the return yoke thickness. The final parameter is the space between the coils and the yoke; see Figure 53. The coil height and width equal the number of layers and turns times the conductor height and width with 1 mm insulation. The main region of the pole area is designed as a hyperbola, which creates a linear gradient from the magnet's centre outward. Line A, tangent to the hyperbola on its left and the circle on its right, acts as a shim to increase the gradient at the edge of the good field region. A circle is used to transition into the tapered coil window to ensure a smooth transition and avoid sharp edges, where flux line concentration and saturation effects could occur.
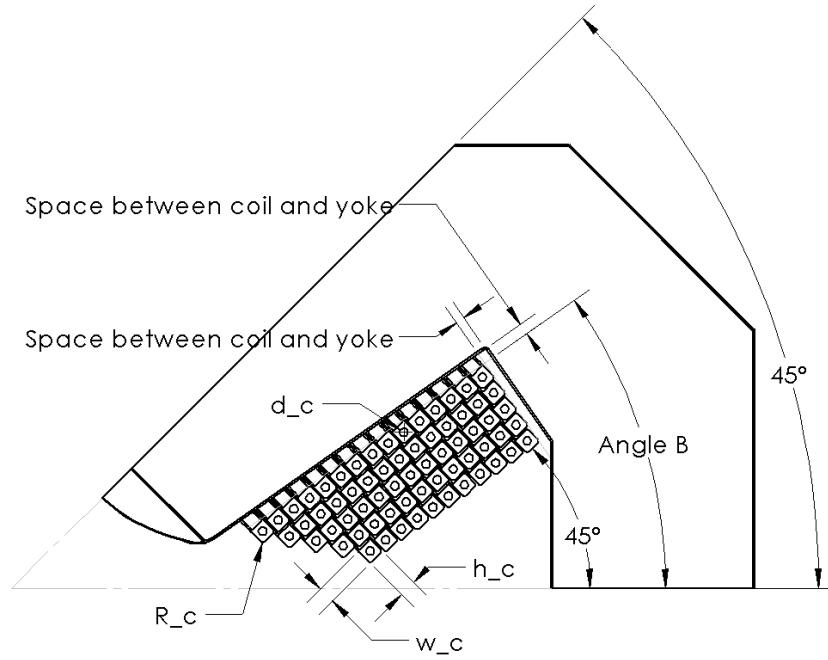
Figure 53: Parametric design of the coil of the quadrupoles; note the conductors in the coil are at a 45° angle, which is different to angle B.
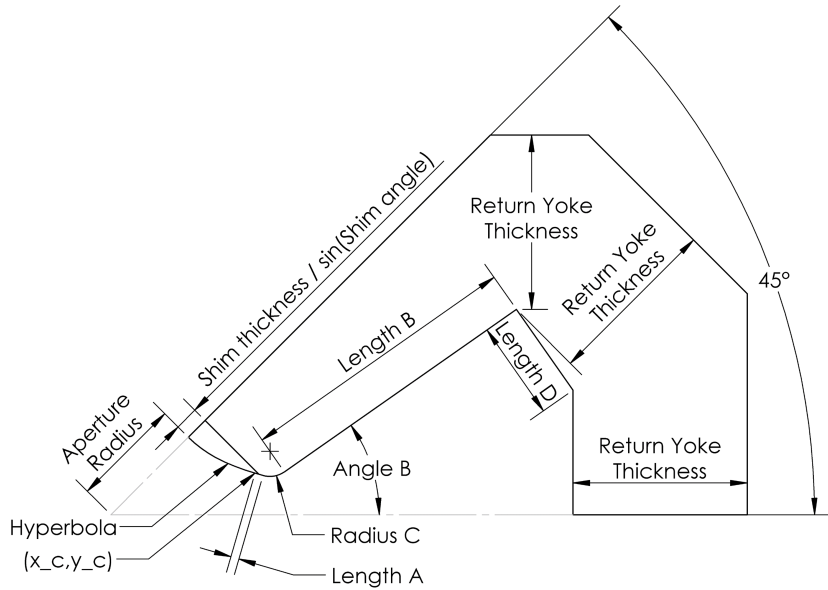
Figure 54: Parametric design of the yoke of the quadrupoles.

The optimization aims to achieve an RFD of 1×10^{-4}, similar to the value for the cut-off point. As previously stated, the RFD is defined as the difference between the magnetic and ideal magnetic fields, normalized by the ideal magnetic field. However, for a quadrupole magnet, the perfect field at the centre is 0 T. Therefore, the RFD is normalized with regards to B_2:

$$\frac{|\Delta B|}{|B|}(x,y) = \frac{\left| \begin{bmatrix} B_x(x,y) \\ B_y(x,y) \end{bmatrix} - B_2 \begin{bmatrix} y \\ x \end{bmatrix} \right|}{|B_2|}. \tag{47}$$

The optimization is done in FEMM 4.2 through MATLAB, which allows for a quick and simple

analysis of the results. Quadrupoles have a rotational symmetry order of 4; thus, only one-eight of the total model has to be modelled. The boundary conditions from Figure 8 are applied. The optimized values for the parameters are summarized in Table 13.

Table 13: Final values of the design variables of the quadrupoles.

Variable	Value
length A [mm]	5
radius C [mm]	15
angle B [deg]	35
length B [mm]	1.15*Coil Height
length D [mm]	1.2*Coil width
width return yoke [mm]	104
space between coil and yoke [mm]	6

The amplitude of the magnetic flux density corresponding to the optimized values is shown in Figures 55 and 56, for the aperture and yoke.
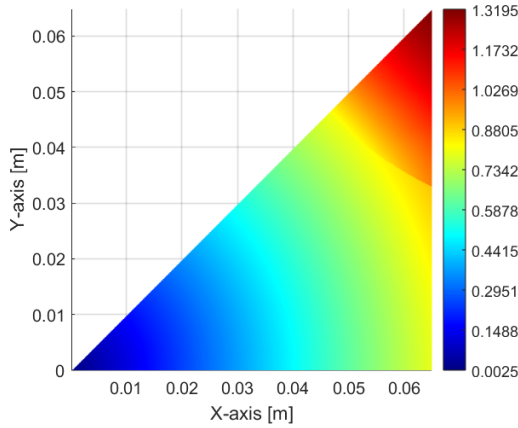
Figure 55: The amplitude of the magnetic flux density in the aperture corresponding to the current of the MQB.
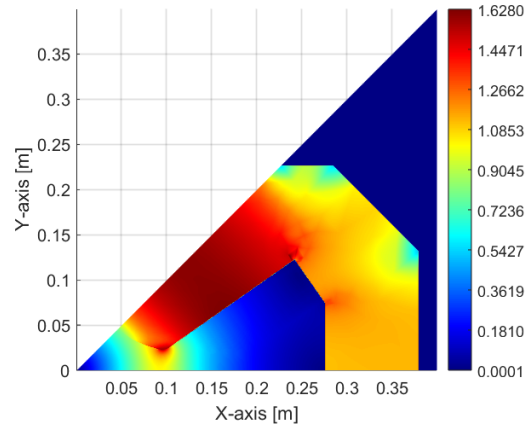
Figure 56: The amplitude of the magnetic flux density in the yoke corresponding to the current of the MQB.

The RFD in the GFR is depicted in Figure 57, with a peak of 1.1×10^{-4}. This is close to the value of the cut-off point. The corresponding allowed multipoles are shown in Table 14. From this, it is clear that the B_2 overperforms with a value of 12.8 instead of 12.2 T/m. Thus, the magnetic efficiency was estimated to be low, confirmed in Figure 58. For the 3D simulations, the current is reduced to 332.9 A. Finally, the sum of the allowed multipoles is less than 5, as per the requirements.

Table 14: The allowed multipoles of the MQB, with R_{ref} is 40 mm.

n	B_n [T/m^{n-1}]	b_n [-]
2	1.2789e+01	10000
6	-1.8439e+02	-3.9503
10	-7.8176e+07	-0.4287
14	-5.1485e+11	-0.0072
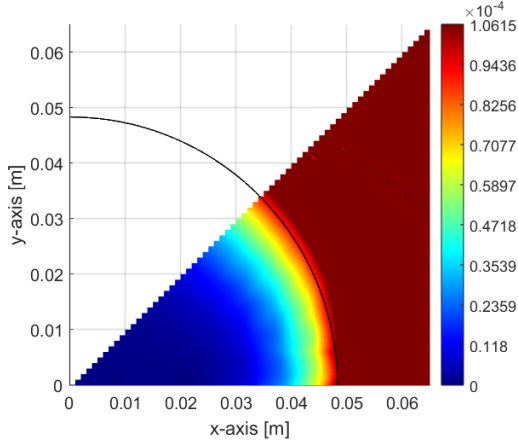
Figure 57: RFD in the GFR of the MQB the maximum is 1.06×10^{-4}.
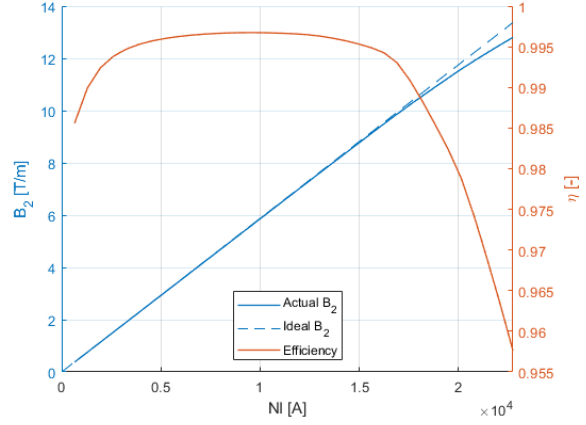
Figure 58: Transfer function of the B_2 component and the corresponding magnetic efficiency.

6.2   Complete Design

The 2D cross-section from Figure 54 and 53 corresponding to the values from Table 13, is extended to the yoke length:

$$l_{yoke} = l_{mag} - \frac{2}{3}h_0. \tag{48}$$

This is 356.4 mm for the MQB and MQF and 191.4 mm for the MQD. The coils are shaped around the pole ends, with a minimum bending radius of three times the conductor width. The final coil-to-coil length is 489.9 mm for the MQB and MQF and 324.9 mm for the MQD. Only one-sixteenth of the complete design will be simulated, depicted in Figures 59 and 60. The same boundary conditions are applied as in 2D, adding the Neumann boundary condition on the vertical plane perpendicular to the trajectory in the magnet's middle. Both designs were simulated in Ansys Maxwell 3D but only at the currents required for the MQB and MQD. With its lower operation current, it is assumed that the MQF performs at least as well as the MQB.

The resulting integrated B_2 component for the MQB and MQD is 2.56 T and -1.47 T, slightly overperforming. However, the sum of the normalized multipoles is too high, 16 and 24, respectively. This will be combated by shimming the poles. The design for the shim can be seen in Figure 61. The initial shim angle ranges from 15 to 75 degrees in steps of 15 degrees, and the
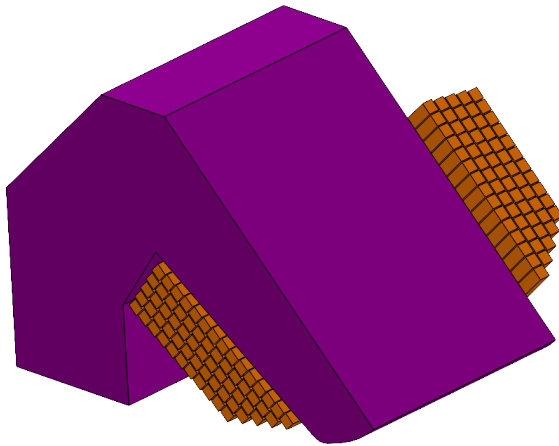
Figure 59: One-sixteenth of the MQB & MQF magnet, simulated in Ansys Maxwell.
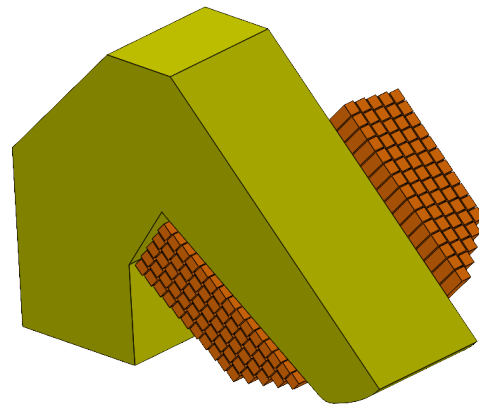
Figure 60: One-sixteenth of the MQD magnet, simulated in Ansys Maxwell.
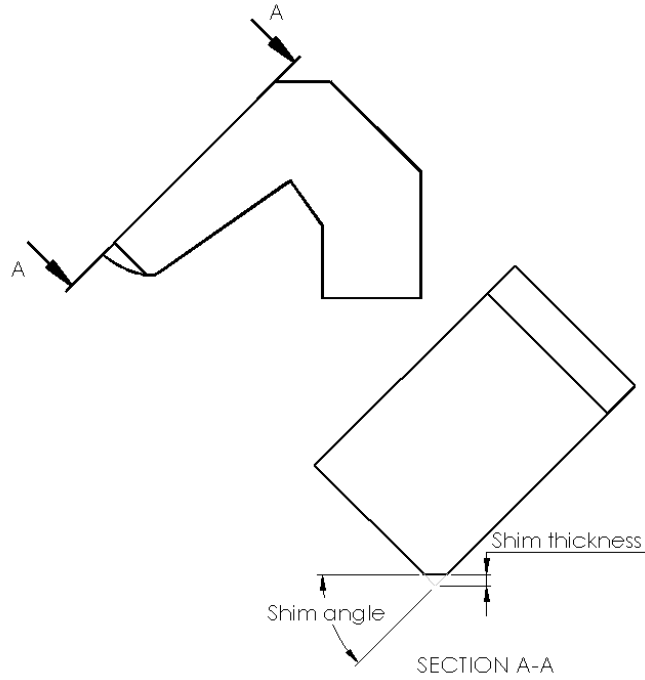
Figure 61: Drawing of the shim design of the quadrupoles, dependent on the shim thickness and shim angle.

thickness from 5 to 15 mm in steps of 5 mm.

The resulting integrated B_2 components for the MQB and MQD can be seen in Figures 62 and 63. By increasing the shim thickness, the integrated B_2 component decreases; note that for the MQD, the integrated B_2 component is negative. Moreover, the MQB meets the requirement of an integrated B_2 component of 2.54 T for almost all the shim designs. However, the MQD only meets the requirement of an integrated B_2 component of -1.43 T for shims with a thickness at most 10 mm. Finally, the shim angle of 45° seems to perform the best compared to the other shim angles at similar thicknesses.
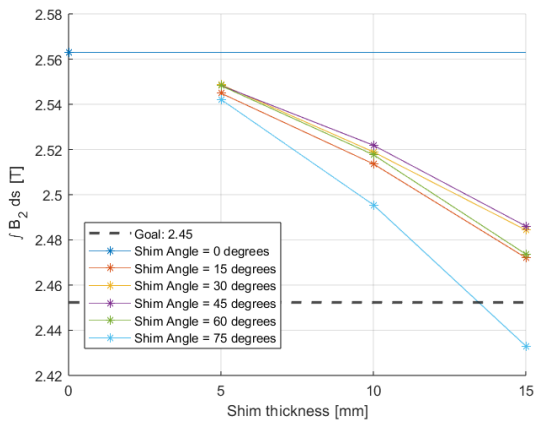
Figure 62: The integrated quadrupole field strength of the MQB with different shim angles and thicknesses.
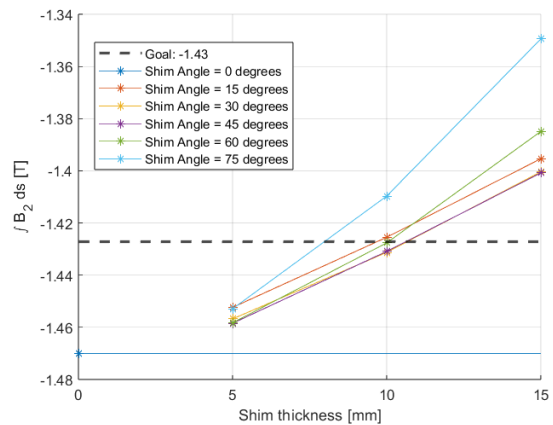
Figure 63: The integrated quadrupole field strength of the MQD with different shim angles and thicknesses.

The resulting sum of the normalized multipoles is shown in Figures 64 and 65. Only a few

shim designs meet the requirement of having a sum of integrated normalized multipoles below 5. The shims with a 45° angle and a 10 and 15 mm thickness perform best for both the MQB and MQD. It was decided to refine the shims further by investigating the results for shims with an angle of 45° and a thickness between 10 and 16 mm.
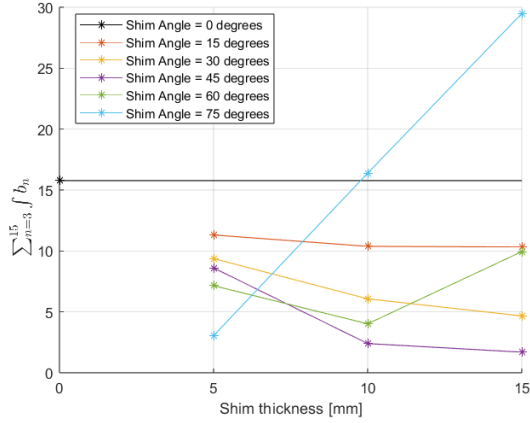
Figure 64: The integrated SNM of the MQB with different shim angles and thicknesses.
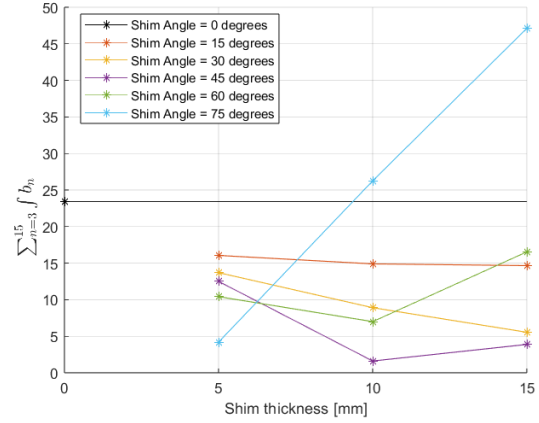
Figure 65: The integrated SNM of the MQD with different shim angles and thicknesses.

The integrated B_2 components for the MQB and MQD are visualised in Figures 66 and 67. The same trend of decreasing integrated B_2 component also holds here. Whereas the MQB meets the produces an integrated quadrupole strength of at least 2.45 T with all thicknesses, the MQD only meets its requirement of -1.43 T for a maximum shim thickness of 12 mm.
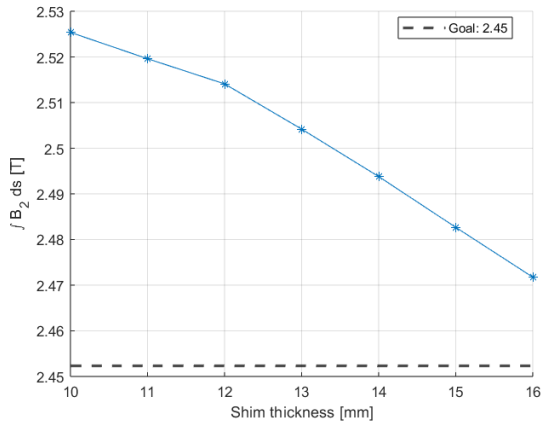
Figure 66: The integrated quadrupole field strength of the MQB with a shim angle of 45° and different shim thicknesses.
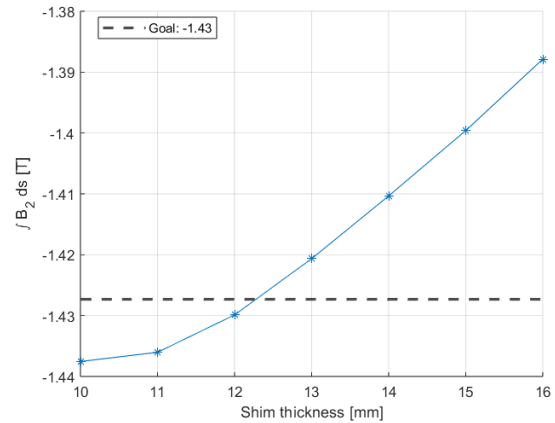
Figure 67: The integrated quadrupole field strength of the MQD with a shim angle of 45° and different shim thicknesses.

The sum of the normalized multipoles for different shim thicknesses is summarized in Figures 68 and 69, for the MQB and MQD respectively. Although it could already be seen in Figures 64 and 65, it is still surprising that for the MQB, the sum of the normalized multipoles decreases with increasing thickness and the opposite is true for the MQD.
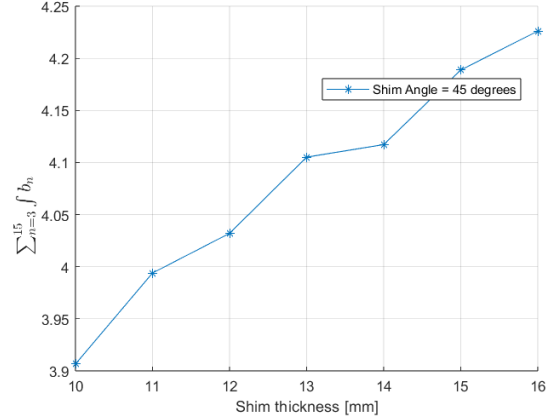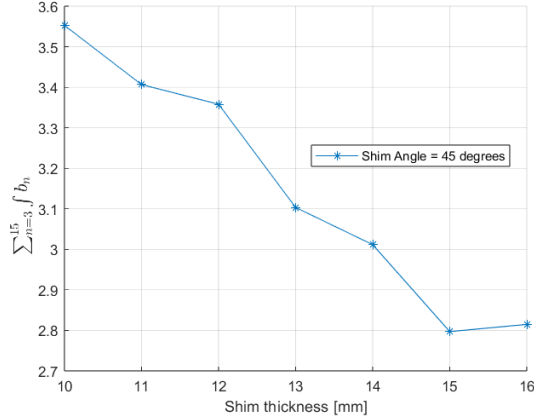
Figure 68: The integrated SNM of the MQD with a shim angle of 45° and different shim thicknesses.

Figure 69: The integrated SNM of the MQB with a shim angle of 45° and different shim thicknesses.

Based on these results, the shim designs for the MQB and MQD will feature a 45° angle and a thickness of 15 and 10 mm, respectively. These yield the lowest sum of normalized multipoles while generating sufficiently strong quadrupole fields. Although a thinner shim might potentially improve performance for the MQD, this option has not been further investigated.

The integrated field components and their magnitudes are shown in Figures 92 to 99 in Appendix B. The integrated RFD has also been evaluated, as seen in Figures 70 and 71, with maximum values of 5.34×10^{-5} for the MQB and 6.5×10^{-5} for the MQD within GFR. Thus, the field quality and the field strength for both quadrupole designs have been met.
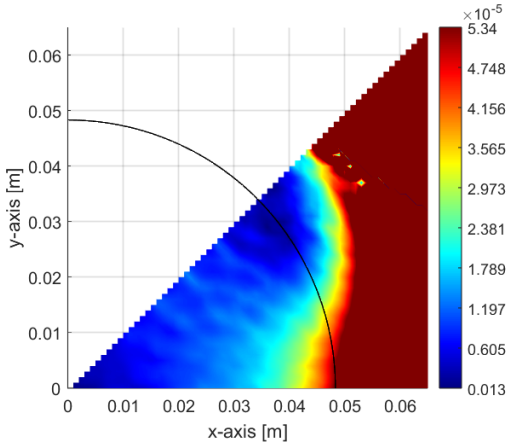
Figure 70: The integrated RFD over the GFR for the MQB.
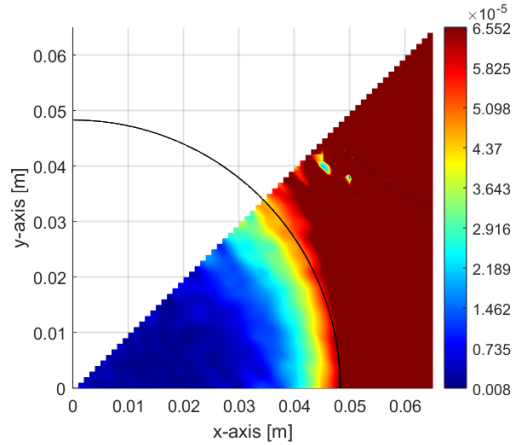
Figure 71: The integrated RFD over the GFR for the MQD.

7   Design of the Sextupole

As previously discussed, the energy distribution of particles within the beam can result in significant deviations from the reference trajectory. Sextupole magnets are designed to correct these deviations, as their magnetic field strength increases quadratically with distance from the centre. Additionally, it was noted that orbit corrector magnets are typically required to steer the beam in either the horizontal or vertical direction, ensuring that the beam follows the correct trajectory despite minor fabrication or alignment errors. However, these orbit corrector magnets are omitted to maintain a compact synchrotron design and reduce both construction and operational costs. Instead, the beam is steered in both the horizontal and vertical directions by adjusting the current applied to specific poles of the sextupole magnets. In accelerators with compact lattices, sextupole magnets are often equipped with horizontal steering, vertical steering, and/or skew quadrupole trim [38].

In this section, the design of the MSX will be discussed. The final assembled design is depicted in Figures 72 and 73; the yoke is green, and the six coils are orange.
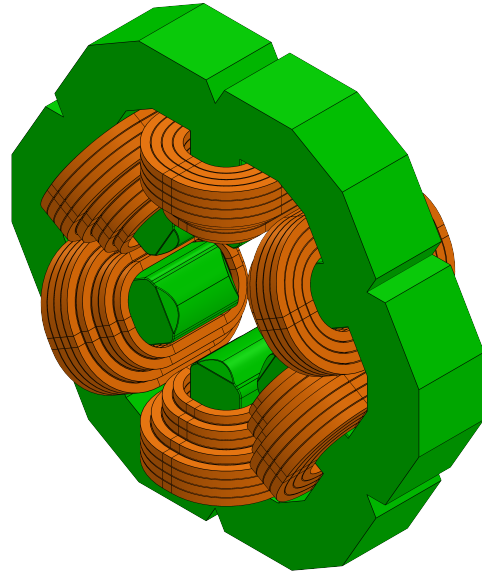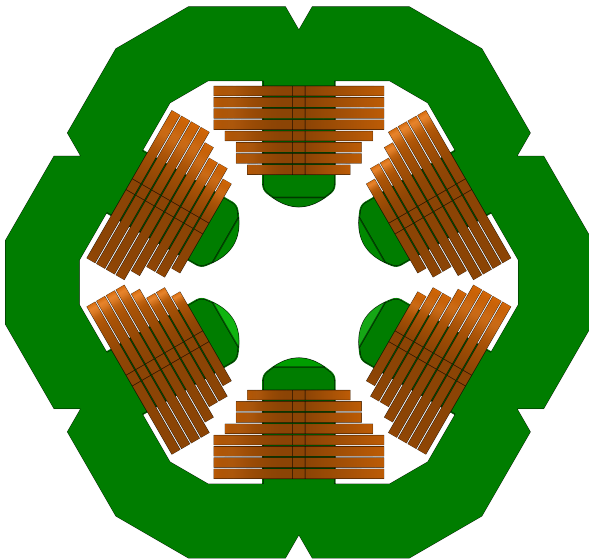
Figure 72: Front view of the assembled MSX.   Figure 73: Isometric view of the assembled MSX.

The peak field at the pole tip B_{pole} is limited to 0.25 T to prevent saturation losses and to maintain consistent field performance across the operational range. Given that there is no space between the MQB and the MSX to modify the beam pipe, the aperture radius h_0 remains fixed at 65.4 mm. This results in a maximum B_3 component of

$$B_3 = \frac{B_{pole}}{h_0^2} = 58.4 \text{ T/m}^2. \tag{49}$$

To achieve an integrated B_3 component of -6.75 T/m, as indicated in Table 3, the corresponding magnetic length is

$$L_{mag} = 115 \text{ mm}. \tag{50}$$

The yoke length is then calculated as

$$L_{yoke} = L_{mag} - \frac{h_0}{2} = 82.3 \text{ mm}. \tag{51}$$

Assuming an efficiency of 0.98, the total ampere-turns required for the MSX is

$$NI = \frac{B_3 h^3}{3\eta\mu_0} = 4.4 \text{ kA}. \tag{52}$$

The current density is limited to a conservative 3.5 A/mm^2. The same copper conductors used in the quadrupoles will also be used in the MSX: 8.8x8.8 $\varnothing$4.2 mm. The cross-sectional area is 62.7 mm^2, giving a maximum allowed current of 219 A, requiring 20 turns. However, to accommodate the additional current necessary for both horizontal and vertical steering, 24 turns are utilized. This adjustment reduces the peak current to 184 A and decreases the current density to 2.94 A/mm^2. The six coils are powered in series, shown in Figure 116, in Appendix D. The total length of the six coils is 64.5 m, resulting in a resistance of 18.4 mΩ and a total power of 0.67 kW. This power is dissipated through the conductor's internal cooling channel. The cooling channels within the coils are also connected in series, depicted in Figure 117 in Appendix D. The cooling parameters, calculated using Equations 32 through 35, are summarized in Table 15.

Table 15: Main parameters of the MSX.

Number of magnets	3
Field gradient [T/m^2]	58.4
Magnetic length [mm]	115
Aperture radius [mm]	65.4
Current [A]	184
Total turns [-]	24
Conductor size [mm]	8.8 x 8.8 $\varnothing$4.2
Current density [A/mm^2]	2.94
Resistance [mΩ]	18.4
Power [kW]	0.67
Water velocity [m/s]	0.39
Reynolds number [-]	4.1e3
Pressure drop [bar]	0.54

The parametric design process for the cross-section of the MSX yoke follows a methodology similar to that used for the quadrupole magnets, with the addition of an extra design variable, the coordinates of the cutoff point (x_c, y_c). The design variables are shown in Figure 74 and determine the coil's position in Figure 75 as well. The equation in this figure refers to the pole shape of the sextupole according to
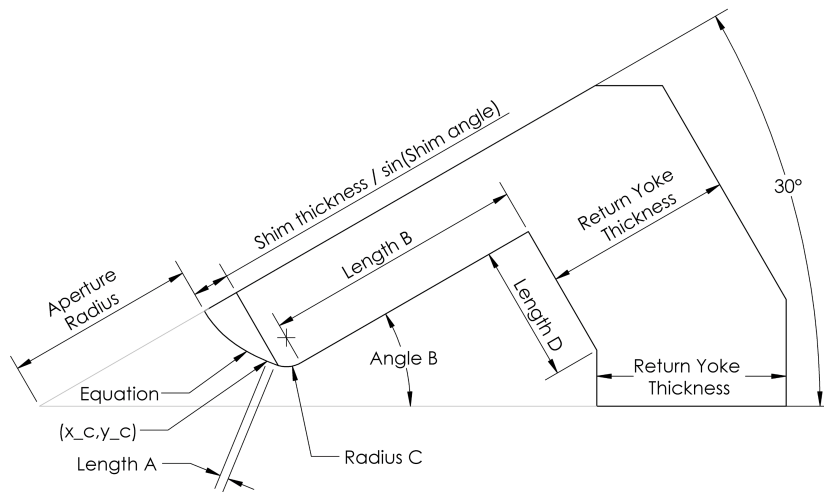
$$3x^2y - y^3 = h_0^2. \tag{53}$$

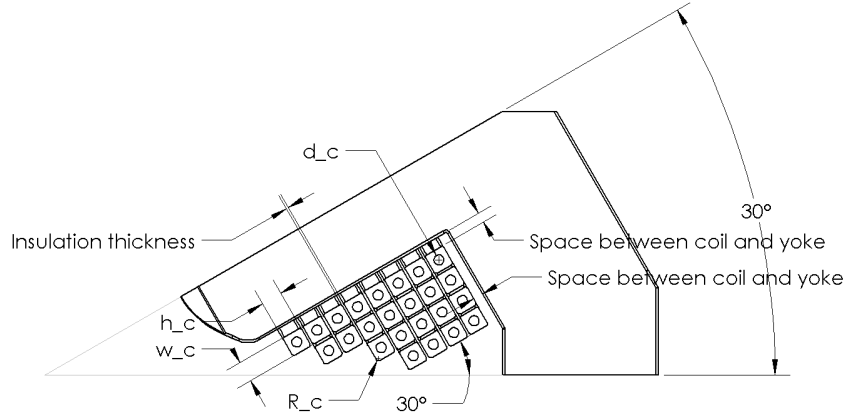Figure 74: Parametric design of the coil of the MSX.

Figure 75: Parametric design of the yoke of the MSX.

Similar to the quadrupole design process, multiple 2D magnetostatic simulations are performed in FEMM 4.2 using these design variables. This software is chosen over Maxwell primarily because it offers seamless integration with MATLAB, enabling direct control of the simulation process and immediate analysis of results. One-twelfth of the MSX cross-sectional design is simulated with the symmetric boundary conditions according to Figure 8. The material selected for the yoke was M27 steel.

The iterative design process aimed to achieve both an RFD and a sum of undesired multipoles below 5×10^{-4}. As previously stated, the RFD is defined as the difference between the magnetic and ideal magnetic fields, normalized by the ideal magnetic field. However, for a sextupole magnet, the perfect field at the centre is 0 T. Therefore, the RFD is normalized with regards to B_3:

$$\frac{|\Delta B|}{|B|}(x,y) = \frac{\left| \begin{bmatrix} B_x(x,y) \\ B_y(x,y) \end{bmatrix} - B_3 \begin{bmatrix} 2xy \\ x^2 - y^2 \end{bmatrix} \right|}{|B_3|}. \tag{54}$$

Table 16 lists the design variables that achieved the targeted field quality. Figure 76 shows the resulting RFD, while the corresponding multipole values are presented in Table 17. Additionally, the magnetic field strengths within the aperture and the yoke are illustrated in Figures 77 and 78, respectively.

Table 16: Final values of the design variables of the MSX.

(x_c, y_c) [mm]	(78.2,15.4)
Length A [mm]	3
Radius C [mm]	10
Angle B [deg]	30
Length B [mm]	1.15*Coil height
Length D [mm]	1.2*Coil width
Return yoke thickness [mm]	65
Space between coil and yoke [mm]	6

Table 17: The allowed multipoles for the MSX with R_{ref} is 40 mm.

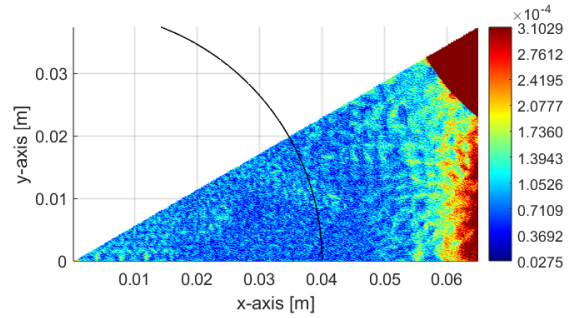|	B_n [T/m^{n1}]	b_n [-]
n = 3	-58.735	10000
n = 9	4.6094e+05	-0.32144
n = 15	5.5200e+12	-0.01576

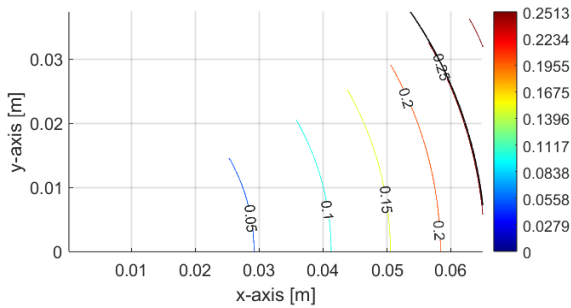Figure 76: The RFD in the aperture of MSX, with a peak of 3.1×10^{-4}.

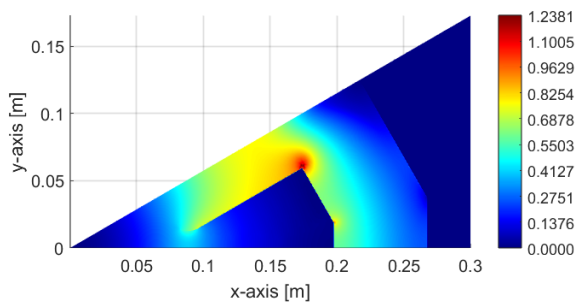Figure 77: Magnetic field strength inside the aperture (black line) of the MSX.

Figure 78: Magnetic field strength over the yoke of the MSX.

7.1   Complete Design

It is important to note that the MSX has a large aperture of 65.4 mm compared to the yoke length of 82.3 mm. This increases the influence of the ends on the overall field quality. Consequently, the focus will be to optimize the 3D design and precisely incorporate shims to enhance the integrated field quality. The cross-sectional design shown in Figure 74 is extended along the entire length of the yoke, yielding a total weight of 82.7 kg. The coils are contoured around the poles with a bending radius of at least three times the conductor width. The coil-to-coil length is 204.4 mm. The total length of the six coils is 64.5 m, with a weight of 35.6 kg. The simulations were conducted on one twenty-fourth of the magnet, as illustrated in Figure 79, applying the same boundary conditions as in the 2D simulation. Additionally, the Neumann boundary condition was imposed on the vertical plane perpendicular to the trajectory in the middle of the magnet. All simulations were performed using Ansys Maxwell 3D.

The integrated B_3 component is calculated to be -3.52 T/m over the trajectory for a R_{ref} of 40 mm. This slight overshoot, compared to the desired -3.38 T/m, is the result of conservatively estimating the magnetic efficiency of the sextupole. The RFD in 3D is based on Equation 15 and divided by the integrated B_3 component:

$$\frac{|\Delta B|}{|B|}(x,y) = \frac{\left| \begin{bmatrix} \int B_x(x,y)\,ds \\ \int B_y(x,y)\,ds \end{bmatrix} - \int B_3\,ds \begin{bmatrix} 2xy \\ x^2 - y^2 \end{bmatrix} \right|}{\left| \int B_3\,ds \right|}. \tag{55}$$
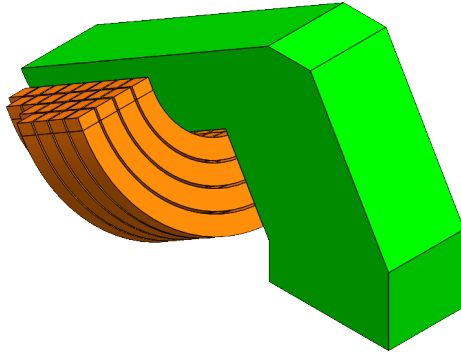
Figure 79: One twenty-fourth of the MSX magnet, simulated in Ansys Maxwell.

It is within the requirements with a maximum value of 3.35×10^{-4} in the GFR. However, the integrated b_9 and b_{15} are too high, with -12.8 and 0.07, respectively. This will be addressed by applying shims to the pole tips. The shims in the simulations will have an angle of 45° and a thickness ranging from 2 to 10 mm in steps of 2 mm; see Figure 80.
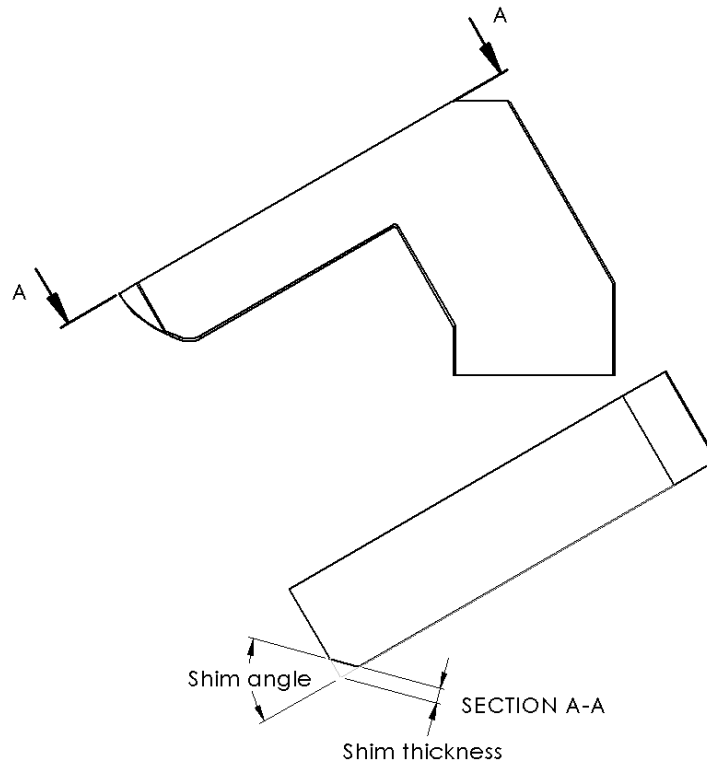

Figure 80: Drawing of the shim design of the MSX, dependent on the shim thickness and shim angle.

Figure 81 shows that for larger shim thicknesses, the integrated B_3 increases from -3.57 T/m without a shim to -3.27 T/m with a shim thickness of 10 mm. An increase is also observed for the integrated b_9 component but not for the b_{15}, shown in Figure 82. Finally, the maximum RFD within the GFR increases; see Figure 83.

Based on these results, shims with a thickness of 6 mm were selected. The integrated B_3 value is now -3.45 T/m, differing by less than 2% from the target of -3.38 T/m. The integrated b_9 component has been nearly eliminated, reduced to -0.28, while b_{15} is now -0.20. The peak homogeneity reaches 3.36×10^{-4}, successfully meeting both field quality requirements. The final design is presented in Figure 73.
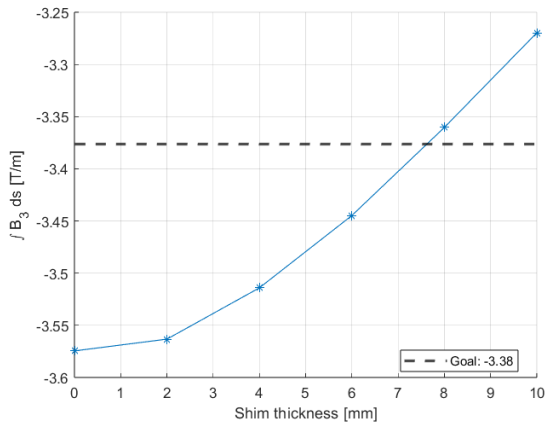
Figure 81: Integrated sextupole fields strength for shims at a 45° angle but with different thicknesses.
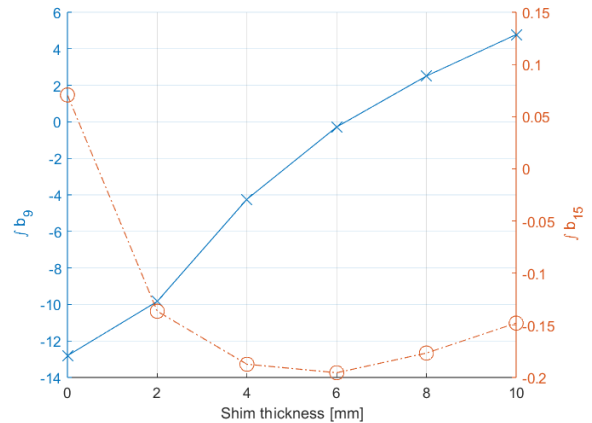
Figure 82: The integrated b_9 and b_{15} or shims at a 45° angle but with different thicknesses.
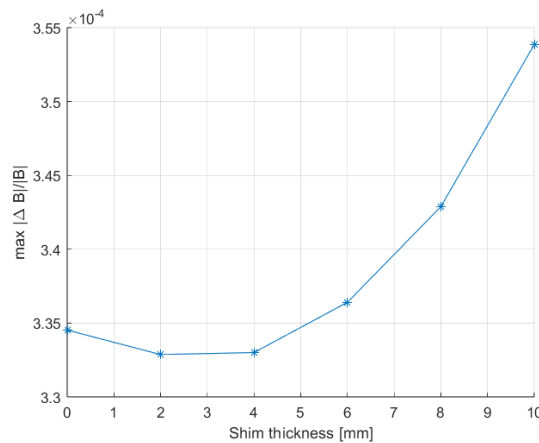

Figure 83: The maximum RFD in the GFR of the MSX for shims with a 45° angle but with different thicknesses.

7.2 Orbit Corrector

With the MSX successfully achieving its primary function as a sextupole, the next step is to explore whether it can also serve as an orbit corrector in both the horizontal (B_1) and vertical (A_1) planes. This is achieved by increasing or decreasing the applied current to specific poles, according to Figure 84. However, the pole geometry of the sextupole is not well suited for generating these fields, leading to high values for the RFD and undesired multipoles.

The operational configurations from Figure 84 can be theoretically analyzed using Halbach's perturbation theory [40]. This demonstrates that such configurations produce orthogonal fields to the harmonics typically associated with a sextupole magnet [40]. This orthogonal arrangement allows for the superposition of various flux distributions, particularly as the flux density remains well below the saturation point [41]. The exact amount of horizontal and vertical steering still needs to be determined. Instead, the goal for the integrated B_1 and A_1 components is set at -1.0 mTm, four times less than the sextupole magnets of SESAME produce [41]. The MSX has a magnetic length of 115 mm, resulting in B_1 and A_1 components of -8.7 mT, respectively.
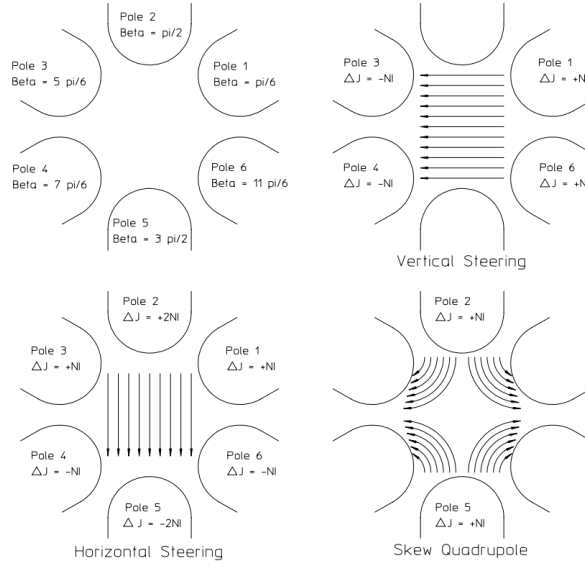
Figure 84: Different sextupole trims, B_3 (top-left), A_1 (top-right), B_1 (bottom-left) and A_2 (bottom-right) [38].

Exciting all six poles achieves horizontal steering, shown in Figure 84. The excitation patterns is $+\Delta J$, $+2\Delta J_h$, $+\Delta J_h$, $-\Delta J_h$, $-2\Delta J_h$ and $-\Delta J_h$ for the poles at $\frac{\pi}{6}$, $\frac{3\pi}{6}$, $\frac{5\pi}{6}$, $\frac{7\pi}{6}$, $\frac{9\pi}{6}$ and $\frac{11\pi}{6}$. The required current is

$$\Delta J_h = \frac{B_1 h}{1.7622 \mu_0 N} = -10.7 \text{ A}. \tag{56}$$

Vertical steering trim is achieved by exciting only four of the six poles. The excitation pattern for the vertical steering trim requires the following currents, $+\Delta J_v$, $-\Delta J_v$, $-\Delta J_v$, $+\Delta J_v$, for the poles at $\frac{\pi}{6}$, $\frac{5\pi}{6}$, $\frac{7\pi}{6}$ and $\frac{11\pi}{6}$, respectively. This requires a current of

$$\Delta J_v = \frac{A_1 h}{1.0173 \mu_0 N} = -18.5 \text{ A}. \tag{57}$$

Table 18 presents the required currents for generating the multipole fields both individually and simultaneously. Notably, there are no dedicated coils for each field; each coil operates at a distinct current. Consequently, the coils cannot be connected in series. A potential future improvement could involve designing independent coils, which would reduce the number of required power supplies.

Table 18: The required currents to generate the respective field strengths.

	$B_3 = 58.4$ T/m^2	$B_1 = -1.0$ mT	$A_1 = -1.0$ mT	B_3, B_1 and A_1 combined
J at $\frac{\pi}{6}$ [A]	184	-10.7	-18.5	155
J at $\frac{3\pi}{6}$ [A]	184	-21.4	0	163
J at $\frac{5\pi}{6}$ [A]	184	-10.7	18.5	192
J at $\frac{7\pi}{6}$ [A]	184	10.7	18.5	213
J at $\frac{9\pi}{6}$ [A]	184	21.4	0	205
J at $\frac{11\pi}{6}$ [A]	184	10.7	-18.5	176

First, the field quality of the horizontal and vertical trims will be analysed independently. With either trim, the MSX acts as a fully symmetric dipole; thus, only one-fourth of the cross-section has to be simulated. The symmetric boundary conditions for a dipole from Figure 8 are applied, as well as the Neumann boundary condition to the vertical plane in the middle of the magnet.

The currents from Table 18 are applied to the corresponding poles from Figure 84. The resulting integrated magnetic field components are depicted in Figures 100 to 107 in the Appendix.

For the horizontal trim the magnetic field in the centre B_y is -8.8 mT, and for the vertical trim the magnetic field in the centre B_x is also -8.8 mT, slightly above the goal of -8.7 mT. The integrated allowed multipoles are summarized in Tables 19 and 20. For both trims the integrated magnetic is -0.70 mTm. As this is only half of the sextupole, it exceeds the goal of -1.0 mTm, meaning that there is a larger contribution from the ends than expected.

Moreover, from Tables 19 and 20, it becomes clear that the sum of the normalized multipoles is far above 5. The integrated b_5 and a_5 components are especially significant, with 643 and -643, respectively. Furthermore, the max RFD within the GFR is 38% for the horizontal trim and 37% for the vertical trim, which is also far above the requirements. However, these coefficients are normalized with respect to the corrector strength, which is small compared to the main sextupole component. And, since the field strengths are so low, any deviation will result in only a minor difference in field strength.

Table 19: Allowed integrated multipoles for the horizontal orbit corrector, $R_{\text{ref}} = 40$ mm.

n	$\int B_n\, ds$ [T/m^{n-2}]	$\int b_n$ [-]
1	-6.9701e$-$04	1.0000e+04
3	-6.1652e$-$06	1.4152e$-$01
5	-1.7529e+01	6.4349e+02
7	-3.3540e+02	1.9710e+01
9	-1.3733e+01	1.2912e$-$01
11	2.0793e+07	-3.1281e+00
13	7.7843e+08	-1.8737e$-$01
15	1.2553e+09	-4.8344e$-$04

Table 20: Allowed integrated multipoles for the vertical orbit corrector, $R_{\text{ref}} = 40$ mm.

n	$\int A_n\, ds$ [T/m^{n-2}]	$\int a_n$ [-]
1	-6.9717e$-$04	1.0000e+04
3	-3.8141e$-$06	8.7533e$-$02
5	1.7514e+01	-6.4312e+02
7	-3.3534e$-$02	1.9702e+01
9	-2.8942e+01	2.7206e$-$01
11	-2.0786e+07	3.1263e+00
13	7.8699e+08	-1.8939e$-$01
15	-1.5958e+09	6.1444e$-$04

It is more practical to assess the overall field quality when all three fields are generated simultaneously by considering the combined currents of the sextupoles and the superimposed corrector fields, as shown in Table 18. The resulting magnetic field components are shown in Figures 108 to 111 in the Appendix. Due to the absence of symmetry in the cross-sectional design, all multipoles are allowed. The normalization is performed with respect to B_3, which represents the primary component of the magnet. From Table 21, it is clear that there is still a large integrated b_5 and a_5 component. However, it is less than the corresponding components of the sextupoles of SESAME [41]. It could be combated by adjusting the shim design, but this has not been investigated further. Although the integrated SNM does not meet the field quality requirements, the integrated RFD satisfies its target, as demonstrated in Figure 85.

Table 21: Allowed integrated multipoles for sextupole, with the combined horizontal and vertical dipole fields, R_{ref} is 40 mm.

n	$\int B_n \, ds \ [\text{T}/\text{m}^{n-2}]$	$\int A_n \, ds \ [\text{T}/\text{m}^{n-2}]$	$\int b_n \ [\text{-}]$	$\int a_n \ [\text{-}]$
1	-7.1012e−04	-7.0121e−04	1.2664e+03	1.2665e+03
2	-1.2107e−06	4.4738e−06	8.7464e−02	-3.2320e−01
3	-3.4605e+00	2.8573e−05	1.0000e+04	-8.2568e−02
4	1.0839e−03	8.5320e−04	-1.2529e−01	-9.8622e−02
5	-1.7576e+01	1.7583e+01	8.1262e+01	-8.1298e+01
6	1.5409e−02	-3.2621e−01	-2.8497e−03	6.0330e−02
7	-3.3501e+02	-3.4138e+02	2.4783e+00	2.5255e+00
8	-1.1114e+01	-7.3530e+01	3.2889e−03	2.1758e−02
9	3.6793e+04	-1.4322e+03	-4.3549e−01	1.6952e−02
10	2.3575e+04	-1.7308e+04	-1.1162e−02	8.1944e−03
11	2.0915e+07	-2.0396e+07	-3.9609e−01	3.8626e−01
12	-2.1546e+06	5.0384e+06	1.6322e−03	-3.8167e−03
13	1.0297e+09	8.1492e+08	-3.1201e−02	-2.4693e−02
14	1.3191e+09	-1.9304e+08	-1.5988e−03	2.3397e−04
15	3.4980e+12	-2.6432e+10	-1.6959e−01	1.2815e−03
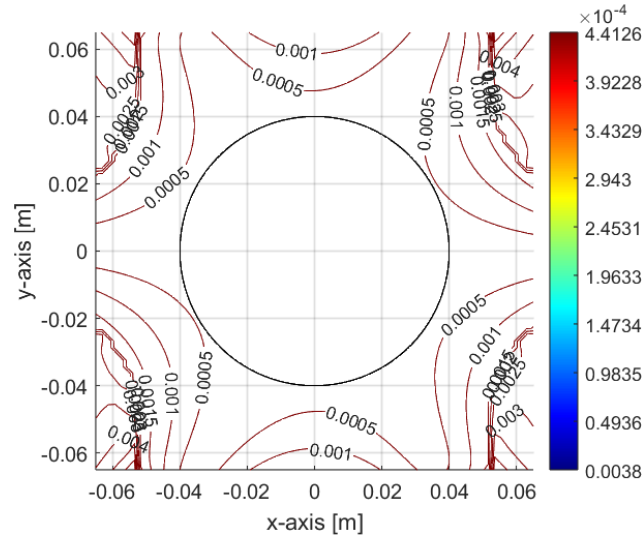
Figure 85: The RFD with respect to the sextupole and corrector fields. The black line denotes the GFR in which the maximum of the RFD is 4.4×10^{-4}.

8   Manufacturing

The yokes for the dipole, quadrupole, and sextupole magnets can be manufactured from solid iron or by stacking laminated sheets. Solid iron yokes involve less tooling than the more complex processes involved in stamping, stacking, and assembling laminated yokes. Despite this, laminated yokes offer several advantages in terms of performance and cost. Laminated yokes allow for the improvement of relative field deviation and magnet reproducibility by sorting or shuffling the laminations based on their magnetic properties. Additionally, the materials used for laminations tend to be more cost-effective [20]. Given that the MB magnet will experience cycling, the use of stacked laminations provides a crucial benefit. Insulating the laminations electrically will help to minimize eddy currents induced by changing magnetic fields, thus enhancing performance. Therefore, the yokes of the different magnets will be constructed from electrically insulated laminations. Insulation can be achieved using either inorganic methods, such as oxidation, phosphating, or Carlite coatings, or organic methods, like epoxy coatings. With epoxy-coated laminations, the sheets are glued into substacks, then assembled and welded together at the outer edges to maintain the integrity of the internal material properties. These exterior welds ensure that the magnetic properties within the magnet remain unaffected.

In the case of the dipoles, due to the horizontal symmetry, a single lamination shape is used corresponding to half of the yoke's total cross-section, as shown in Figure 30. A four-piece design is not possible due to the vertical asymmetry. The two-piece design also allows for the insertion of the coils into the yoke before the top and bottom halves are assembled. Similarly, quadrupole yokes are constructed using either a two-piece or four-piece laminated design. While a two-piece assembly simplifies construction and reduces potential mechanical errors, the four-piece design offers more space for coil and vacuum chamber installation. Therefore, the quadrupoles will utilize a four-piece laminated yoke, with careful attention given to the assembly process and lamination shuffling. Likewise, the sextupoles will be fabricated using a six-piece laminated design.

The magnet coils will be carefully wound according to precise geometric specifications. Bending the concave part of the dipole coil will be challenging; a mandrel will be used to facilitate this.

Once the coils are wound, they undergo a potting process, in which the coils are encapsulated in a resin matrix. This step not only provides mechanical stability but also improves thermal conductivity, which is essential for efficient heat dissipation during magnet operation. The potted coils are then assembled into the yoke structure, ensuring precise alignment and positioning to achieve optimal magnetic performance.

8.1   System Integration

The successful operation of HeLICS depends on precise system integration and alignment in accordance with the lattice design. The system integration team is responsible for managing this complex process. Several challenges were encountered during the integration, including collisions between different components. These issues were resolved by adjusting both the proposed magnet designs and the synchrotron lattice. This required close collaboration between the system integration, beam optics and the magnet design team, ensuring proper alignment and functionality of all components. The magnets' yoke and coil-to-coil lengths, shown in Table 22, were carefully minimized to prevent collisions and optimize performance. Figure 86 provides a schematic overview of the synchrotron, illustrating the arrangement of various components.

8.2   Power Consumption

Figure 87 shows the peak electrical power of the magnets, totalling 890 kW. This value is significant, and comparing it to existing synchrotrons, such as the CNAO facility, offers valuable

Table 22: Dimensions of the different magnets.

	MB	MQB	MQF	MQD	MSX
Yoke width [mm]	1050	759.5	759.5	759.5	512.8
Yoke length [mm]	2737	356.4	356.4	191.4	82.3
Coil-to-coil length [mm]	2925	489.9	489.9	324.9	204.4
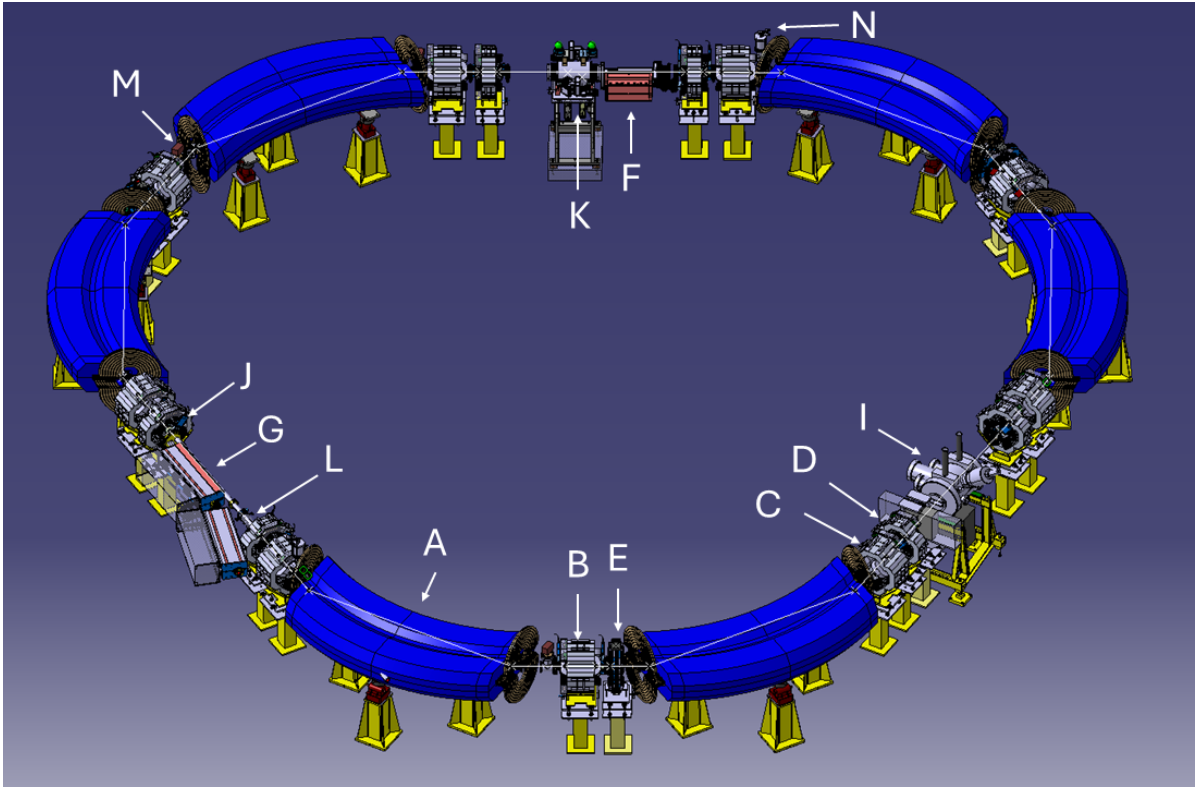
Figure 86: Schematic of the HeLICS Synchrotron showing the placement of various components around the ring. Key components include MB (A), MQB (B), MQF (C), MQD (D), MSX (E), injection septa (F), extraction septa (G), kicker (-), RF-cavity (I), BPM (J), BTV (K), tune pickup (L), vacuum pump (M) and sector valve (N).

insights. The CNAO synchrotron accelerates protons up to 250 MeV/u and carbon ions up to 400 MeV/u, with a magnetic beam rigidity of 6.3 Tm [42]. The total peak electrical power for CNAO's dipole, quadrupole, and sextupole magnets is 795 kW [43].

The largest discrepancy in power consumption arises from the dipole magnets. CNAO utilizes sixteen dipoles, each with a peak power of 39 kW, contributing to a total of 617 kW. In contrast, HeLICS employs six dipoles (2.67 times fewer), each consuming 127 kW (3.3 times more). Various differences in the design of both dipoles will be highlighted to indicate where this discrepancy could come from. Although the CNAO dipoles have a similar aperture height of 72 mm, they operate at a lower peak magnetic field of 1.5 T, which results in fewer ampere-turns [44]. This lower peak magnetic field also reduces magnetic saturation, improving magnetic efficiency. This comes at the expense of a larger bending radius, necessitating more floor space.

Both systems generate the magnetic field with the same number of turns, but CNAO uses a larger conductor cross-section (25x25 $\varnothing$8.0 mm). This requires more coil space, which is easier to accommodate in CNAO's H-shaped design compared to HeLICS' O-shaped design. However, this also results in a larger cross-sectional area of the magnet, 0.66 m^2, compared to 0.46 m^2. The advantage of the larger conductor is reduced electrical resistance for similar currents, leading to lower power consumption in CNAO dipoles compared to those in HeLICS.

Due to the shorter dipoles in CNAO, only two cooling circuits are needed per magnet, compared to four in HeLICS. However, the total number of cooling circuits is 32, 1.5 times more than in HeLICS. With more cooling circuits, each circuit has to dissipate less thermal energy, making cooling less demanding.

The interplay of these factors makes it difficult to isolate a single cause for the difference in power consumption. Every design element impacts the overall efficiency and performance of the magnets. While it is possible to reduce the power consumption of the HeLICS dipoles, achieving this would require either increasing the size of the magnets or expanding the available floor space — both considered undesirable. An alternative solution is the use of superconducting coils. Advances in high-temperature superconductors make this an exciting option. The magnetic field could be increased to 2.42 T, the required peak field for carbon ion extraction at 430 MeV/u. However, this benefit is counteracted by the need to supply energy for cooling the superconducting coils. Careful evaluation of these trade-offs is essential for optimizing both performance and operational practicality.
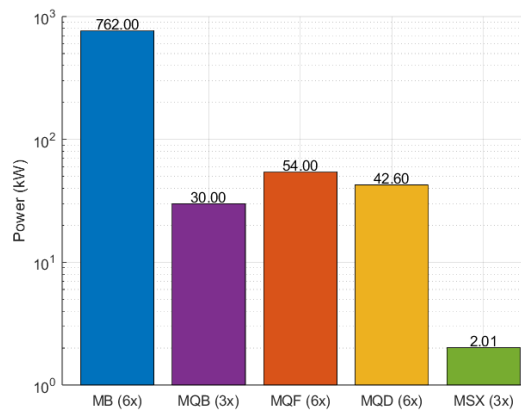
Figure 87: Peak power consumption per magnet type, displayed in logarithmic scale. The number of magnets is indicated in the parentheses. The total power consumption of all magnets is 890 kW.

9   Conclusion

This thesis has explored the design and optimization of the magnet system within the context of HeLICS as part of the NIMMS team at CERN. Helium ion therapy offers a potential alternative to proton and carbon ion therapies. The advantages of helium ions, including a sharper Bragg peak and reduced lateral scattering, make them particularly suited for treating cancers near critical structures. NIMMS seeks to balance cost-efficiency with technical viability, aiming to make advanced cancer treatment more widely accessible through HeLICS.

The design work undertaken in this thesis has focused on the various magnets required for HeLICS, the dipoles, quadrupoles, and sextupoles. Each of these magnets plays a unique role in the synchrotron. The requirements for field quality, mechanical robustness, and manufacturability guided their design. The work minimised relative field deviation and unwanted higher-order multipoles across various operational conditions through detailed iterative simulation processes. Through fine-tuned shimming techniques, the stringent field quality requirements are met to maintain beam stability and precision.

Special attention was given to thermal and electrical stability, ensuring the magnets can operate reliably under the expected loads. The cooling systems were carefully designed to manage the thermal loads, while the electrical configurations were optimized to balance power consumption, magnet size and overall efficiency. This thesis also briefly explored the possibility of future upgrades using (high-temperature) superconducting coils, which could significantly

reduce power consumption and operational costs while allowing for even higher magnetic fields.

Integration of the magnet system into the broader synchrotron design posed additional challenges. Close collaboration with the system integration and beam optics teams helped to resolve these issues, leading to a magnet system that is fully integrated with the rest of the HeLICS framework.

In summary, the magnet system design presented in this thesis represents a vital step toward realizing an efficient, compact helium ion therapy facility. The insights gained throughout this process contribute significantly to the technical advancement of the HeLICS project. Looking ahead, future work will likely focus on utilizing superconducting coils. This could reduce energy demands and allow carbon ion therapy in a much smaller and cheaper synchrotron than existing designs. Continued development of HeLICS and similar systems will help make helium ion therapy a viable, cost-effective treatment for cancer patients, expanding access to advanced ion therapies.

References

[1] Hyuna Sung et al. "Global Cancer Statistics 2020: GLOBOCAN Estimates of Incidence and Mortality Worldwide for 36 Cancers in 185 Countries". In: *CA: A Cancer Journal for Clinicians* 71.3 (May 2021), pp. 209–249. ISSN: 0007-9235. DOI: 10.3322/caac.21660.

[2] Rebecca L. Siegel et al. "Cancer statistics, 2023". In: *CA: A Cancer Journal for Clinicians* 73.1 (Jan. 2023), pp. 17–48. ISSN: 0007-9235. DOI: 10.3322/caac.21763.

[3] NIH. *Radiation Therapy Side Effects.* Jan. 2022. URL: https://www.cancer.gov/about-cancer/treatment/types/radiation-therapy/side-effects.

[4] Cancer Research UK. *Long term side effects of radiotherapy.* Mar. 2024. URL: https://www.cancerresearchuk.org/about-cancer/treatment/radiotherapy/side-effects/long-term-side-effects.

[5] M Vretenar et al. *Conceptual design of a compact synchrotron based facility for cancer therapy and biomedical research with helium and proton beams.* Tech. rep.

[6] *Particle therapy facilities in clinical operation.* June 2024. URL: https://www.ptcog.site/index.php/facilities-in-operation-public.

[7] William Saunders et al. *Helium-Ion Radiation Therapy at the Lawrence Berkeley Laboratory: Recent Results of a Northern Cal-ifornia Oncology Group Clinical Trial.* Tech. rep. 2. 1985.

[8] Andrea Mairani et al. "Roadmap: Helium ion therapy". In: *Physics in Medicine and Biology* 67.15 (Aug. 2022). ISSN: 13616560. DOI: 10.1088/1361-6560/ac65d3.

[9] Line Hoeltgen et al. "Helium Ion Therapy for Advanced Juvenile Nasopharyngeal Angiofibroma". In: *Cancers* 16.11 (May 2024), p. 1993. ISSN: 2072-6694. DOI: 10.3390/cancers16111993. URL: https://www.mdpi.com/2072-6694/16/11/1993.

[10] Santa Gabriella Bonaccorsi et al. "Exploring Helium Ions' Potential for Post-Mastectomy Left-Sided Breast Cancer Radiotherapy". In: *Cancers* 16.2 (Jan. 2024). ISSN: 20726694. DOI: 10.3390/cancers16020410.

[11] Barbara Knäusl et al. "Can particle beam therapy be improved using helium ions? – A planning study focusing on pediatric patients". In: *Acta Oncologica* 55.6 (June 2016), pp. 751–759. ISSN: 1651226X. DOI: 10.3109/0284186X.2015.1125016.

[12] M G Pullia et al. "EXPLORATIVE STUDIES OF AN INNOVATIVE SUPERCON-DUCTING GANTRY". In: *Proceedings of IPAC2022* (2022), pp. 2966–2969. DOI: 10.18429/JACoW-IPAC2022-THPOMS012. URL: https://www.hitriplus.eu/..

[13] J. M. Schippers. "Cyclotrons for particle therapy". In: *CERN Yellow Reports: School Proceedings.* Vol. 1. May. CERN, 2017, pp. 165–175. ISBN: 9789290834557. DOI: 10.23730/CYRSP-2017-001.165.

[14] Alexander Wu Chao and Maury Tigner. *Accelerator Physics.* Tech. rep.

[15] Y Jongen. "Cyclotrons from protons to Carbon for Hadron Therapy". In: 2013.

[16] Ashraf El-Saftawy. "Regulating the performance parameters of accelerated particles". PhD thesis. 2013.

[17] Stephanie Rädel. "On space charge driven microbunching instability in bERLinPro". PhD thesis. Mar. 2017.

[18] Davide Tommasini. *4. FORMULAE - Practical Definitions & Formulae for Normal Conducting Magnets.* Tech. rep. 2011.

[19] Helene Felice et al. *Unit 5 Field harmonics.* Tech. rep. Brunswick: USPAS.

[20] Attilio Milanese. *RT magnet design, fabrication and testing*. Tech. rep. St. Pölten: CAS, Dec. 2023.

[21] P Schnizer, E Fischer, and Germany B Schnizer. "MAGNETIC FIELD DESCRIPTION IN CURVED ACCELERATOR MAGNETS USING LOCAL TOROIDAL MULTIPOLES". In: 2011.

[22] S Maridor and D Perini. *ELENA BEAM AND VACUUM PIPE CLEARANCE ANALY-SIS*. Tech. rep. 2014.

[23] Diogo Miguel Louro Alves, Ricardo Marco Hernandez, and Lars Soby. *The ELENA BPM System. Status and Plans*. Tech. rep. Geneva: CERN, Oct. 2016.

[24] Thomas Zickler. "Basic design and engineering of normal-conducting, iron-dominated electromagnets". In: *Accelerator Physics* (June 2010), pp. 65–102. DOI: 10.48550. URL: https://arxiv.org/abs/1103.1119.

[25] Vinit Kumar and Amalendu Sharma. "Understanding the edge focusing in dipole magnets". In: *Indian Particle Accelerator Conference*. 2018, pp. 776–778. URL: https://www.researchgate.net/publication/321588584.

[26] Masumi Umezawa Futaro Ebina Yusuke Fujii Koji Matsuda Kazuo Hiramoto Kikuo Umegaki and Hiroki Shirato. *Development of Compact Proton Beam Therapy System for Moving Organs*. Tech. rep. 8. 2015. URL: https://api.semanticscholar.org/CorpusID:21954106.

[27] H Huttunen et al. *OPTICS DESIGN OF A COMPACT HELIUM SYNCHROTRON FOR ADVANCED CANCER THERAPY*. Tech. rep.

[28] Lowry Conradie. *Magnet Design - Workshop on Accelerator Technologies, Basic Instruments and Analytical Techniques*. Tech. rep. Trieste: ICTP-IAEA, Oct. 2019.

[29] Xiande Fang, Yu Xu, and Zhanru Zhou. "New correlations of single-phase friction factor for turbulent pipe flow and evaluation of existing single-phase friction factor correlations". In: *Nuclear Engineering and Design*. Vol. 241. 3. Mar. 2011, pp. 897–902. DOI: 10.1016/j.nucengdes.2010.12.019.

[30] *Electrical steels - European product offer by ArcelorMittal*. Tech. rep.

[31] Attilio Milanese. *RT_dipole_solution_script.txt*. Geneva, 2024.

[32] G Petrucci and D Tommasini. *The ELETTRA Storage Ring Magnets*. Tech. rep. 1993.

[33] R P Walker and D Zangrando. *Measurement and Correction of the ELETTRA Storage Ring Dipole Magnets*. Tech. rep. 1993.

[34] L Dallin, T Summers, and D Bodnarchuk. "OPTIMIZING BEAM BRIGHTNESS AT THE CANADIAN LIGHT SOURCE". In: *ParticleAcceleratorConference*. 2007.

[35] D Einfeld et al. *MODELLING OF GRADIENT BENDING MAGNETS FOR THE BEAM DYNAMICS STUDIES AT ALBA*. Tech. rep.

[36] L Dallin et al. *GRADIENT DIPOLE MAGNETS FOR THE CANADIAN LIGHT SOURCE*. Tech. rep. URL: http://www.lightsource.ca/.

[37] Pallippattu Krishnan Vijayan, Arun K. Nayak, and Naveen Kumar. "Governing differential equations for natural circulation systems". In: *Single-Phase, Two-Phase and Supercritical Natural Circulation Systems*. Elsevier, 2019, pp. 69–118. DOI: 10.1016/b978-0-08-102486-7.00003-2.

[38] Jack Tanabe. *Iron Dominated Electromagnets Design, Fabrication, Assembly and Measurements*. Tech. rep. 2005.

[39] Th Zickler. *DESIGN REPORT OF THE QTG QUADRUPOLES FOR THE CERN CNGS LINE*. Tech. rep. Geneva: CERN, Aug. 2000.

[40] K Halbach. "FIRST ORDER PERTURBATION EFFECTS IN IRON-DOMINATED TWO-DIMENSIONAL SYMMETRICAL MULTIPOLES*". In: *Nuclear Instruments and Methods* 74.1 (1969), pp. 147–164. ISSN: 0029-554X.

[41] Attilio Milanese and M. Attal. *DESIGN REPORT OF SEXTUPOLE MAGNETS*. Tech. rep. Geneva: CERN, Mar. 2014. URL: www.cern.ch/CESSAMag.

[42] S. Rossi. "The status of CNAO". In: *European Physical Journal Plus* 126.8 (2011), pp. 1–39. ISSN: 21905444. DOI: 10.1140/epjp/i2011-11078-8.

[43] G Bisoffi et al. "ENERGY COMPARISON OF ROOM TEMPERATURE AND SUPERCONDUCTING SYNCHROTRONS FOR HADRON THERAPY". In: *Proceedings of IPAC2022*. 2022, pp. 3080–3083. ISBN: 9783954502271. DOI: 10.18429/JACoW-IPAC2022-THPOMS049.

[44] G Brianti, M Giesch, and S Rossi. *EUROPEAN ORGANIZATION FOR NUCLEAR RESEARCH DIPOLE OF THE CNAO SYNCHROTRON (Based on the PIMM Study)*. Tech. rep. 1998.

A   Fields Dipole
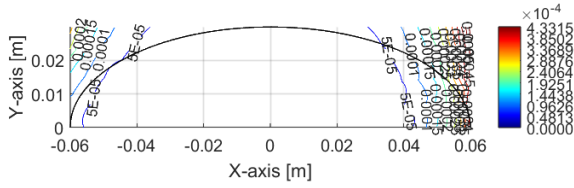
Figure 88: The RFD over the GFR at 0.167 T, the magnetic field strength required to inject protons.
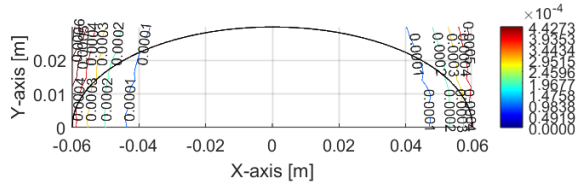
Figure 89: The RFD over the GFR at 1.63 T, the magnetic field strength required to extract protons.
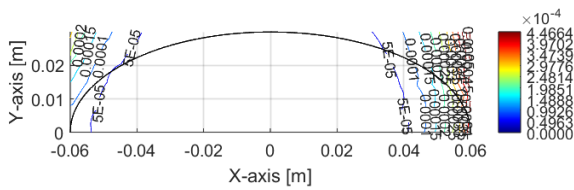
Figure 90: The RFD over the GFR at 0.236 T, the magnetic field strength required to inject helium and carbon ions.
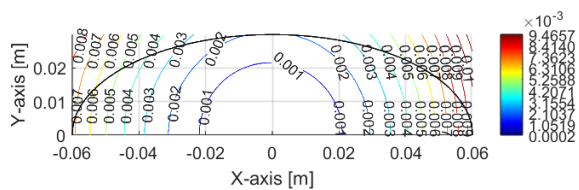
Figure 91: The RFD in the GFR at 2.42 T, the magnetic field strength required to extract carbon ions.

B   Fields Quadrupoles
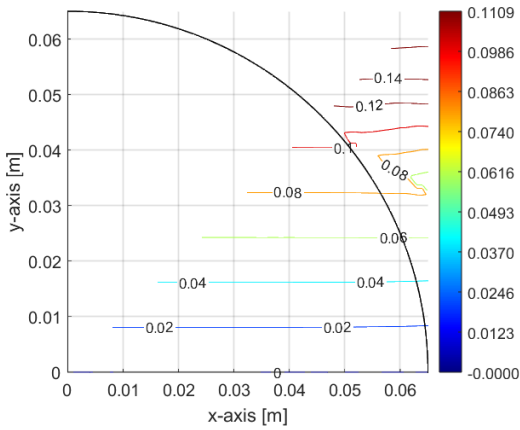
Figure 92: Integrated B_x for the MQB.
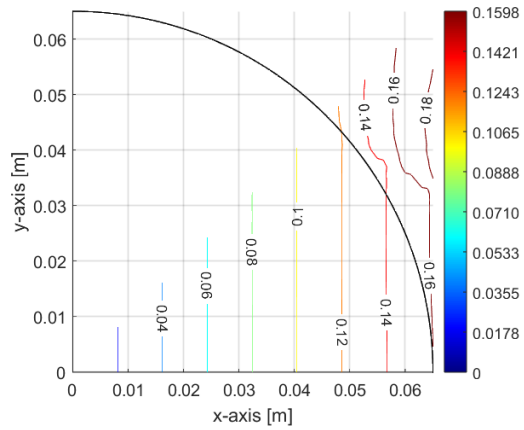
Figure 93: Integrated B_y for the MQB.
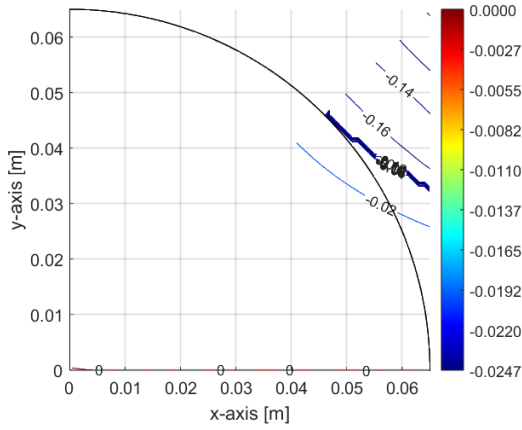
Figure 94: Integrated B_z for the MQB.
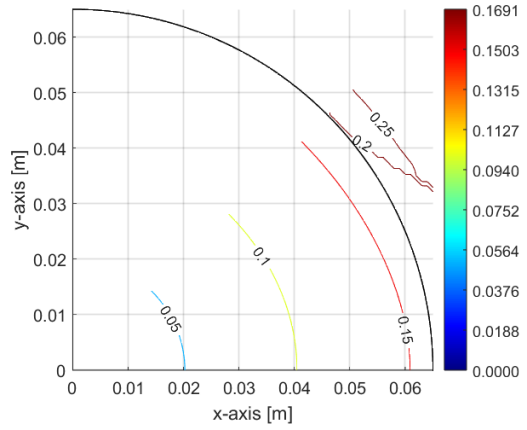
Figure 95: Integrated $|B|$ for the MQB.
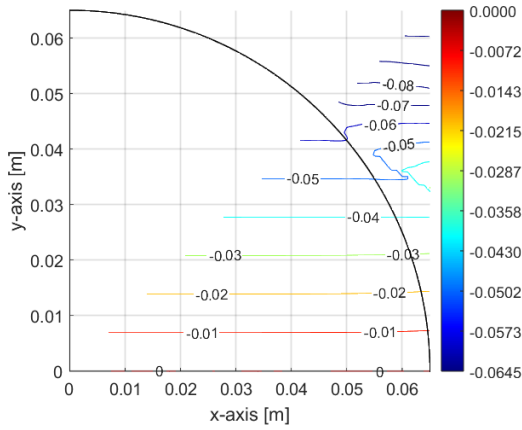
Figure 96: Integrated B_x for the MQD.
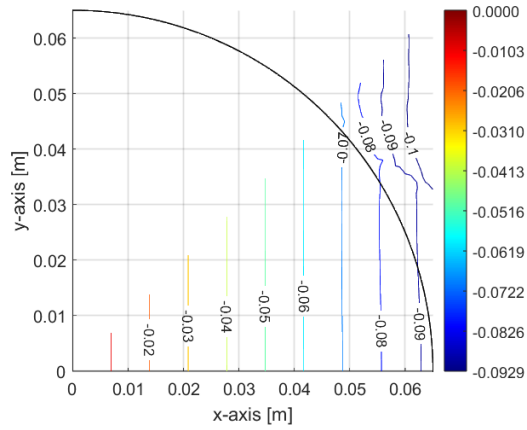
Figure 97: Integrated B_y for the MQD.
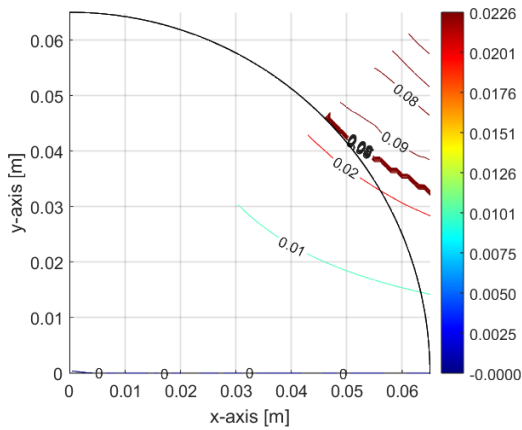
Figure 98: Integrated B_z for the MQD.
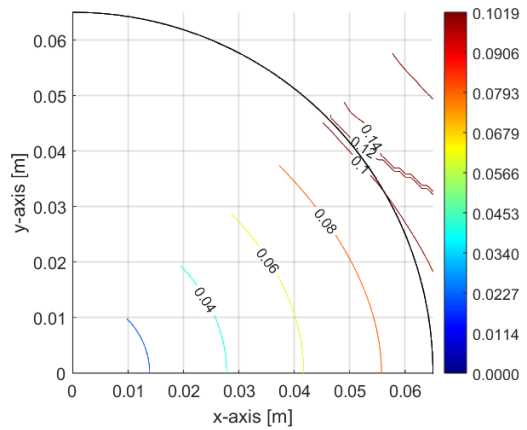
Figure 99: Integrated $|B|$ for the MQD.

C   Fields Sextupoles
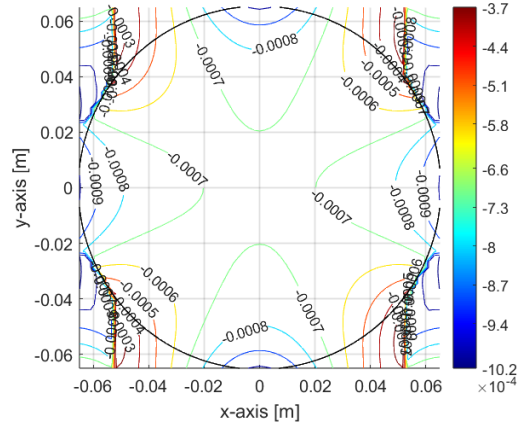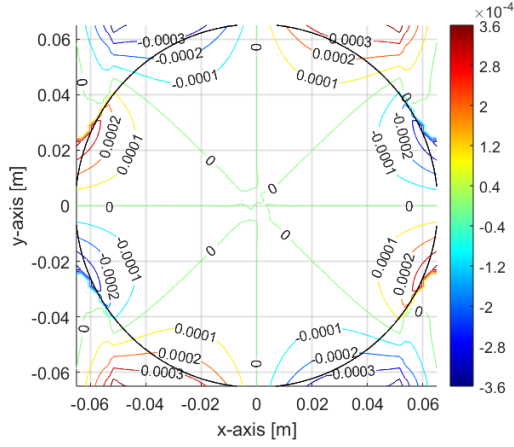
Figure 100: Integrated B_x for the horizontal trim.

Figure 101: Integrated B_y for the horizontal trim.
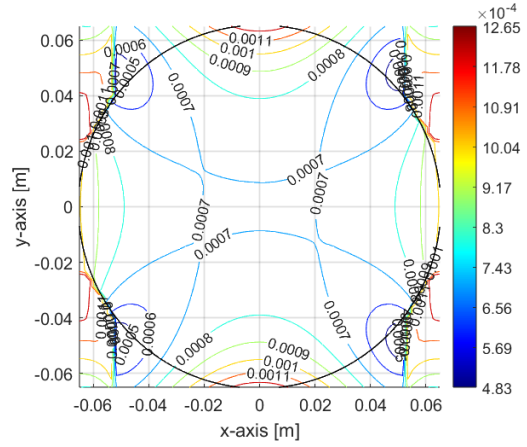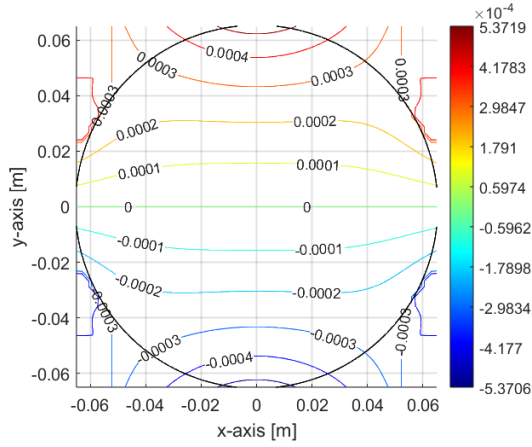
Figure 102: Integrated B_z for the horizontal trim.

Figure 103: Integrated $|B|$ for the horizontal trim.
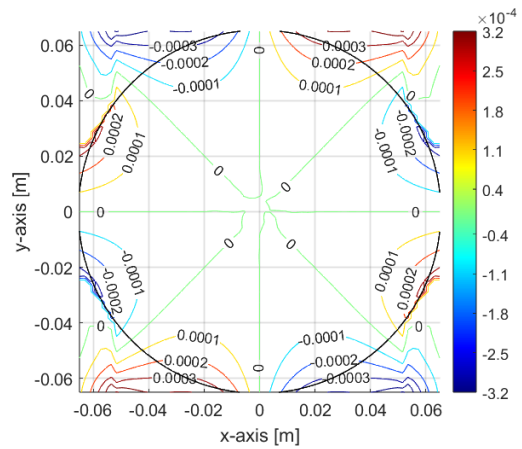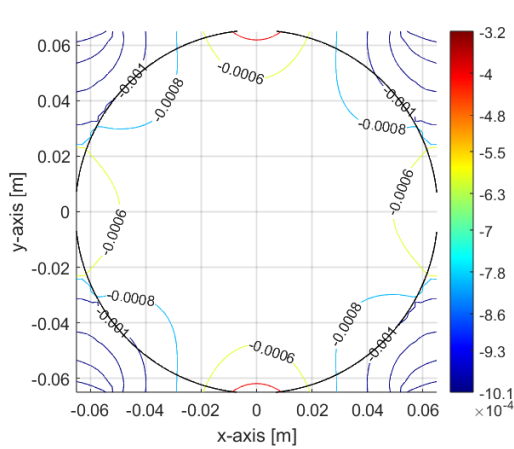
Figure 104: Integrated B_x for the vertical trim.

Figure 105: Integrated B_y for the vertical trim.

61
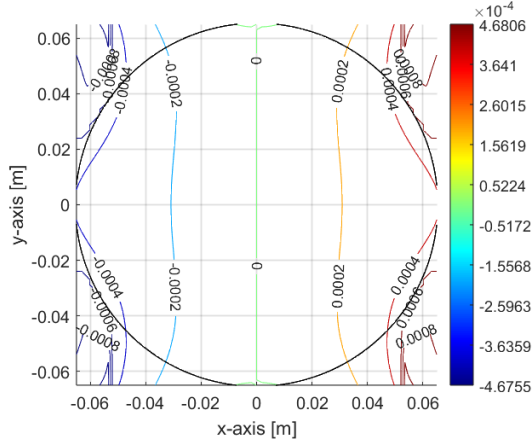
Figure 106: Integrated B_z for the vertical trim.
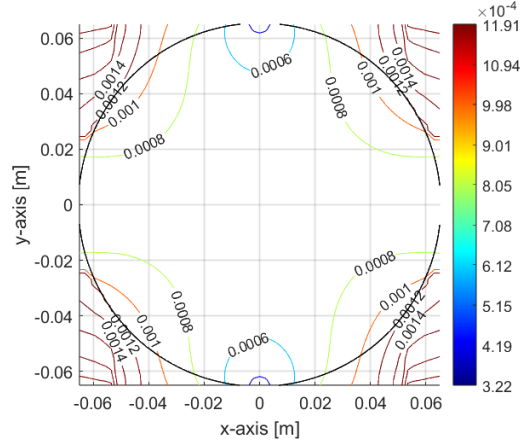
Figure 107: Integrated $|B|$ for the vertical trim.
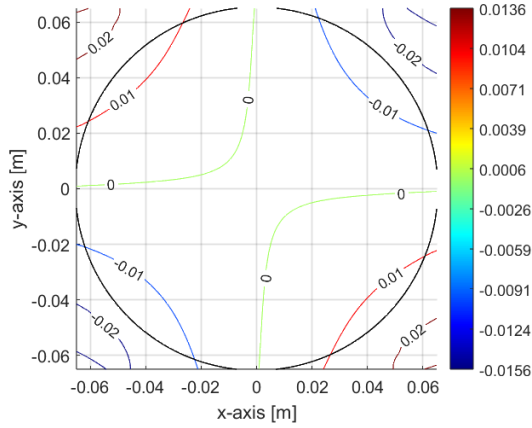
Figure 108: Integrated B_x for the horizontal trim, vertical trim and sextupole field combined.
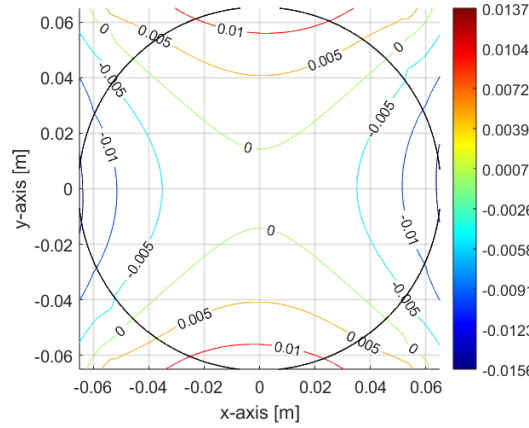
Figure 109: Integrated B_y for the horizontal trim, vertical trim and sextupole field combined.
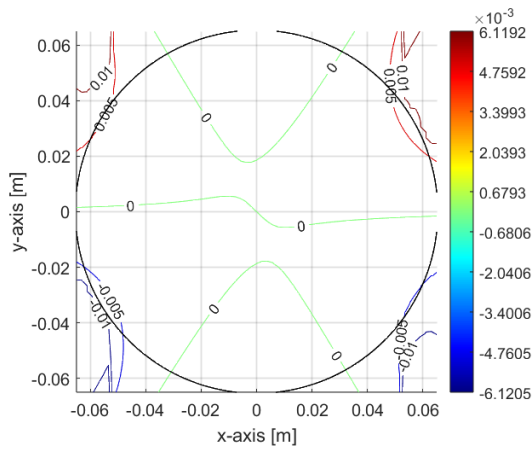
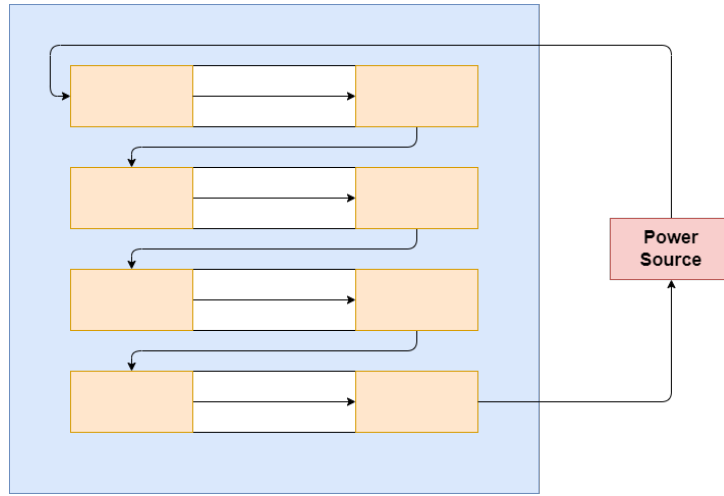Figure 110: Integrated B_z for the horizontal trim, vertical trim and sextupole field combined.
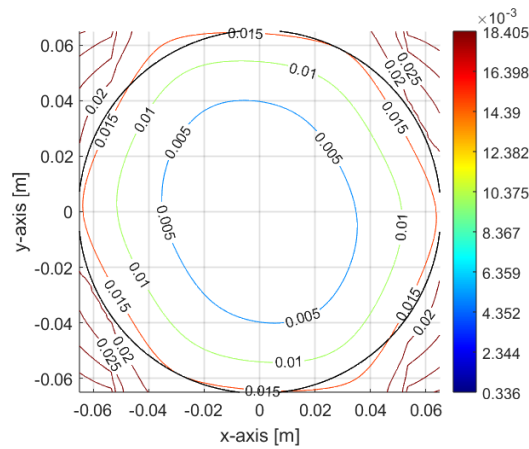
Figure 111: Integrated $|B|$ for the horizontal trim, vertical trim and sextupole field combined.

62

D Electrical and cooling circuits

Figure 112: Electrical circuit for the MB, the four layers are powered in series.
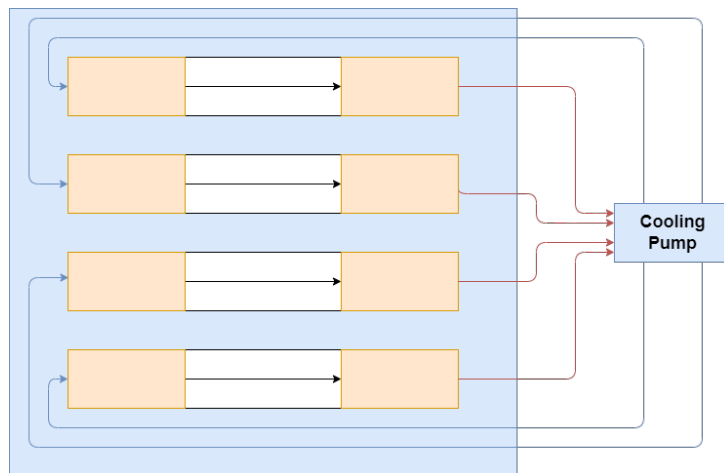
Figure 113: Cooling circuit for the MB, the four layers are cooled in parallel.
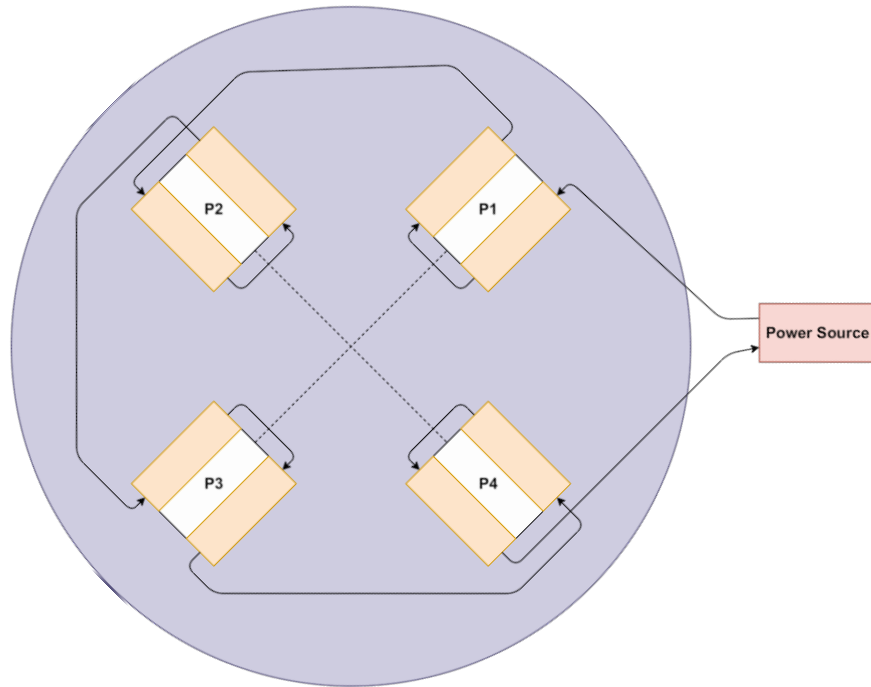
Figure 114: Electrical circuit for the quadrupole magnets, the four poles are powered in series, with alternating polarity.
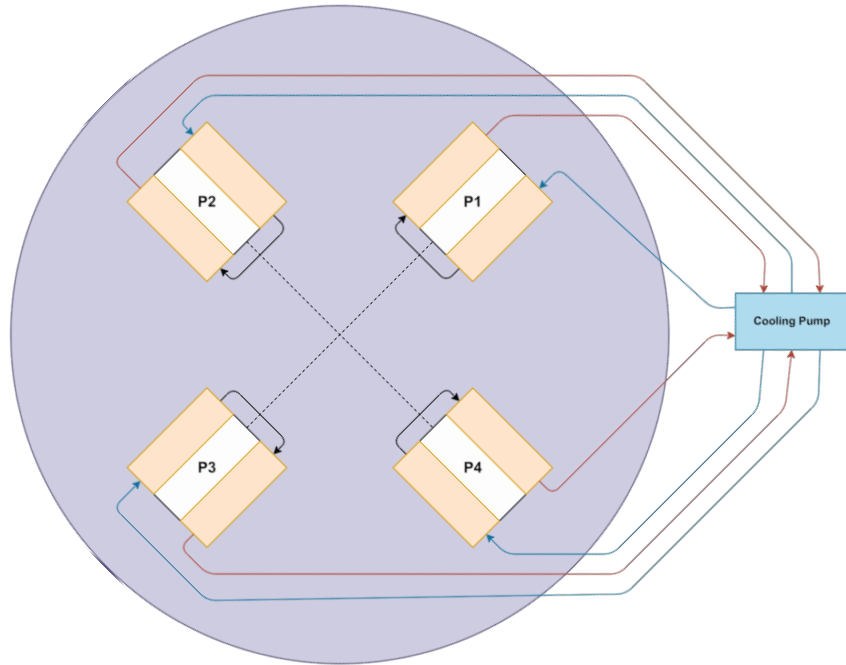
Figure 115: Cooling circuit for the quadrupole magnets, the four poles are cooled in parallel.
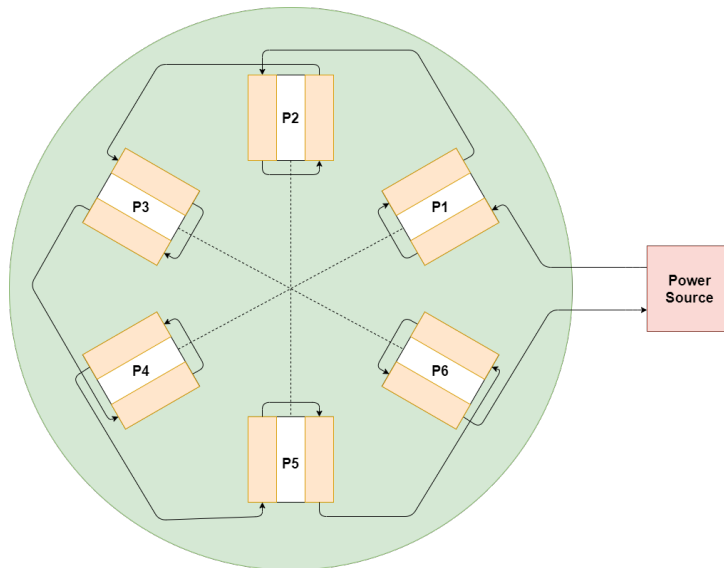

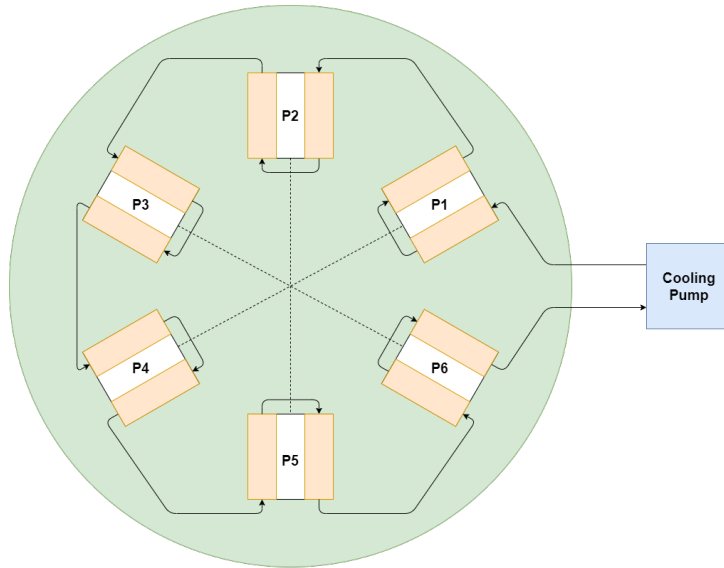Figure 116: Cooling circuit for the MSX, the six poles are powered in series, with alternating polarity.

Figure 117: Cooling circuit for the MSX, the six poles are cooled in series.